12-2012

Structure and Dynamics of High Temperature Superconductors

Jennifer Lynn Niedziela
jniedzie@utk.edu

To the Graduate Council:

I am submitting herewith a dissertation written by Jennifer Lynn Niedziela entitled "Structure and Dynamics of High Temperature Superconductors." I have examined the final electronic copy of this dissertation for form and content and recommend that it be accepted in partial fulfillment of the requirements for the degree of Doctor of Philosophy, with a major in Physics.

Takeshi Egami, Major Professor

We have read this dissertation and recommend its acceptance:

Elbio Dagotto, Jaime Fernandez-Baca, Norman Mannella

Accepted for the Council:
Carolyn R. Hodges

Vice Provost and Dean of the Graduate School

(Original signatures are on file with official student records.)

12-2012

Structure and Dynamics of High Temperature Superconductors

Jennifer Lynn Niedziela
jniedzie@utk.edu

To the Graduate Council:

I am submitting herewith a dissertation written by Jennifer Lynn Niedziela entitled "Structure and Dynamics of High Temperature Superconductors." I have examined the final electronic copy of this dissertation for form and content and recommend that it be accepted in partial fulfillment of the requirements for the degree of Doctor of Philosophy, with a major in Physics.

Takeshi Egami, Major Professor

We have read this dissertation and recommend its acceptance:

Elbio Dagotto, Jaime Fernandez-Baca, Norman Mannella

Accepted for the Council:
Carolyn R. Hodges

Vice Provost and Dean of the Graduate School

(Original signatures are on file with official student records.)

Structure and Dynamics of High Temperature Superconductors

A Dissertation

Presented for the

Doctor of Philosophy

Degree

The University of Tennessee, Knoxville

Jennifer Lynn Niedziela

December 2012

Dedication

To my grandparents, who have all inspired me in their own unique ways.

Acknowledgements

I have been exceptionally fortunate in my nascent career, and this is due directly to the people I have had the privilege to know. I would like to express my gratitude for a few people in particular.

First and foremost, I wish to express my thanks to my thesis supervisor Takeshi Egami, who's inspirational words and novel approaches to complex problems prove remarkably motivational time and again. I also thank the members of my doctoral committee, Elbio Dagotto, Jaime Fernandez-Baca, and Norman Mannella for their time, patience, guidance, and instruction.

I would like to recognize the contributions of Dan Parshall and Konstantin Lokshin to the work presented here. In addition to invaluable experimental contributions, Dan and Kostia have frequently provided important insight and context to our findings, as well as needed challenges, and friendship. In particular, I would like to recognize the extensive effort Dan has put into phonon visualization that has been invaluable to this work, helping me to draw physical insight into the complex entanglement of the phonons in the present study.

A neutron scatterer is nowhere without sample growers, so I would like to expressly thank Athena Safa-Sefat, Michael A. McGuire, and Chenglin Zheng for sample growth and characterization. Further, the I am deeply grateful to the instrument staff and scientific computing groups that have supported this work at Oak Ridge National

Laboratory, Argonne National Laboratory, Los Alamos National Laboratory, the SPring-8 Synchrotron, the Institut Laue Langevin, and the CEA-Saclay. Thanks also go to the hardworking administrative staff at the University of Tennessee Physics Department, who have been a tremendous help on the bureaucratic end of getting this work done.

To all of my friends and family, I thank you for giving me the chance to take on this task, even though it takes me away from all of you. Last, and most of all, I wish to thank my partner in life Nicholas Luciano. I feel so lucky to have found a partner that can provide countless hours of love, support, encouragement, and conversation and who can give me the occasional lecture on neutronics when I need it. I look forward to our new adventures as we start the next part of our lives.

“History of science and technology has consistently taught us that scientific advances in basic understanding have sooner or later led to technical and industrial applications that have revolutionized our way of life.”

-Enrico Fermi

Abstract

High temperature superconductivity in iron based compounds has presented a series of complex problems to condensed matter physics since being discovered in 2008. The stalwart basis of condensed matter physics is the “strength in numbers" aspect of crystalline periodicity. Perfect crystalline periodicity has made possible the reduction of the questions of structural and electronic properties to single dimensions, increasing the tractability of these problems. Nevertheless, modern complex materials stretch these assumptions to their limits, and it is at this point where our work starts. Using neutron and x-ray scattering, we have conducted a series of studies on the structural disorder of iron based superconductors and found it to be ubiquitous. Further, we have investigated the lattice dynamics of the iron-based superconducting systems, and found anomalous phonon behavior, with coupling between the spin and lattice degrees of freedom. These findings together raise questions on the role of structural disorder in complex materials, high temperature superconductivity specifically.

Contents

List of Tables

List of Figures

List of Acronyms

AF anti-ferromagnetic

APS Advanced Photon Source

ARCS Wide Angular Range Chopper Spectrometer

ARPES Angle Resolved Photo Emission Spectroscopy

BCS Bardeen, Cooper, and Schrieffer

BFA $BaFe_2As_2$

CCR closed-cycle refrigerator

CNCS Cold Neutron Chopper Spectrometer

cT collapsed tetragonal

DAC diamond-anvil cell

DAS data acquisition system

DFT density functional theory

DMFT dynamical mean-field theory

DOS density of states

GL Ginzburg-Landau theory

FeSC iron-based superconductors

FM ferromagnetic

HFIR High Flux Isotope Reactor

HIPD High Intensity Powder Diffractometer

HTSC high temperature superconductivity

ILL Institut Laue-Langevin

INS inelastic neutron scattering

IXS inelastic x-ray scattering

LDA Local Density Approximation

LLB Laboratoire Léon Brillouin

MV magneto-vibrational

NIST NIST Center for Neutron Research

NOMAD Nanoscale Ordered Materials Diffractometer

NPDF Neutron Powder Diffractometer

NTE negative thermal expansion

NSF non-spin-flip

NRIXS Nuclear Resonant Inelastic X-ray Scattering

ORNL Oak Ridge National Laboratory

pDOS phonon density of states

PDF pair distribution function

PG pyrolitic graphite

POWGEN Powder Diffractometer Next Generation

QMC Quantum Monte Carlo

RF radio frequency

RUS Resonant Ultrasound Spectroscopy

SDW spin-density wave

SF spin-flip

SNS Spallation Neutron Source

TA transverse acoustic

TAS triple-axis spectromter

TDS thermal diffuse scattering

TOF time-of-flight

WLS wavelength-shifting

YBCO $YBa_2Cu_3O_7$

Symbols

Symbol	Description
β	$1/k_BT$
b	Neutron scattering length
γ	relativistic gamma, E_{tot}/E_{rest}
E_F	Fermi energy
E_f	final energy
E_i	incident energy
E_r	resonance energy
$g(\mathbf{r})$	pair distribution function
$G(\mathbf{r})$	reduced pair distribution function
$\hbar$	reduced Planck's constant
$\hbar\omega$	energy (meV unless otherwise noted)
k_B	Boltzmann's constant
$\mathbf{k_F}$	Fermi wavevector
$\mathbf{k_f}$	final wavevector
$\mathbf{k_i}$	incident wavevector
$\mathbf{Q}$	momentum transfer ($Å^{-1}$ unless otherwise noted)
$\mathbf{q}$	inelastic momentum transfer
$\mathbf{Q} \perp \mathbf{P}$	momentum transfer perpendicular to neutron polarization
$\mathbf{Q} \parallel \mathbf{P}$	momentum transfer parallel to neutron polarization
$\mathbf{P}$	neutron polarization
r_0	classical electron radius
$S(\mathbf{Q}, \omega)$	dynamic structure factor

Symbol	Description
T_c	critical transition temperature
T_N	magnetic ordering temperature (Néel Temperature)
χ"$(\mathbf{Q}, \omega)$	dynamic susceptibility
μ_B	Bohr magneton
$\mu_\mathbf{N}$	Nuclear magneton
Z	electron number

1 Introduction

It is not exaggeration to say the world would be changed profoundly by room temperature superconductivity, the transmission of electrical current without resistive losses. Superconductivity is not only interesting in its application, but also in its physics. A collective quantum phenomenon, superconductivity requires adjustment to a central tenet of physics that like charges should always repel. The history of superconductivity has forced physicists to reconcile long standing theories with surprising experimental results.

Although the field of superconductivity research has been active for a century[1], basic questions remain, including: “Is there a comprehensive theory capable of describing all superconducting properties?"; “Is room temperature superconductivity possible?"; “Can we develop materials with high critical fields and currents for industrial application?"; and “Can we predict superconductivity from first principles?" Addressing these questions requires a considerable amount of theoretical and experimental work, synthesis of results, and creative thinking.

Consensus on superconductivity remains elusive. Many issues remain contentious, but a few notions are relatively settled: 1) electron-phonon coupling is responsible for some versions of superconductivity, and in these cases the pairing is isotropic and s-wave, 2) the pairing symmetry in copper-oxide high temperature superconductors is d-wave. The superconducting mechanism in high temperature superconductors, the

[1] Probably. Kamerlingh Onnes kept a poorly dated lab notebook.(20).

role of magnetic excitations, the importance of structural excitations, and even the homogeneity of the structures are all topics of debate. Further, some new discoveries are groundbreaking enough to completely shift the paradigm of understanding; the most recent of these is the 2008 discovery of high temperature superconductivity in FeSC.

The work presented herein explored several avenues directly related to the structural effects in high temperature superconductivity (HTSC). A historical background and review of recent work in superconductivity is given in chapter 2, along with a review of recent developments in experiment and theory. The physical properties of the studied compounds are presented in Section 2.5. Chapter 3 will review essential physics for context of the results. Dynamic lattice effects are central to the work presented herein, lattice effects are presented separately in Section 3.2, with mechanisms of spin-phonon coupling in Section 3.5, with particular emphasis on the Invar effect and mechanism of magneto-elastic coupling. Magnetism, specifically distinctions between static order and itinerant states, will be addressed in section 3.4. Chapter 3.6 presents structural heterogeneity, and its application in HTSC. A growing amount of evidence questions the fundamental assumption of perfect periodicity in crystalline systems, and FeSC are a platform to explore deviations from periodicity and the impact on electronic effects. Neutron and x-ray scattering were used for this work, and both techniques are described in Chapter 4, with sufficient detail to convey the experimental results.

Chapter 5 describes neutron and x-ray powder diffraction experiments to analyze the local and average structure as a function of chemical substitution and temperature. In the first set of studies on compounds derived from $BaFe_2As_2$, the fundamental result is the observation of a small but finite set of distortions in the FePn_4 tetrahedra, and the breakdown of local symmetry assignment for $BaFe_2As_2$. Further, superconducting compounds are found to exhibit negative thermal expansion in the superconducting state. Studies performed on $FeTe_{1-x}Se_x$ systems highlight the substantial impact of local disorder on the superconducting properties, with different treatments producing superconductivity unexpectedly.

The second component of this work focused on using neutron and x-ray scattering to study lattice mechanisms, specifically spin-phonon coupling in FeSC. In an inelastic x-ray experiment, a softening was observed of the transverse acoustic phonon at the magneto structural transition temperature in $BaFe_2As_2$, which is due to an increase in the electron-phonon coupling brought on by enhanced intraband Fermi-surface nesting(21), and the direct coupling of the spin and lattice systems. Inelastic neutron and x-ray scattering measurements also provide evidence exists of anomalous phonon behavior across the spectrum of studied materials, including atypical thermal behavior, phonon lifetime changes, temperature-dependent intensities, and direct magnetic coupling to the phonon spectra. These results are presented in Chapter 6.

The goals of this work were to study the static and dynamic lattice behaviors, and connect these lattice properties to the superconducting or magnetic behaviors in the system of FeSC. All of the work conducted feeds to this central question: "What is the role of the lattice in high temperature superconductors?" In the course of this work a larger question emerges: "What is the role of heterogeneity in HTSC?" and, perhaps a more profound question is "What is the level of electronic stability of the HTSC against lattice distortion?" These questions and future work are addressed in the final chapter.

2 Superconductivity

Superconductors are a class of compounds that exhibit zero resistance to electrical current flow below a finite temperature. Superconductivity was discovered by Kamerlingh Onnes in 1911 when Onnes observed the electrical resistance of mercury dropped abruptly below 4.2 K to what for all measurable purposes was zero(22; 23). The last century has seen the discovery of superconductivity in a large number of material classes, remaining absent in materials exhibiting electronic stability[1], or strong magnetic states[2](see Fig. 2.1)(5).

Forty years after Onnes' discovery, Bardeen, Cooper, and Schrieffer were able to finalize a theoretical framework of the microscopic theory of superconductivity in their nobel-prizewinning work on the eponymous Bardeen, Cooper, and Schrieffer Theory (BCS)(24). The key insights to the BCS mechanism are that the long-range (effective) interactions between electrons are attractive, resulting in an instability in the Fermi surface against a pairing interaction forming the *Cooper pairs*(25), and the condensation of these pairs opens a gap in the energy spectrum near the Fermi surface of the order 3.5 $k_B T_c$(24). More fundamentally, the formation of the pair state is indistinguishable from the condensation because electrons that aren't paired are able to break the paired state(26). The BCS framework successfully describes a number of key behaviors of the superconducting state. Later formulations of this theory provided a full picture from the

[1] e.g., the Nobel Gases and "precious metals" do not superconduct at any known pressure or temperature
[2] e.g., superconductivity is only seen in a few transition metals or rare earth elements

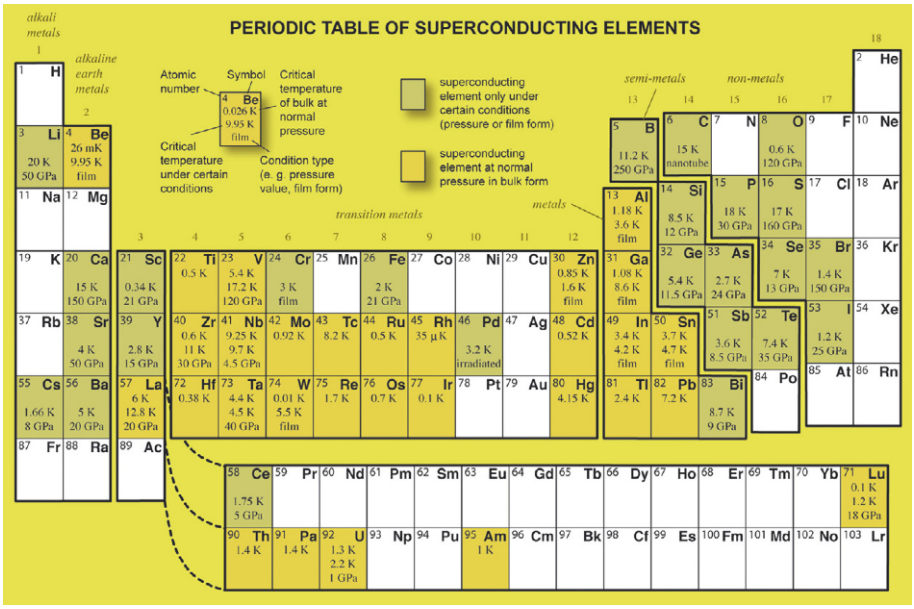

Figure 2.1: Superconducting conditions of pure elements. Figure from (5).

weak to strong coupling regime(27; 28; 29), and a predicted limitation on the value of T_c attainable(30). After these developments, work progressed for another 40 years an industrial development of superconductors with waning effort applied to searching for higher T_c materials.

Nevertheless, in 1986, 2001, and 2008, the theoretical maximum temperature was bested by the discovery of cuprates(31; 32; 33), magnesium diboride(34), and FeSC(35; 7). In addition to pure elements, cuprates, and iron based superconductors, superconductivity is observed in systems of heavy fermions(36), organic conductors(37), fullerenes(38), and ruthenates(39). All of these systems pose challenges to the BCS formulation, and demand new explanations. To date, there is no universally accepted theory of high temperature superconductivity.

The next few sections will deal more deeply with the different superconducting classes, the history of the development of BCS theory, cuprate HTSC, and FeSC. We begin with a more in depth review of the experimental and theoretical facets of different types of superconductors.

2.1 Superconducting basics

In addition to having zero electrical resistance, superconductors are perfect diamagnets. The perfect diamagnetism of the superconducting state makes possible the complete expulsion of magnetic fields in a bulk superconducting state (the Meissner effect), and a limited distance of magnetic field penetration (the London penetration depth). These properties are the hallmarks of a superconducting material, and distinguish superconductors from other types of conductors.

The field of superconductivity research has a rich history of phenomenology, where material properties and experimental observations played a large role in the development of the history that persists to the current day. One of these phenomenological mainstays is the classification of superconductors as “Type I" , “Type II", “conventional”, or “unconventional”. The distinction between the different types of superconductors is done on the basis of the behavior of the Meissner effect and adherence with BCS:

- A **Type I** superconductor does not support a magnetic field of any strength, expelling completely any applied field up to a critical temperature or critical field.
- A **Type II** superconductor has two (up to three) distinct regions of support for magnetic field penetration.
- A **conventional** superconductor can be described by BCS.
- An **unconventional** superconductor cannot be described by BCS.

Type I superconductors are typically simple metals or alloys, and the T_c for the onset of superconductivity for type I superconductors is below 10 K. The maximum magnetic field the superconductor can be exposed to is of the order of a few hundred gauss, above this field and temperature, the superconducting behaviors are quenched. The magnetic field on the surface is confined to the London penetration depth:

$$B(x) = B_0 \exp\left(-\frac{x}{\lambda_L}\right)$$

which is analogous to "skin depth" penetration of an AC field into a conductor, and gives a distance λ_L, the distance into the superconductor where the magnetic field has become a factor of e weaker(40). These penetrations are roughly 50-500 nm, and are highly sample dependent.

Superconductivity is considered to be a collective, cooperative quantum phenomena involving the ordering of the electronic state. This effect is most directly seen in what is known as the superconducting gap[3]: the range of energies where there are no electronic excitations in the superconductor. The gap size is of the order of a few meV, and is directly related to the value of the T_c via the relationship: $E_g \approx 3.5 k_B T_c$ for BCS superconductors. Measurement of the superconducting gap is accessible through a number of experimental techniques. Due to the ordered electronic configuration, superconductors have lower entropy compared to a regular conductor, and consequently lower free energy, making the superconducting gap size directly proportional to a jump in specific heat at T_c. The gap is temperature dependent in the BCS theory, which reflects the collective nature of the effect. The gap structure is isotropic in conventional superconductors, but may have nodes in an unconventional material. The gap can be measured through specific heat measurements; scanning tunneling spectroscopy, where it appears as a valley in the tunneling spectra; or absorption experiments. The symmetry of the superconducting gap is related to the crystal structure, and can be detected with Angle Resolved Photo Emission Spectroscopy (ARPES).

Type II superconductors can sustain distinct levels of magnetic field, and typically have a higher transition temperature and critical field than their type I counterparts. The magnetic field descriptions are commonly denoted H_{Cn}, where $n = 1, 2, 3$ (Fig. 2.2). When $n = 1$, applied magnetic fields are completely expelled from the bulk in the same manner as a type I. When $n = 2$, the magnetic flux inside of the superconductor is maintained, but only in quantized units of flux, known as fluxons. When $n = 3$ the magnetic field is confined to the surface, and the magnetic field in the bulk is absent.

[3]The superconducting gap is a common, but not universal feature in superconductors, and there is evidence for gapless superconductivity in materials doped with magnetic impurities, and theoretical basis for this from a moderate modification of the Abriskov-Gorkov result(41).

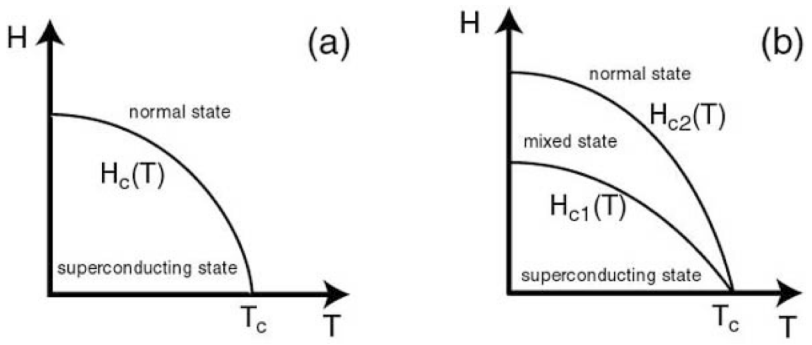

Figure 2.2: Distinction between Type-I (a) and Type-II (b) superconductors. The Type-I superconductor expels all magnetic fields below a critical field, above which it becomes a normal conductor. The Type-II superconductor supports three distinct states of field before the magnetic field collapses the superconductivity.

The coherence length, interpreted as the spatial extent of the Cooper pairs, is given in terms of the Fermi velocity and the superconducting energy gap:

$$\xi_0 = \frac{2\hbar v_F}{\pi E_g} \tag{2.1}$$

With a few exceptions, type II superconductors are typically compound materials. Some type II superconductors are described by the BCS theory, while other type II superconductors are lacking a complete theory. The distinction between type I and type II superconductors can be traced to the ratio of the coherence length ξ_0, (Eq. 2.1) to the penetration depth λ_L. If the ratio $\lambda_L/\xi_0 > 1$, the material will be a type II superconductor (and a type I superconductor for the case $\lambda_L/\xi_0 < 1$). For the type II superconductors, the critical field for $n = 1$ can be approximated by $(\xi/\lambda)H_C$, while for $n = 2$, $(\lambda/\xi)H_C$.

The coherence length and description of the penetration depth are successes of the work of Ginzburg and Landau who formulated a theory for superconductivity. In the Ginzburg-Landau theory (GL), the system is described as having a macroscopic “order parameter", and this order parameter is treated in a mean field study. This formulation was able to describe the superconducting system and the phase transition, but was not microscopic in detail. The order parameter that was defined is now recognized to

be the macroscopic wave function of the superconducting state, with its modulus the superconducting pair density(42).

2.2 BCS Theory

In 1950 Fröhlich published a theory on the superconducting ground state driven by electron lattice coupling(43; 44). This work was confirmed by the demonstration of the isotope effect which was published a few months prior to Fröhlich's theory (45; 46)[4]

When Cooper began work on the problem, he considered an approach where one allows an arbitrarily small attractive interaction between electrons. In a "normal" metal that can be described as a Fermi liquid, a continuous spectrum of quasiparticles with energies E_k occupies the available states of the system up to the Fermi energy (E_F), with the restriction on state occupancy guaranteed by the Pauli principle. Using the background of the filled Fermi sea, Cooper created a model where two additional electrons were placed into the system, with a low-energy, zero total momentum state. Writing the two electron orbital wave function as:

$$\psi_0(\mathbf{r}_1, \mathbf{r}_2) = \sum_{\mathbf{k}} g_{\mathbf{k}} e^{i\mathbf{k}\cdot\mathbf{r}_1 - i\mathbf{k}\cdot\mathbf{r}_2} \tag{2.2}$$

And then writing this in reduced, symmetrized form:

$$\psi_0(\mathbf{r}_1 - \mathbf{r}_2) = \left[\sum_{\mathbf{k}} g_{\mathbf{k}} \cos i\mathbf{k}\cdot(\mathbf{r}_1 - \mathbf{r}_2)\right](\sigma_{1\uparrow}\sigma_{2\downarrow} - \sigma_{2\uparrow}\sigma_{1\downarrow}) \tag{2.3}$$

one uses the Schrödinger equation with Hamiltonian to obtain energy eigenvalues:

$$(E - 2E_{\mathbf{k}})g_{\mathbf{k}} = \sum_{k'>k_F} V_{\mathbf{k}\mathbf{k}'} g_{\mathbf{k}'} \tag{2.4}$$

[4]The canonical story of superconductivity is typically told that Fröhlich had no knowledge of the experiments on the isotope effect, arriving at his theory in isolation from this set of discoveries. The idea of this "happy coincidence" has recently been called into question. There are allegations that a) Fröhlich knew about the isotope effect experiments, and that b) this had a profound effect on the development of the theory of superconductivity. You can read the sordid accusations for yourself in reference (47; 48).

Where the $V_{\mathbf{kk'}}$ describe the particulars of the interaction potential. If one considers the interaction to be a constant, then one may re-write the eigenvalues as $\frac{1}{V} = \sum_{k>k_F} \frac{1}{(2E_k - E)}$, and then writing the sum as an integral and including the electronic density of states at the Fermi level:

$$\frac{1}{V} = N(0) \int_{E_F}^{E_F + \hbar\omega_c} \frac{dE_k}{(2E_k - E)} = \frac{1}{2} N(0) \ln \frac{2\mathrm{E_F} - \mathrm{E} + 2\hbar\omega_\mathrm{c}}{2\mathrm{E_F} - \mathrm{E}} \tag{2.5}$$

In this formulation, there is always at least one bound state, and that the bound state is present no matter how small the interaction potential V may be. It is important to note that due to the non-analytic behavior of the energy eigenvalues, a solution is not possible from more standard perturbation theory approaches(49; 40).

The key realization to BCS is that there is a phonon mediated net attraction between electrons near the Fermi surface of the material that causes the formation of boson-like "Cooper" pairs in a net zero angular momentum state(25), which then condense to form the macroscopic superconducting state. In the paired, condensed state, the electrons are able to flow like a superfluid like state through the conducting material. More fundamentally, the formation of the pair state is indistinguishable from the condensation because electrons that aren't paired are able to break the paired state(26).The mean distance between electrons in type I superconductors is of the order or 1000 Å, resulting in regions of many thousands of overlapping pairs.

BCS theory is particularly successful, describing several key behaviors of superconductors. Among these are that the energy gap for individual particle-like excitations is described; and the isotope effect is explained, accounting for the shift of T_c with ionic mass. BCS introduced several simplifications. The first of these is that the attraction between electrons is constant for electrons within some energy epsilon and zero otherwise, and the second is that Coulombic interaction between electrons may be neglected. While these two assumptions work well to describe the weakly coupled superconducting state, the generalization prompted by the works of Migdal(27),

Eliashberg(28), and Scalapino(29) provide the full picture of BCS superconductivity which works from a weak to a strong coupling regime.

McMillian combined these tenets into an equation that accurately predicted the superconducting transition temperature materials (30). The equation:

$$k_B T_C = \frac{\hbar\omega}{1.2} exp\left(-\frac{1.04(1+\lambda)}{\lambda - \mu^*(1+0.62\lambda)}\right) \tag{2.6}$$

accounts for the electron-phonon interaction (discussed in Chap. 3.) λ, and μ^* is a phenomenological parameter obtained from fitting. The McMillian upper limit is about 23 K, worked well to describe Nb and was widely interpreted as putting a cap on the value of T_c. Neverthless, Allen and Dynes found that in principle there was no upper limit to T_c in the regime of very strong coupling between electrons and phonons, finding that the value of $T_c \backsim \lambda^{1/2}$(50). Indeed MgB_2, with a T_c of 40 K has very strong electron phonon coupling in a few phonon branches resulting in the description of MgB_2 as an Eliashberg superconductor(51).

Cuprates, iron based superconductors, and heavy fermion compounds fall into the class considered "unconventional superconductors," in that the superconductivity in these compounds cannot be described by the BCS as currently formulated. Understanding the superconducting mechanism in unconventional materials is a problem at the forefront of condensed matter physics.

There are important similarities observed between different families of unconventional superconductors. First, the cuprate(52; 53), heavy fermion, and iron pnictide(54; 55) families all exhibit a magnetic resonance at the antiferromagnetic ordering vector, the energy of which scales with the superconducting critical temperature. Further, there is a universal connection between the energy of the spin resonance and the superconducting energy gap, with a linear relationship of $E_r/2\Delta = 0.64(4)$, where E_r is the energy of the resonance, and Δ is the size of the superconducting energy gap in meV(56).

Theories of HTSC are as varied as the compounds themselves. While elemental superconductors are well-described by the BCS theory of superconductivity(24) with

modifications from Eliashberg (28), a mechanism describing all families of superconductivity remains unknown, though not for lack of effort on the part of experimental and theoretical physicists from myriad specialties. A leading theoretical basis[5] to describe the electron pairing mechanism in unconventional HTSC is the exchange of magnetic spin fluctuations. This theory has its roots in the idea of a repulsive electron-electron interaction mediated by spin fluctuations, which itself has a theoretical basis in Kohn-Luttinger theory that Cooper pairing of fermions is possible due to many-body effects resulting in attractive pairing forces for pairs with large orbital angular momenta(58). This "spin fluctuation" mechanism has been applied to both cuprates and FeSC. Nevertheless, complex materials are well known to exhibit behaviors arising from multiple degrees of freedom available to the system, implicating lattice and orbital effects along with spin. Research presented here will focus primarily on the subject of the most recently discovered general class of iron-based superconductors (FeSC), and the interactions between the spin and lattice systems.

2.3 Cuprates

In 1986, Bednorz and Müller revealed that they had been successful in creating a new class of superconductors(31). This new class of materials was based on a layered perovskite structure with layers of copper oxide bounding the perovskite. Breaking six of the six phenomenologically derived "Matthias rules"[6] for superconductivity(8), superconductivity in cuprates came as quite a surprise. Further, at 35 K, T_c was more than the highest previously observed and in apparent violation of the BCS framework.

The cuprate family of superconductors result from charge or hole doping into a layered perovskite structure with a number of CuO_2 planes. The doping into the charge reservoir serves to induce (remove) carriers from the system, which results in

[5]Repulsive electronic exchange is a robust idea, but it is worth noting that recent theoretical constraints have been put forward which indicate that repulsive electron pairing does not work at any screening length or temperature(57).

[6]Matthias Rules: 1. High symmetry is good, cubic is best. 2. Look for materials with high density of states. 3. No oxygen. 4. No magnetism. 5. No insulators.(59) and 6. No theorists. (8)

a suppression of the anti-ferromagnetic (AF) ordering, while doping into the CuO_2 layers directly is not well tolerated(60). The cuprate families are a class of material known as Mott insulators in the normal state, where a material is an insulator due to strong on-site Coulombic repulsion serving to isolate the electrons, which undergo a metal-insulator transition(61) before entering the superconducting phase. To date, the cuprates as a class hold the highest T_c, with the highest critical temperature belonging to $HgBa_2Ca_2Cu_3O_x$ with a T_c of 135K(62), reaching as high as 150K under pressure(63).

Despite decades of research, the completion of a theory of superconductivity in cuprates remains elusive. A number of cuprate properties are well established, including that the superconductivity is due to Cooper pairing, superconductivity occurs in the CuO_2 planes, the pairs are spin singlets, the order parameter symmetry of the single layer tetragonal compounds is $d_{x^2-y^2}$, the coherence length, strongly anisotropic, is of the order of 10 Å, and only 3 Å out of plane.(64; 26). Many cuprate compounds show the existence of a “pseudo gap" region with low electronic DOS, which has been interpreted as being analogous to the superconducting gap, and therefore "proof" of the purely electronic pairing mechanism. Nevertheless, pseudogaps are present in non-superconducting materials like magnetoresistive manganites(65), and nickelates(66), which cast doubt on the direct connection between superconductivity and the pseudogap. Another common feature to cuprate superconductors is the presence of a spin-resonance detected by neutron scattering, interpreted as a signature of the Cooper pair formation in the superconducting state, the energy of the resonance scaling with T_c. The resonance is observed in most, but not all, unconventional superconductors, so while it is important to the superconducting state, the precise nature is still unknown.

A substantive problem in development of the theory is sociological, in that the extensive literature makes consensus difficult(67). When this fact is coupled with issues of sample quality diversity resulting in favoritism of certain types of samples for certain techniques, the result is a difficultly that prevents a unified experimental description of properties for a given technique.

The structural morphology of cuprate superconductors has a common element of layers of CuO_2 planes stacked between layers of rare earth oxide. The CuO_2 planes are composed of square blocks of order 4 Å on a side. The parent compounds are insulating ceramics that exhibit long range antiferromagnetic order. With electron doping or hole doping, this antiferromagnetic state is quickly suppressed, giving rise to a superconducting state which then transitions to a fermi liquid compound. Examples of cuprate structures are shown in Fig. 2.3, and a model phase diagram is shown in Fig. 2.4.

The essential structural frameworks of the cuprate HTSC are well established - the systems are perovskite structures, existing in tetragonal or orthorhombic symmetry, with the square checkerboard layers of CuO_2 omnipresent. The CuO_2 planes are composed of O^{2-} and Cu^{2+} ions. Many systems undergo some manner of structural phase transition.(68) A number of features complicate the structural analysis, including small lattice distortions present in the long-range structure, the questionable stoichiometry of the oxygen, cross substitution, orthorhombic twinning, and other defect/disorder issues present in any crystalline system.(68) The onset temperature of superconductivity of cuprates is correlated with the complexity of the structure, and the number of CuO_2 planes, with the presence of material defects that complicate the structural analysis having a non-trivial impact on the superconducting properties of the samples.(68)

From a structural perspective, the biggest predictor of a high critical temperature for a cuprate is a large number of CuO_2 planes[7], with the supporting layers serving merely as charge reservoirs. This structural feature lead an active area of research in search for a pairing mechanism that focuses on a tunneling or coupling of the Cooper pairs through these planes.(70)

While relatively few reports directly correlate local structural changes with T_c, in $Tl_2Ba_2CaCu_2O_8$ temperature dependent changes in the short-range correlation of the Cu-O bonds are observed, with maximal deviation from expectation at T_c.(71). Refinement of structural models against the PDF data show that there is a high degree of correlation

[7]With reports of T_c near room temperature for a compound with 8 CuO_2 layers.(69)

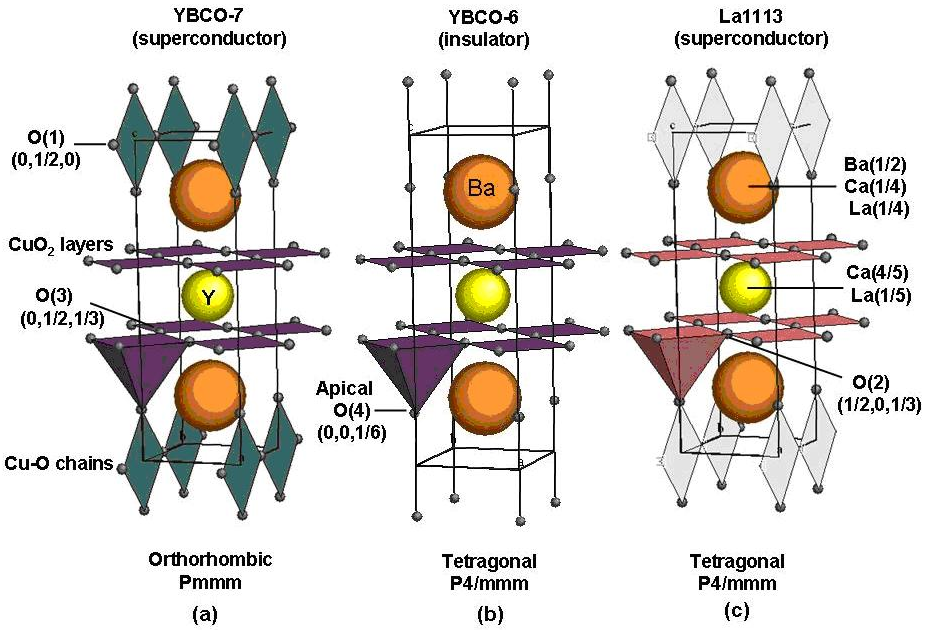

Figure 2.3: Example stoichiometries of cuprate compounds.

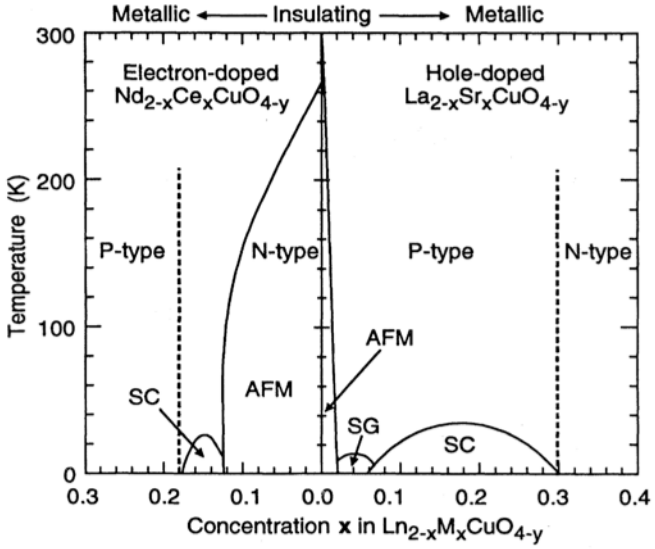

Figure 2.4: Example phase diagram for model cuprate system $Ln_{2-x}M_x\mathrm{CuO}_{4-y}$. Figure from (6)

between the Tl and O atoms in an environment of disordered Cu-O bonds, reflecting a substantial degree of buckling in the Cu-O planes.

Small displacements of oxygen atoms are found in cuprate materials(72). In $YB_2Cu_4O_8$ [8] a deviation from Rietveld structural models is seen around 4 Å (73; 74) suggesting that these displacements are due to the formation of stripes, or other electronic anomaly.(74) Several cuprate compounds exhibit this behavior, and it appears to be a general feature, reflecting distinct Cu environments at T_c.(72)

Planar deviations are also seen in cuprate structures. In $CaSrCuO_2$, the oxygen atoms are displaced parallel to the c-axis, which is not reflected in the average crystal structure(75). This results in a buckling of the CuO_2planes, with a spatial inhomogeneity to the buckling giving rise to the presence of locally ordered atomic displacements which are intrinsic to the structure (75). In $YBa_2Cu_3O_7$ (YBCO), a split in the Cu planar site is seen, supporting the existence of charge inhomogeneities.(76) These changes are not seen in non-superconducting compounds, thus suggesting a connection with superconductivity (77),

In the Tl compounds, the short range (less than 5 Å) structure is found to be substantially different for super and non-superconducting samples, while the long range structure was in good agreement, suggesting that the degree of disorder in the non-superconducting sample was crucial to the destruction of the supercondcutivity.(78) Below T_c, distinct regions of order are seen, while above the spin-gap temperature the domains disappear, findings that are attributed to the formation of charge localizations through some dynamic effect.(73)

2.4 Iron-based Superconductors

Because of the sharp suppression of superconductivity by magnetic pair breaking in metals doped with magnetic impurities, it was thought that magnetic elements doped in superconducting materials would be anathema to the superconducting state.

[8] $YB_2Cu_4O_8$ is used due to its stoichiometric superconductivity and relatively free impurity state.

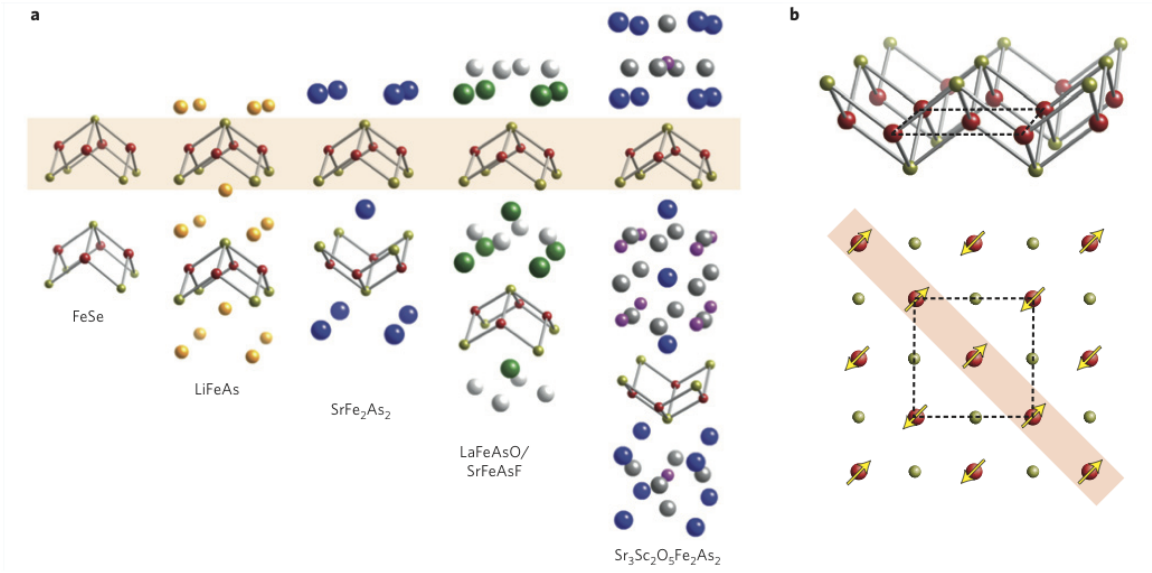

Figure 2.5: Structures of common forms of FeSC. The highlighted stripe emphasizes the presence of the iron layer common to all compounds, and the direction of iron ordering in the magnetic state. Figure from (7).

None of the common magnetic transition metal elements exhibit superconductivity at ambient pressure (Fig. 2.1), and 100 ppm of iron can destroy superconductivity in molybdenum(79). Nevertheless, superconductivity has been reported in a huge number of compounds containing a square planar iron layer, and in some cases even co-existing with the superconducting state.

The first class of FeSC, iron pnictides, were first discovered to be superconducting in 2006, when layered LaOFeP exhibited a T_c of 5 K when fluorine was substituted onto the oxygen site(80). This paper noted the main difference in compositional morphology between the cuprates and the pnictides - that the CuO_2 planes in cuprates have a 2-D planar structure, while the FePn_4 layers have a tetrahedral structure, meaning that the electrons occupy different orbital configurations ($3d_{x^2-y^2}$ for cuprates, $3d_{xz}$, $3d_{yz}$, or $3d_{xy}$ for pnictides). Other reports showed similar behavior in layered chalcogenides (81). Two years later, the Hosono group announced the development of superconductivity with at T_c of 26 K in LaFeAsO with fluorine substitution on the oxygen site(35). To date, the highest transition temperature recorded in an FeSC compound is 55 K(82).

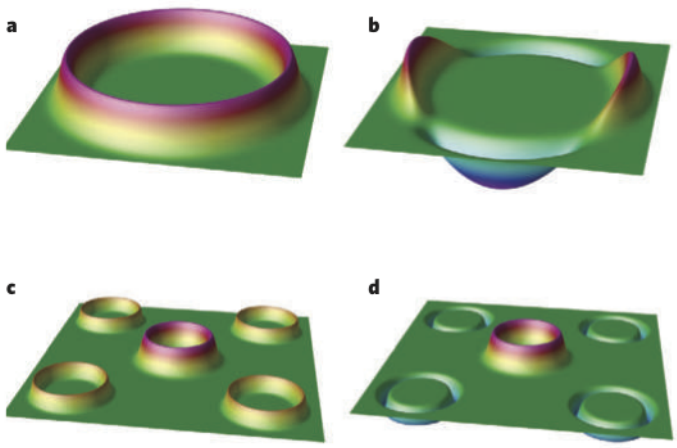

Figure 2.6: Superconducting order parameters for different superconducting classes. **a** s-wave superconductivity for conventional BCS superconductors, **b** d-wave superconductivity as found in cuprates, **c** extended s-wave of MgB_2, and **d** $s_{\pm}$ proposed order parameter for iron superconductors. Figure from (8)

Several categories of superconducting structures have been identified, and are nominally differentiated by the base morphology (Fig. 2.5). The most commonly represented in the literature are REFePnO$_{1-y}$ ("1111") where RE is a rare earth compound; AFe$_2Pn_2$ ("122") where AE is an alkaline earth metal; and the FeTe$_{1-x}$Se$_x$family (also known as the "11"). There are several other groups including the "111" family AFePn, where A is an alkali metal (T_c 25 K), and the AEScFePnO family(83) which has a T_c of 37.5 K in the compound of Sr_2VO_3FeAs, which approaches 45 K with doping on the AE site, though in some doping cases not reaching fully zero resistivity until 7 K(83).

In addition to having the iron layer in common, the iron-based superconductors all exhibit superconductivity in proximity to AF order(84; 3). Most of the compounds are room temperature tetragonal paramagnets[9], which become AF at low temperatures. The AF transition is suppressed with hole(86; 87; 88), electron(89; 90), pressure(91), or isoelectronic substitution(92; 93), eventually giving way to superconductivity.

When FeSC were first discovered, it was hoped that the FeSC would provide insight about the behavior of superconducting cuprates, and link a common origin of HTSC.

[9]Though some recently discovered systems are room temperature AF systems that become superconducting in the presence of large magnetic moments(85)

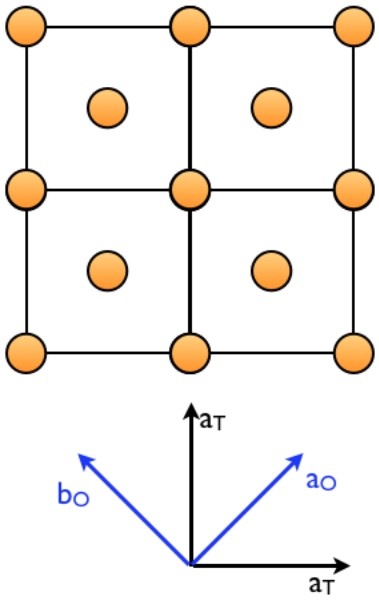

Figure 2.7: Orientation of the a and b axis for a 1111 or 122 FeSC. In the tetragonal phase, $a = b$, so a_T is used to describe the structure. The orthorhombic lattice is rotated 45^o in the $x - y$ plane.

There were immediate similarities apparent between the two classes of compounds. Both have antiferromagnetic ground states, with doping serving to suppress the long range order; both spin fluctuations, and an energy resonance which scales linearly with the superconducting temperature(56). Both cuprates and pnictides have common structural elements where superconductivity occurs - iron planar layers in FeSC and CuO_2 planes in cuprates. It is believed that the superconductivity is confined to these planar structural elements, with the purpose of the interstitial layers to provide carriers or increase Coulomb repulsion.

Nevertheless, there are a few key differences. First, the normal state electronic properties are distinct: cuprates are ceramic Mott-Hubbard insulators, and FeSC have a metallic character[10]. Second, compared to cuprates, FeSC tolerate doping to a greater extent, while the case is opposite in the cuprates where disorder can disrupt

[10] Additionally, it is interesting to note that the FeSC fail to meet the Anderson maxims that HTSC must have a parent compound in a Mott insulator and that the effective spin be $\frac{1}{2}$(67)

the superconductivity due to impurity fluctuations causing the destruction of Cooper pairs(60). Third, the presence of static magnetism and superconductivity support both static magnetism and superconductivity in the underdoped regime(14; 94; 95; 92) in FeSC is unique. As is clear from the phase diagrams of Fig. 2.4 and 2.11, the AF state has no overlap with the superconducting state in the cuprate systems, while there are regions of definite overlap and evidence of coexistence in FeSC. Fourth, the phase diagram of the FeSC is balanced between chemical substitutions, broad ranges of the phase diagram where superconductivity is induced through hole or electron substitution, while for the cuprates, hole and electron substitution produce markedly different phase diagrams. In cuprates, hole doping is more successful in inducing superconductivity, while hole doping in the Fe layer of FeSC does not yield superconductivity. Finally, hole doping in FeSC with the use of Cr suppresses the structural transition in FeSC, but superconductivity is not seen at any doping level. showing that the suppression of the structural transition is not sufficient to induce superconductivity(96).

In addition to the distinct orbital configuration, another difference is the symmetry of the superconducting state. The superconductivity in cuprates has been unambiguously determined to be d-wave(97; 98), which is robust against doping(99), while in FeSC the picture is less clear, although consensus is building around a description of the state as $s\pm$(100)[11]. These are only a few of the new issues raised as a result of comparing cuprates and FeSC.

There are a few key similarities across the iron based superconducting families. First, the parent systems undergo a structural and magnetic transition to a long range antiferromagnetic state with cooling(84; 3), though the precise nature of the structural transition and magnetic order are contested. The lattice distortion from tetragonal to orthorhombic symmetry is required for antiferromagnetic ordering, but whether the lattice distortion allows the AF ordering to take hold, or whether the lattice distortion is a consequence of AF ordering is subject to debate.

[11]Though this too is controversial(101)

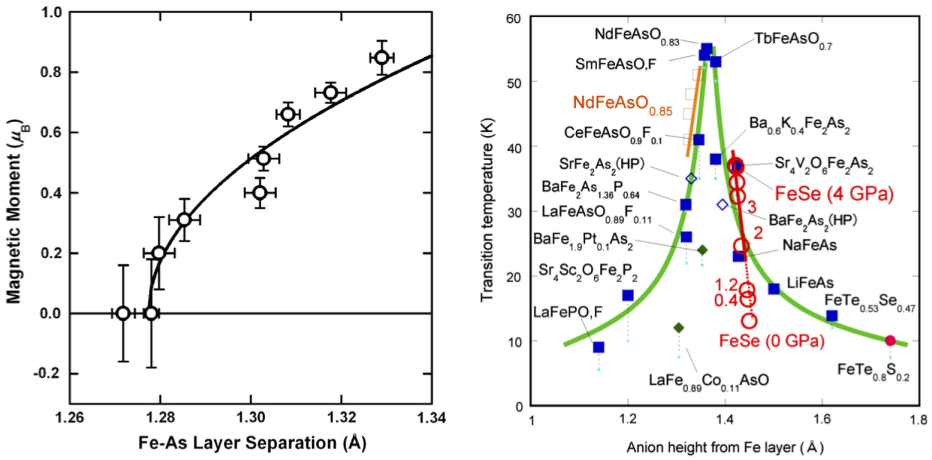

Figure 2.8: Demonstration of the dependence of the magnetic moment (figure from (9), data from (10)) and superconducting transition temperature on the iron-pnictogen distance (figure from (11)).

Second, there is a strong dependence of T_c on the size and "perfection" of the FePn_4 tetrahedra(102; 11) (Fig. 2.8), which can be compared with the phenomenological fact that more CuO_2 planes implies a higher T_c in the cuprates. While this is a potential pathological pitfall, it does highlight the importance of the local environment to the superconducting state.

Another similarity between these families of superconductors is that the strength of the electron-phonon coupling is thought to be not strong enough to account for the high superconducting transition temperature(103; 104), although the value of the coupling increases when magnetism is taken into account, where it is shown that there is a renormalization of phonon modes that involve $Fe - As$ vibrations when magnetism is taken into account, but also find that there is an increased coupling to phonons around the 20 meV mark. (105). The largest effects of magnetism on phonons are in modes involving motion of the Fe-As ions, showing a softening of the 25 meV branch down to 20 meV for the As-Raman mode in $BaFe_2As_2$(106; 105). Further, extreme sensitivity to the size and direction of the magnetic moment in calculations shows that the iron in-plane mode hardens along the AF direction, while the As modes soften. The density functional theory (DFT) calculations of traditional electron phonon coupling also fail to describe

the superconducting properties of cuprates in the case of the cuprates(107; 108; 109). In $A\mathrm{Fe}_2Pn_2$ compounds, the largest effects of magnetism on phonons are in modes involving motion of the Fe-As ions, showing a softening of the 25 meV branch down to 20 meV for the As-Raman mode in $\mathrm{BaFe}_2\mathrm{As}_2$(106; 105). Further, extreme sensitivity to the size and direction of the magnetic moment in calculations shows that the iron in-plane mode hardens along the AF direction, while the As modes soften. (110; 111; 106). Further, the Fermi energy is only 20-40 meV above the bottom of the electron band(112; 113), an energy scale within reach of conventional lattice vibrations.

Due to the omnipresence of the iron layer and empirical structural details clearly showing its import, a substantial body of work focuses on the magnetic interactions in the system resulting from the iron structure. In order to bring calculations in line with experiments, either the structure or magnetic moment would require relaxation, and the values were strongly interdependent with small changes in atomic positions bringing about large changes in the magnetic moment(114). Early theoretical results developed a picture where the magnetic ordering state was realized when the system reached an ideal electronic nesting condition, and that destruction of this nesting condition was requisite for superconductivity(115). Evidence for dynamic local polarization was demonstrated for $\mathrm{CeFeAsO}_{1-x}\mathrm{F}_x$, indicating strong magnetic fluctuations and itinerant iron character(116). Further, it is demonstrated that the impact of chemical substitution is less critical to impact the number of charge carriers, but more to suppress the magnetic state(117). This point is reinforced by studies showing that the impact of pressure is equivalent to that of chemical substition(118). However, the nesting picture is counter-indicated by the details of the magnetic moment and superconducting transition on the lattice shown in Fig. 2.8, which indicate that the structural tuning of the Fe-As layer pushes the system closer or further from the Stoner criterion, strongly impacting the electronic properties.

Early studies of the electronic structure show that the specifics are highly sensitive to the height of the pnictogen atom above the iron plane(115), leading to as much as a 4% discrepancy between experiment and theory. The details of the Fermi surface are similar

across the FeSC family, with electron pockets at the zone corners, and hole pockets at the zone center, with the electronic density of states at the Fermi level only weakly dependent on doping(115; 7), which is supported by experimental observations(119). As the system is electron doped, the effect of doping is to raise the Fermi level so that the hole pocket disappears(120; 121). The electronic band structure is relatively well established, and experimentally confirmed to be dominated at the Fermi level by contributions from the Fe d electron orbitals which are degenerate in the paramagnetic state(122; 123). The nominal iron valence is estimated at Fe^{2+}, which corresponds to a high-spin, high volume iron state.

Early theoretical work shows that the magneto-structural transition in the oxyarsenide LaFeAsO(84) is the manifestation of relieved magnetic frustrations as the AF ordering results in different occupancy for the d_{xz}, d_{yz} orbitals which breaks the tetragonal symmetry(124). Another explanation for the coupling of the transitional behaviors is that of ferro-orbital ordering. A minimal approach applying the Hartree-Fock approximation to a two orbital model shows that AF ordering arises as a consequence of ferro-orbital ordering, which then results in a lattice distortion(125). Three and five orbital models suggest that orbital degrees of freedom are strongly coupled to magnetic ordering, with d_{xz} and d_{yz} susceptible to orbital ordering, but the orbital magnetization much greater for the d_{yz} orbital, resulting in a reduction of the orbital hybridization between the d_{xz} and d_{yz} orbitals(123). The optimal superconducting pnictide compounds display no long range magnetic ordering, yet the Local Density Approximation (LDA) calculations predict a spin polarized ground state, and core-level spectroscopy photoemission studies sensitive to time scales of 10^{-15} s indicates dynamic spin polarization(116).

While the structural distortion in the pnictides is small, the magnetic exchange anisotropy is very large when the exchange constants are calculated from an anisotropic Heisenberg model calculation (Fig. 2.9), yielding SJ_{1a}=59$\pm$2, SJ_{1b}=-9.2$\pm$1.2, SJ_2=13.6$\pm$1.0 meV, with very small interlayer magnetic coupling (SJ_{1c}=1.8$\pm$0.3 meV)(12)

The iron pnictides are very close to the Stoner QCP, meaning that even the smallest of lattice strains can have large effects. The in plane iron phonon mode is relevant to

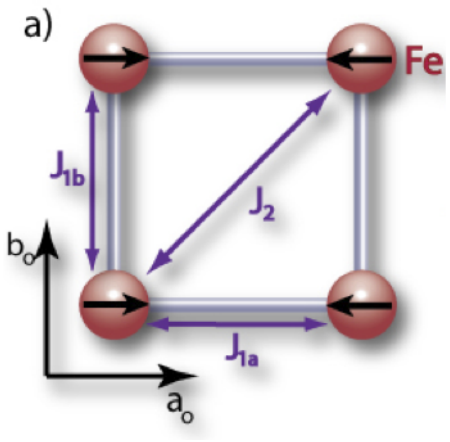

Figure 2.9: Configuration of exchange constants and planar magnetic ordering for $A\mathrm{Fe}_2Pn_2$ families, with A=Ca, Sr, Ba. Magnetic coupling is negative out of the plane. Figure from (12)

the structural transition in in the $A\mathrm{Fe}_2Pn_2$ type compounds, and the demonstration of strong spin exchange anisotropy(126; 12) is an indicator of strong spin-lattice coupling in the iron plane.

Calculations have shown evidence of strong spin-phonon coupling. The calculated impact of phonons on the electronic density of states is remarkable, with displacements of less than 0.01 Å between the Fe-As atoms impacting the magnetic moment of the material calculated by DFT(110). Further, these studies show that the magnetic moment and spin resolved electronic density of states vary significantly when subjected to phonon displacements, with phonons modulating the $Fe - As$ layer having the greatest impact on the the eDOS. The bands close to the Fermi level depend strongly on the distortion from the iron d-bands, and phonon modes coupling to the bands close to the Fermi level create large fluctuations of the electron density at the Fermi level(110).

It is clear in these compounds that there is an involvement of the lattice either directly involved in the mechanism of superconducting pair formation, or providing the favorable setting for same. Additionally, while conventional electron-phonon coupling that describes the superconductivity in BCS superconductors has been thought not to play a substantial part in the superconductivity of pnictides(103; 105), unconventional coupling methods have been posited. One possibility to explain a superconducting pairing

mechanism that is phonon-based is the idea of spin-phonon coupling, in which the superconducting pairs are created via phonon exchange in the spin channel, rather than in the conventional BCS phonon mediated charge channel(127; 128; 129; 9; 130; 124; 131). This effect would manifest in several ways, one of which is the detection of negative thermal expansion via the Invar effect, resulting from a volume change as the iron sublattice switches between the low-volume low spin state, and the high-volume high spin state via interaction with volume modulating phonons, thought to dynamically controlling the iron spin state(132). Another is a coupling of the onset of long range AF ordering to the structural phase transition, as the two occur at the same temperature in many of the pnictide compounds(7).

Resonant Ultrasound Spectroscopy (RUS) measurements on $BaFe_2As_2$ and $Ba(Fe_{0.92}Co_{0.08})_2As_2$ show a strong softening of the shear elastic constant, which is used to conclude that there is general lattice softening through the structural transition driven by renormalization of the shear elastic constant by nematic fluctuations(133). In this context, the softening of the lattice is a secondary effect, with electronic degrees of freedom taking precedence over elastic, and the structural transition again as consequence of the magnetic ordering.

Further, high resolution lattice studies using capacitative dilatometry show small but definite changes in the lattice of $Ba(Fe_{1-x}Co_x)_2As_2$ near the superconducting transition temperature, in both the a and c direction(13) as indicated by a kink in the thermal expansion coefficient at T_c. The thermal expansion coefficient is measured:

$$\alpha = \frac{1}{V}\left(\frac{\delta V}{\delta T}\right)_P$$

A capacity or capacitive dilatometer uses a parallel plate capacitor with one stationary and one moveable plate. As the sample changes, it displaces the moveable plate, changing the gap between the plates, and the capacitance changes as a function of gap size. This method is very sensitive to small changes, and can pick up changes on the order of 100 picometers. In the pnictides, several studies on the cobalt doped systems have been performed using capacitative dilatometry. These studies have shown that there

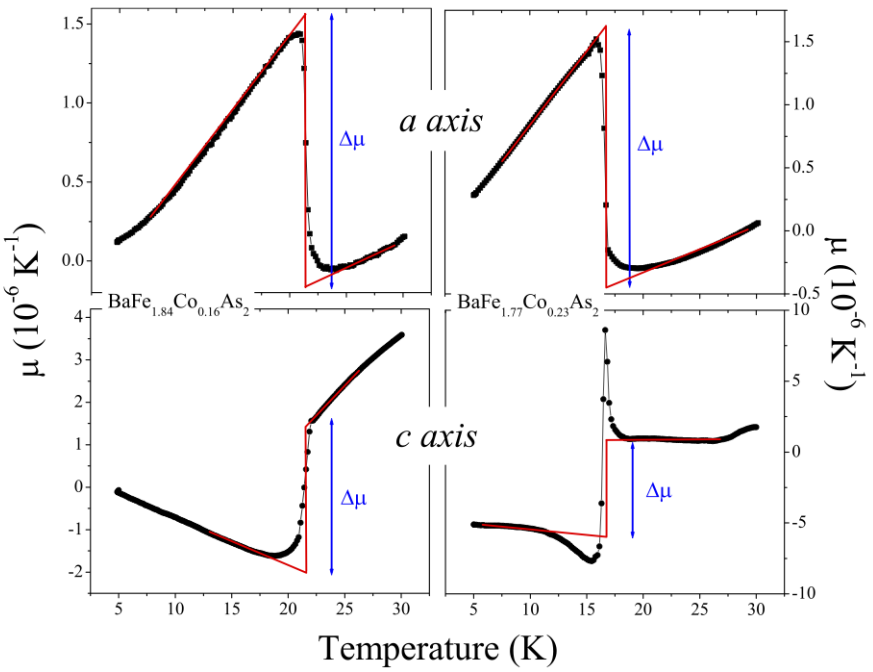

Figure 2.10: Thermal expansion coefficients of a and c axes for $Ba(Fe_{0.92}Co_{0.08})_2As_2$and $BaFe_{1.77}Co_{0.23}As_2$. The thermal expansion coefficient goes negative for the c axis below T_c indicating that the system enters a negative thermal expansion mode. Figure from (13).

is no obvious structural transition for materials in which the AF transition is fully suppressed, but also show a sharp change in the thermal expansion coefficient as the system approaches T_c, which have uniformly shown a change in the thermal expansion parameter near T_c and a sharp discontinuity in the relative length of the c-axis, with a change in derivative of the thermal expansion of the a-axis(134; 13). The presence of this negative thermal expansion along the c-axis and zero thermal expansion along the a axis are both potential indicators of spin-phonon coupling. It is worth noting that there is also a demonstrated sensitivity of T_c to the c/a ratio across a number of superconducting families, including heavy fermion superconductors(135), organic superconductors(136), and cuprates(137).

Iron specific phonon DOS experiments on $BaFe_2As_2$ and $Ba(Fe_{0.92}Co_{0.08})_2As_2$ have measured shifts in optical phonon energies at the structural and magnetic transition(138). Experimental studies on the TA modes of $CaFe_2As_2$ shows a softening of the TA(110)$_{TET}$

mode at the structural transition(139; 140). Further, calculation shows that phonons are very sensitive to the structural details of the FePn_4 layers, with phonon modes that distort the tetrahedra having substantial impact on the electronic density of states close to E_F(110). Further, considering a combination of the structural, magnetic, and orbital effects investigating the instability of all three effects as resulting from quasiparticle excitations on the fermi surface specifically indicates that the structural transition is not the consequence of magnetic ordering(141). Finally, dependence of the magnetic moment of pnictide materials as a function of Fe-As layer separation is well established, and appears universal to pnictide families (10; 9), clearly indicating important links between the lattice and the magnetism.

The parent pnictide superconductors $BaFe_2As_2$, $CaFe_2As_2$, and $SrFe_2As_2$ all exhibit superconductivity under applied hydrostatic pressure(91). While the compounds are very sensitive to the pressure conditions(142), the effect of pressure serving to harden the phonons, which is explained naturally in terms of shrinking the unit cell enabling an increase in lattice energy(138). Nevertheless, a work done on comparing neutron diffraction data of $BaFe_2As_2$ under pressure and substitution on the barium site with potassium showed that the impact of chemical doping is strikingly similar to the impact of pressure, with the reduction in c-axis parameter largely contained in the shrinking of the barium-arsenic bond(118).

Physical properties of FeSC are influenced by the local environment of the iron atoms. The distance of the coordinating atoms from the Fe plane impacts the strength of the observed magnetic moment(10), and most dramatically the superconducting critical temperature(102; 11) (see Fig. 2.8). Further, there is a correlation between spatial blocking of the iron layers, with greater distance between iron layers resulting in higher T_c(143). Local structural effects have been observed in a number of iron based materials. A study combining X-ray diffraction and μSR demonstrates a conflict for electrons between the magnetic and superconducting states in the underdoped region of $Ba_{1-x}K_xFe_2As_2$(144), while x-ray PDF[12] analysis shows no serious local distortions(145). PDF analysis on

[12]See section 4.3.2 for details about the PDF method.

$FeTe_{1-x}Se_x$ shows direct variation in the local environments as a function of doping, leading to ambiguity in the structural phase identification for short atomic ranges(146). A PDF study on non superconducting $BaFe_2Se_3$ demonstrated that introduction of local distortion to the lattice position of the iron atoms was indistinguishable in long range Rietveld refinement, but provides a substantial improvement in the match of the local structural model to the experimental data(147). A study of the superconducting phase of $Fe_{1.01}Se$ demonstrates a modulation of the crystal structure arising from displacements of the iron atoms(148). The presence of planar defects is shown to induce superconductivity and ferromagnetic (FM) in $SrFe_2As_2$, by a stabilization of elastic strain(149). A PDF study conducted on SmFeAsO and superconducting $SmFeAsO_{0.85}F_{0.15}$ shows a distribution of Fe-As distances, and substantial local distortion(150) when compared to the average structural analysis obtained from Rietveld.(151)

2.5 Materials used in this dissertation

2.5.1 Iron pnictides

A majority of this work was conducted on compounds derived from $BaFe_2As_2$ and subsequent chemical substitutions. The reasoning behind choice of this set of crystals is two fold. First, the chemical synthesis process yield single crystals of sufficient size for inelastic neutron scattering (INS), and also produces platelets of appropriate size for IXS (millimeter scale vs micrometer scale). The second reason is that the the crystal structure of $BaFe_2As_2$ accommodates a large array of substitution possibilities into the iron-arsenic layer, enabling parametrized studies that directly probe the atomic influence on the magnetic and superconducting states(121). Further, the structure of $BaFe_2As_2$ also supports the partial to full replacement of the the Ba atoms with Sr, Ca, K, and Rb, providing additional avenues to study the dynamics of the blocking layers between the iron planes. The structural motif of AFe_2Pn_2 compounds is shown in Fig. 2.5.

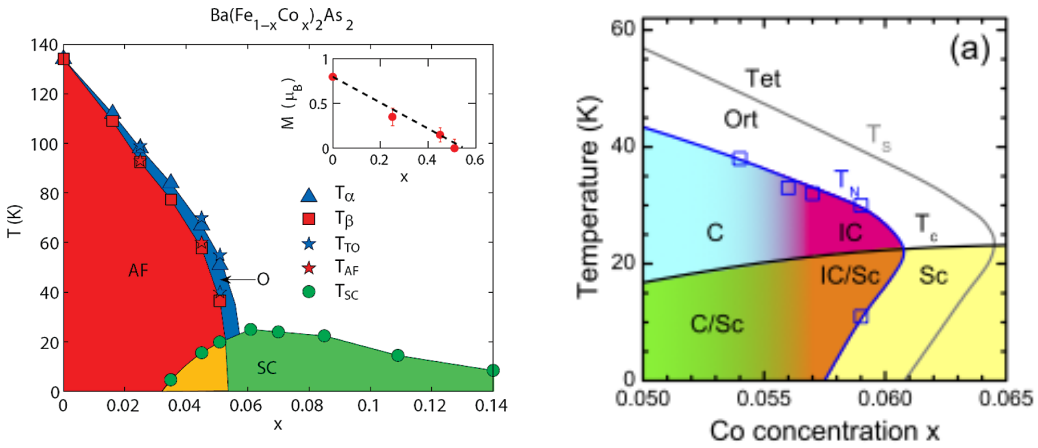

Figure 2.11: Representative phase diagram of $BaFe_2As_2$ with Co doping on the Fe site. General phase diagram on the left(14), while the right shows static incommensurate order near the superconducting phase boundary(15)

At room temperature, $BaFe_2As_2$ is a tetragonal ($I4/mmm$) paramagnet with electronic properties of a poor semimetal(115). At T $\approx$ 140 K, $BaFe_2As_2$ undergoes a structural transition to orthorhombic ($Fmmm$) symmetry displaying a sharp jump in resistivity(3), and magnetically orders with spins AF along the a-axis in the iron plane, FM along the b-axis, and AF between the iron layers with an ordered moment of 0.87(3)-1.04 μ_B per Fe site(152; 153). Electron, hole, and isovalent substitution all induce superconductivity, and regions of static magnetic order exist into the superconducting phase(14; 154), including a region of incommensurate order persisting further into the phase diagram than commensurate order(15)(see Fig. 2.11 for phase diagrams.).

In the structural transition, the iron arrangement goes from a square 2.8Å on a side to a rectangle 2.79Å by 2.81Å on a side(121). The AF transition temperature is suppressed with hole(86; 87; 88),electron(89; 90), or isoelectronic doping(92; 93), eventually giving way to superconductivity.

The observed and calculated magnetic properties of $BaFe_2As_2$ are very sensitive to small details of the structure. The measured moment predicted by DFT calculations (of the order of 1.75-2.4 μ_B(115)), and varies directly as a function of Fe-As layer separation. Calculations show extreme sensitivity to magnetism and structural details, with the

change in the As height, and orientation of the Fe-As bond to the magnetic moment all having pronounced effects on calculations. The structural distortion is small, but the magnetic exchange anisotropy is very large when the exchange constants are calculated from an anisotropic Heisenberg model calculation which includes damping with very small interlayer magnetic coupling(12). This puts the precise specification of $BaFe_2As_2$ as either an itinerant magnetic system or local moment system into question.

Experimental results on lattice effects in $BaFe_2As_2$ compounds show disparity. In some cases, there is little impact of doping(106), while experiments on hole-doped $Ba_{1-x}K_xFe_2As_2$ show substantial broadening of phonons at the AF wave vector(155). The agreement of phonon calculations with experiment are improved by relaxing the strength of the Fe-As bond(156; 106), and explicitly including magnetism(110; 157), although the orientation of the phonon with the magnetic ordering vectors leads to a conclusion that higher frequency modes are more influenced by magnetism(106).

Understanding the dynamics of the Fe-As tetrahedron is an important step as the iron spin state is theoretically shown to be coupled to the degree of As-As hybridization(132), and the phonon modes which modulate the Fe-As tetrahedron have the greatest impact on the electronic density of states at the Fermi level(110; 157). Further, Cooper pair formation occurring in the spin, rather than the charge channel is possible due to the strong magnetoelastic coupling in the system(9). This picture is further enhanced when discussing specifically the magnetoelastic interaction which may be the driving force behind the structural transition(158; 159).

2.5.2 Iron Chalcogenides

Iron chalcogenides are another form of FeSC having form $FeTe_{1-x}Se_x$. The chalcogenides are formed from the square planar layer of iron coordinated with a chalcogen ion, commonly Se or Te. Varying the site substitution (Se,Te) induces superconductivity near 8K. The structural motif of iron chalcogenides is shown in Fig. 2.5.

For this thesis, the iron chalcogenides were studied as a function of sulfur, selenium dopings when treated in varying ethanol concentrations, after reports that commercially available alcohols were able to induce superconductivity with a high volume fraction(160)

The changes in local atomic structure were studied using neutron PDF analysis to understand the interatomic substitutions in the system, and what induces the changing conditions that enable superconductivity in treated compounds, yet show the absence of superconductivity in the as-grown samples.

3

Structure, Phonons, and Magnetism in Condensed Matter

A basic grounding in condensed matter physics is assumed for the reading of this dissertation. The aim of this chapter is to review the concepts most pertinent to understanding the presentation of the experimental results.

3.1 Crystal Structures

Given the number of degrees of freedom in a real system, numbering in the order of 10^{23}, things would be completely intractable if there were no simplifying scheme. Fortunately, a major simplification to approach theories of solids is provided by the periodicity of the crystalline lattice. Simplifying structural, dynamic, and correlational calculation, the theoretical grounding of condensed matter physics is the notion of lattice periodicity.

The crystalline lattice is a mathematical construct that describes the presence of identical environments in space. A structure is used to define the entity that comprises a lattice with a basis, where the basis describes the relative orientation of atoms at each lattice point.[1] Because of the spatial periodicity of the lattice, a number of symmetry classes exist that describe the relative translations, rotations, and mirroring that can occur to the system to leave it invariant. These processes give rise to the different

[1]The terms lattice and structure are often used interchangeably, with relatively little damage, but it is worth emphasizing that the mathematical distinction exists.

classes of crystals, comprised of the smallest units of space that can meet the translational invariance requirement (unit cells). There are seven types of unit cell lattices, fourteen when inversion symmetry is considered (the *Bravais* lattices). Frequently, one can represent the lattice using a small portion of the unit cell known as the asymmetric unit, which is translated through the symmetry operations of the group to recreate the structure in space.

3.2 Lattice Dynamics

The term “lattice vibrations" describes the collective motion of the atoms within a structure. Lattice vibrations give rise to a number of effects in real materials, which require their explicit consideration in the development of equilibrium states in a system. Most explicitly, the lattice vibrations play a large role in any system that are not fully dominated by the electronic system at equilibrium. First, the lattice vibration is fully responsible for the observed thermal expansion of solids, with melting being an extreme case. Zero point vibrations in a system are quantum effects that alter the ground state configuration. The vibration of the lattice contributes substantially to the specific heat of a system. Most pertinent to this work, lattice vibrations provide the pairing glue for the superconductivity described by the BCS theory[2]. In the expanding universe of complex materials that exhibit coupling between the charge, spin, and lattice degrees of freedom, lattice vibrational effects are likely to play an important role in describing the equilibrium properties of the solid states.

The vibrational motion of atoms in a solid is determined mostly by the nuclear potential energy of the atomic arrangement. While the specific details of how the lattice comes to be arranged in a particular manner are complex, the lattice vibrational component can be considered a system of coupled harmonic oscillators that fully specify normal modes of the system. The quanta of lattice vibrations are quasiparticles known as phonons, which obey Bose-Einstein statistics.

[2]See Sec. 2.2

Most condensed matter texts contain a lengthy work up of the theory of lattice vibrations in crystals[3], but we discuss a few things briefly. First, we consider the total potential energy U as some function of the potential energy ϕ between atomic sites $\mathbf{R}$ and $\mathbf{R}'$:

$$U = \frac{1}{2}\sum_{\mathbf{R}\mathbf{R}'} \phi(\mathbf{R} - \mathbf{R}') \tag{3.1}$$

If the atoms execute a displacement $\mathbf{u}(\mathbf{R})$ or $\mathbf{u}(\mathbf{R}')$, Eq. 3.1 may be expanded:

$$U = \frac{1}{2}\sum_{\mathbf{R}\mathbf{R}'} \phi(\mathbf{r}(\mathbf{R}) - \mathbf{r}(\mathbf{R}')) = \frac{1}{2}\sum_{\mathbf{R}\mathbf{R}'} \phi(\mathbf{R} - \mathbf{R}' + \mathbf{u}(\mathbf{R}) - \mathbf{u}(\mathbf{R}')) \tag{3.2}$$

If one assumes that the atoms vibrate harmonically around their equilibrium positions, one can expand U in a taylor series. In doing so, one finds that the constant term is the equilibrium lattice potential from Eq. 3.1, the first linear term goes away (as it is the opposing force against the lattice, so it must go away in the equilibrium state), and the quadratic term is the harmonic term, written:

$$U^h = \frac{1}{4}\sum_{\mathbf{R}\mathbf{R}'} [u_\mu(\mathbf{R}) - u_\mu(\mathbf{R}')]\phi_{\mu\nu}(\mathbf{R} - \mathbf{R}')[u_\nu(\mathbf{R}) - u_\nu(\mathbf{R}')] \tag{3.3}$$

where the μ, ν describe cartesian directions, and $\phi_{\mu\nu}$ describes the second partial derivative of the potential. At this point, the problem essentially reduces to a system of coupled harmonic oscillators. In three dimensions, the eigenvector solutions describe the polarization of the phonon modes, while the eigenvalues the normal mode frequencies. This model, called the *harmonic approximation*, is the most mathematically appealing, but higher order considerations are invariably required to discuss real materials. The third and fourth order terms of the taylor expansion of U are included in *anharmonic* theories. The anharmonic theory is required to explain many properties of real solids, including thermal expansion and thermal conductivity.

[3] See Ashcroft, Ch. 22-26 (161), Wallace, Chapter 2-3(162), and Bruesch (163)

The lattice vibrational quanta are directly measurable by spectroscopic probes, notably neutron scattering. Full dispersion maps are obtainable, along with direct information about normal mode population, thermal expansion, and electron-phonon interactions. Anharmonicity of the lattice is also detectable by spectroscopic probes, as the lattice anharmonicity impacts the phonon lifetime, and a direct measurement of the one-phonon line width will provide information about the anharmonicity of the system.

3.3 Electron-Phonon Coupling

In traditional metals, electron-phonon coupling is always present, arising from the residual electron-ion interaction. This interaction is commonly neglected in the most electronic approximations, due to the orders of magnitude difference between phonon energies (of order 0.01 eV) and typical Fermi energies (of order eV)(163). Further, the role of conduction electrons is commonly viewed as a method of screening the positive ionic cores from one another. Because the conduction electrons are highly mobile, with a velocity much higher than that of the ionic cores, the screening activity is virtually instantaneous, and serves to stabilize the lattice.

Though this phenomenological picture is appealing, the inter-ion forces are complex, and must be extended to higher order terms even in the simplest metals. These more complex terms are the result of anharmonicity and indicate the presence of interactions further than that of the nearest neighbors.

There are a few classic examples of traditional electron-phonon coupling that can impact material properties. The first of these arises in cases where an abrupt change in the screening power of the electrons can be observed at $|\tau + \mathbf{q}| = 2\mathbf{k_F}$, which is known as a Kohn anomaly(164). In the Kohn anomaly, the electrons suffer a loss of screening ability for phonons with a wave vector $\mathbf{q} > 2\mathbf{k_F}$, greatly enhancing the ionic interaction, which can result in a lattice instability in extreme cases.

3.4 Magnetism

Magnetism as a term most generally describes the preferred orientation of electronic spins within a system. Magnetism has been known to humanity for millennia, yet theories of magnetism remain markedly underdeveloped. Simple square lattice systems with nice coordinated sites like the Ising or the Heisenberg systems are fairly well understood. A particular problem arises in metals when electrons are no longer fixed to particular atomic sites, and are free to move around as the Coulomb potential dictates. Nevertheless, a few key points are tractable with some elementary physics application. Many of the concepts here are covered extensively in condensed matter texts, and more comprehensive discussions of these descriptions are can be found in more canonical sources. (161; 165; 166)

First, considering two electrons in a simple system like the infinite square well. Due to the Pauli principle, the two electrons may not be in precisely the same quantum state. If the two electrons have the same spin direction, their wave functions will not overlap if the electrons are in the same energy level. Therefore, we can see that a direct consequence of the spin order is a sensitivity of the ground state energy to the spin-separation distance.

3.4.1 Spin Waves

In a magnetically ordered material, below some characteristic energy, the spin system is rigidly fixed to the ionic cores. Above this energy, the interaction of a neutron of sufficiently high energy with the spin system can result in a disturbance to the magnetic ordering, known as a spin wave (Fig. 3.1). Quantized spin waves in condensed matter systems are known as magnons, possess dispersion, and can be studied with INS.

3.4.2 Itinerant magnets

Itinerancy is the problem alluded to in the beginning of the section dealing with non-localized electrons. An itinerant system has mobile spin carriers, and has consistently

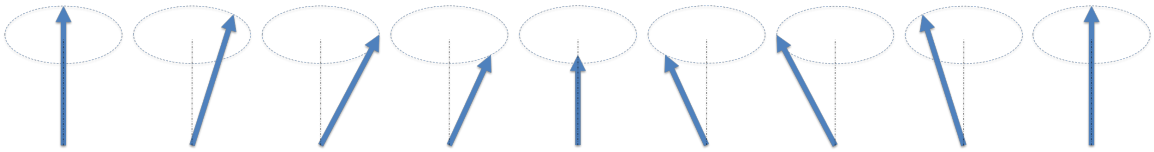

Figure 3.1: Schematic of a spin wave excitation. (left) fixed atomic moments in the lattice. (right) disruption of the moment arrangement with by a neutron results in a wavelike distribution of the moments with wavelength λ_{SW}.

eluded ideal description for over a century. Itineracy can arise in a ferro- or antiferromagnetic state, so consistent theories for the different configurations are required. Two main mechanisms for dealing with such mobile spin carriers are the Stoner model and the spin fluctuation model.

The Stoner model of itinerant magnetism builds on the case of Pauli paramagnetism. Pauli paramagnetism takes into account the density of states at the Fermi level, and compensation of spins:

$$\chi_P = 2\mu_B^2 N(E_F) \tag{3.4}$$

The Stoner model is closely related to the Weiss model for ferromagnetism. In the Stoner model, the magnetic carriers are unsaturated spins in the d-band, the exchange is done through a Weiss-like molecular field term, and Fermi statistics are obeyed. The major success of the Stoner theory is that it accounts for non-integer magnetic moments found in transition metal compounds by dealing directly with band-filling and the interaction between the electrons in the valence band. The Stoner framework modifies the Pauli paramagnetic susceptibility, enhancing it through the exchange interaction:

$$\chi_S = \frac{2\mu_B^2 N(E_F)}{1 - IN(E_F)} \tag{3.5}$$

The "Stoner exchange parameter" I controls the onset of the magnetic state - if the denominator is negative, the paramagnetic state has a higher energy than all magnetic configurations, so the system must be magnetic. The magnetism onset criterion is more

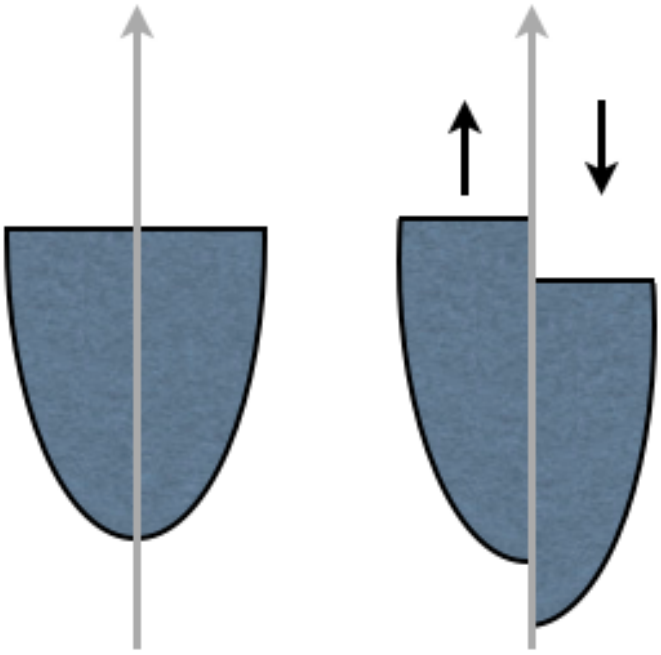

Figure 3.2: Illustration of the shift in the band population caused by the presences of static magnetism in an itinerant system.

succinctly stated as: $IN(E_F) \geq 1$ which would make the denominator in Eq. 3.5 less than 1. The zero-temperature version of the theory is not well supported, as it predicts that the Curie temp scales linearly with the magnetic moment, which is not experimentally validated, and the framework can really only be applied to very weak itinerant systems.

Unfortunately, the Stoner model fails rather badly at any finite temperature greater than zero.(167; 168; 169) The main difficulties remain that the temperature dependence of the observables is too weak, and does not match experimental observation. Further, the Stoner model does not capture the effect of a finite paramagnetism above the Curie/Neel temperatures, meaning it is qualitatively incorrect in these circumstances. The Stoner model does qualitatively allow the presence of magneto-elastic phenomena, explaining this through a mechanism of spin exchange. In this model, one allows a removal of

electrons from the spin-down bonding state, transferring them them to the spin-up anti bonding state, which results in a weaker bond and expanded lattice.

To describe the behavior of itinerant systems, a greater degree of success has been obtained with the spin fluctuation concept of Moriya.(170). In the spin fluctuation model, the notion of a well-defined locally precessing spin-wave[4] goes away and is replaced by a local fluctuation in the magnetic moment or spin density. The spin fluctuation theory grows out of gaussian statistics, where it is assumed that in equilibrium, physical properties of a system will fluctuate around some mean value. In this way, a locally fluctuating vector magnetic moment may be defined:

$$\mathbf{m}(\mathbf{r}) = \frac{1}{V}\int (\mathbf{m}(\mathbf{r}))^n dV \tag{3.6}$$

where n is the order of an expansion, and the fluctuation is zero for odd orders from symmetry. If one defines a locate moment $\mathbf{M}$ parallel to one axis of a coordinate system, one may see immediately that there are three orthogonal fluctuation components, one parallel to $\mathbf{M}$, and the other two perpendicular (Fig. 3.3). The total moment at a site is given by the sum of the moment $\mathbf{M}$ and the fluctuations around $\mathbf{M}$, where one sums over the spatial dimensions in the coordinate system.

The fluctuations at temperatures greater than T_c lose spatial correlation, making the parallel and perpendicular components degenerate. Taking the second derivative of the free energy with respect to the magnetization, one finds that at T=T_c, the fluctuation amplitude has a finite value:

$$\langle m_c^2 \rangle = \frac{M_0^2}{5}$$

Which leads to an expression for the finite temperature dependence of the spin fluctuations:

$$\langle m_c^2 \rangle \frac{T}{T_C} = \frac{M_0^2}{5}\frac{T}{T_C} \tag{3.7}$$

[4]See Sec. 3.4.1.

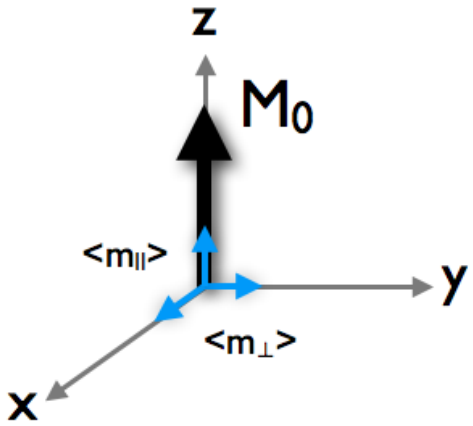

Figure 3.3: Demonstration of static magnetic moment M_0 (thick black arrow) with spin fluctuation components (small blue arrows). The spin fluctuations represent gaussian disruptions in the spin density around the static moment.

This formulation shows that the reduction of the static moment at low temperatures is greater than for the Stoner model, because the thermal activation energy of the fluctuations is much less. Further, the Moriya model of the spin fluctuations allows the explicit presence of paramagnetism above T_c, and better approximates the magnitude of the static magnetic moment below the magnetic transition temperature. Due to the proximity of the cuprate superconducting state to an AF insulating state, spin fluctuations have been discussed extensively as a mechanism for binding superconducting pairs in HTSC. Finally, the spin-fluctuation mechanism is also implicated in magneto-volume coupling, where the magnetic contribution to the thermal expansion coefficient is given by the spin-fluctuation amplitude:

$$\alpha_m = \frac{d\omega}{dT} = \begin{cases} \frac{1}{T_C}\left(\frac{V_{NM}}{V_0} - 1\right)\left(1 - 3\frac{\langle m_c^2\rangle}{M_0^2}\right), & \text{if } T < T_C \\ \frac{1}{T_C}\left(1 - \frac{V_{NM}}{V_0}\right)\left(3\frac{\langle m_c^2\rangle}{M_0^2}\right), & \text{if } T \geq T_C \end{cases} \tag{3.8}$$

where V_{NM} is the non-magnetic contribution to the volume, and ω is the relative volume change(171). The magneto-volume interaction, critical in solids that display Invar behavior, may play an important role in the lattice dynamics of FeSC.

3.5 Spin Phonon Coupling

The magnetic and lattice degrees of freedom can cooperate to give rise to new effects, and this phenomena is generally known as spin-phonon or spin-lattice coupling. As an example of spin-lattice coupling, one can consider electron kinetic energy. In a metal, the Pauli exclusion principle results in the reduction of the overall volume to reduce the electron kinetic energy, making the magnetic state of a system have a higher volume than the non-magnetic state. This behavior contributes to negative or zero thermal expansion of some iron alloys, and is known as the Invar effect.

The presence of magnetic materials and observation of strong electronic properties force us to consider behaviors that implicate both magnetic and elastic properties. One such mechanism can be found in magnetoelastic behaviors. In magnetoelastic phenomenon, the magnetic and elastic properties of a material are coupled, a behavior which can strongly impact the elastic behavior in a solid. Microscopically, the dominant contribution to magnetoelasticity comes from the crystalline electric field, and a Hamiltonian describing the different contributions to the behavior can be written:

$$H_{tot} = H_M(\mathbf{M}, \mathbf{H}) + H_{ME}(\mathbf{M}, e_{ij}, w_{ij}) + H_E(e_{ij}) \tag{3.9}$$

Where H_M describes the magnetic properties of the solid, H_E describes the elastic properties of the non-magnetic solid, and H_{ME} is the magnetoelastic portion describing the coupling. $\mathbf{M}$, $\mathbf{H}$ describe the magnetic variable and applied magnetic field, and e, w describe the symmetric and antisymmetric elastic strain tensor(172). Using this Hamiltonian, and standard free energy calculations, one can determine the static properties of the system, including the magnetostrictive distortion of the lattice, magnetoelastic contributions to magnetic anisotropy, and magnetoelastic contributions to the elastic stiffness moduli(172; 173).

One manifestation of magnetoelasticity is magnetostriction, a type of strain resulting from the difference between magnetoelastic and elastic contributions to the lattice. In such a situation, the magnetoelastic contribution of the system is derived from the

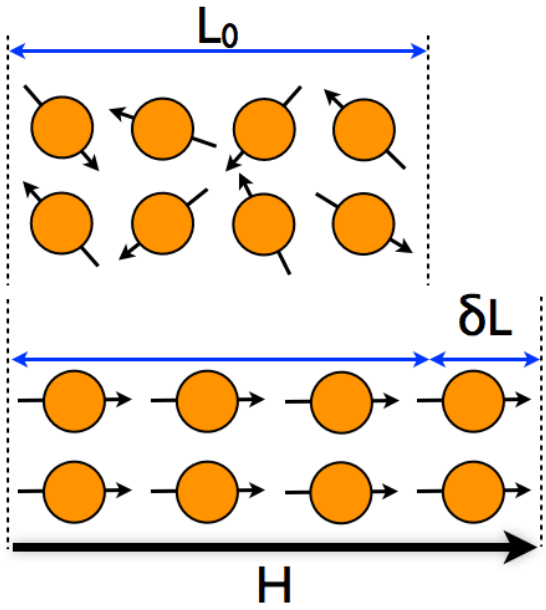

Figure 3.4: Simple illustration of magnetostriction. In a magnetically disordered system (top) the distribution of magnetic moments has no definite spatial correlation. When a magnetic field is applied, the ordered state is larger than the disordered state by a factor δL due to the presence of the ordered magnetic moments.

interaction between spin moments of electrons coupling to orbital motion of electrons around nuclei, and the elastic energy is provided by deformation of the crystalline structure(173). Upon application of a magnetic field, the there is a change in the size or shape of the material (Fig. 3.4). In some cases, the coupling between the elastic and magnetic degrees of freedom are dominant considerations in the elastic behavior of a solid, with magnetoelastic phenomena giving rise to lattice instabilities or structural phase transitions which lower the crystalline symmetry(174; 175).

The nuclear spin may also couple to the magnetically ordered lattice(172). For a metallic material, the coupling of the lattice strain and the conduction electrons can give rise to an internal magnetic field that then couples to the nuclear magnetic dipoles. An alternate route is obtained when beginning with a magnetically ordered solid where the lattice strain couples to the electronic dipole moments, which then couple to the nuclear dipole moments via the hyperfine interaction to produce a magneto elastic coupling

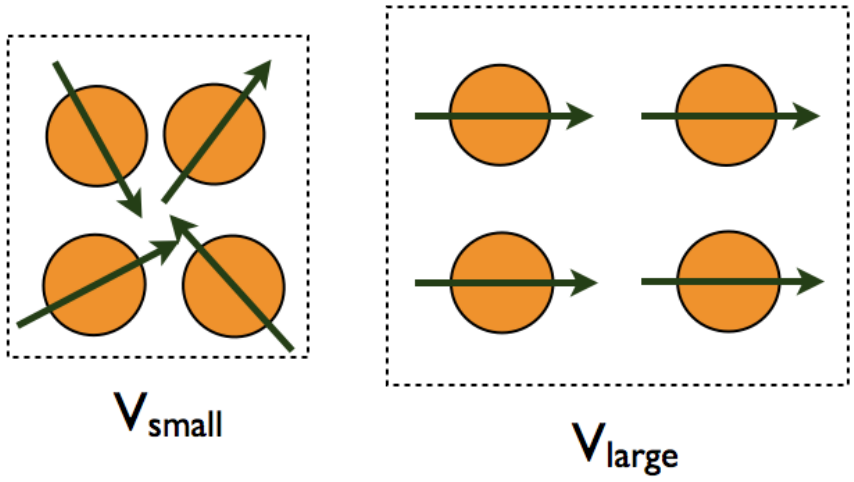

Figure 3.5: Simple illustration of the magnetovolume effect. In a magnetically disordered system (left) the distribution of magnetic moments has no definite spatial correlation. In the presence of a larger volume, the magnetic moments may align due to loosening of the spatial restriction of the Pauli principle.

effect. These effects are typically negligible, but worth mentioning given speculation regarding the role of hyperfine couplings between the iron and arsenic atoms in FeSC.(95) Further, nuclear spins with an electric quadrupole moment can be coupled to the elastic strain by the changes in the electric field gradient at the nuclear position induced by lattice vibrations.(172)

Another evidence of strong spin-phonon coupling would be the presence of an unexpectedly strong scattering resulting from the magneto-vibrational (MV) effect. MV scattering is a mirror image of the phonon spectrum in the spin channel. The nominal cross section for MV scattering is orders of magnitude lower than that of nuclear scattering. In the event of a strong spin-phonon coupling, the scattering intensity may increase to the order of the nominal magnetic scattering(176). One can distinguish the MV component of the scattering with polarized neutron scattering. The nuclear component is NSF while the MV component is SF for a centro-symmetric system.(177)

The coupling between these degrees of freedom has recently been demonstrated to play an important role in the formation of the magnetic state in $BaFe_2As_2$(19). Spin-lattice

coupling is also indicated in the AFePn systems, with a strong anisotropy in the Fe-Fe exchange constants(12; 126) The coupling of the spin and lattice degrees of freedom for HTSC has long been pushed by a relatively small crew of researchers who recognized the coupling of these roles could have crucial effects, and needed further exploration.

3.6 Structural Heterogeneity

A degree of structural homogeneity is required for the current framework of condensed matter physics. Electronic structure calculations are limited in their ability to accommodate distortions, and structural solutions for diffraction require large coherent domains. Nevertheless, real materials are frequently found to deviate from the ideal structure. This frequently gives rise to different electronic states, such as the ferroelectric transition in $BaTiO_3$ precipitated by a large shift in the local organization of the atoms, or dynamic charge stripes as seen in the cuprate superconductors are a type of dynamic phase separation which minimizes the Coulomb energy, and occur on a long length scale.

Many first-principles approaches to condensed matter problems rely on a periodic basis for computation. To be sure, the power of crystalline periodicity provides us with sufficient coherent scattering to perform structural determinations, and provides the basis for electronic structure calculations of high accuracy. Nevertheless, this condition of perfect periodicity is insufficient to describe the behavior of real materials. While the majority of atoms can be found to occupy an average translational symmetry, localized defects and distortions from the periodicity are increasingly recognized to play a crucial role in the functional and electronic behaviors of materials.

Part of the restriction on understanding local heterogeneity is computational. The total number of particles interacting in any system is well outside the scope of current computing power. Reasonable approximations may be made to reduce the system size, but special care must be taken to avoid errors in the approximation, as this will naturally

serve to reduce the reliability of the solutions. The size of computational simulation scales in at least a linear, and more often a quartic manner with the system size. [5]

Approximations that are commonly used in structural calculations are the Born-Oppenheimer approximation, where it is assumed there is no coupling between the electrons and ions, and the Hartree Fock theory, where the true many body wave function is replaced by a single Slater determinant of electron orbitals accounting for spin and space components. Hartree-Fock theory neglects the degree of correlation between the electrons, rather placing the individual electrons in an average potential derived from the surrounding electrons. HF theory is limited by the choice of basis function used to describe the orbital system, and has questionable accuracy in standard systems, and is outright incorrect in systems with a high degree of expected correlation, though it is frequently used to understand systematic dependencies on extensive variables.

Density functional theory also treats the system in a non-interacting limit, and does not result in a correlated wave function. The essential practice of DFT theories is to treat the electronic density of the system as a functional, and declare victory on discovery of the ground state when the electronic-density functional is minimized. DFT accuracy again suffers with the degree of correlation in the studied system. Approximations used in a DFT framework include the LDA, where the value of the exchange energy is explicitly accounted for, using an exchange functional. LDA does best in systems where the charge densities vary slowly, but the bonding strengths are typically overestimated resulting in shortened bond lengths. Further LDA neglects short range van der Waals bonding, and does not do well with hydrogen bonding.

Frequently, pseudopotentials are applied to reduce the fluctuation complexities associated with atomic core electrons, which has the effect of smoothing out the wave function and reducing the overall number of basis functions required[6].

[5] i.e., in the case of Quantum Monte Carlo (QMC), the the computational cost scales with the cube of the number of electrons in the system, at a minimum, and there are additional scaling factors associated with the Z value of the atoms involved(178).

[6] Pseudopotential methods are also used in DFT calculations

Computational effort has been expended in bringing some understanding to the phenomena of heterogeneity. In a work exploring a phenomenological approach, Alvarez *et. al.* recognize the Hubbard and t-J models to be at their useful limit,(179), drawing strong analogy with phase separation in the manganites, shown to result in a number of the complex behaviors exhibited by such systems(180)

We take this very long tangent into the question of structural heterogeneity, as it is important to understanding the work that will be presented here. In the FeSC superconductors, traditional DFT methods have trouble reconciling the structure with the electronic properties, sometimes predicting the correct magnetic order, but getting the lattice parameters incorrect. All of this raises questions regarding the source of such structural heterogeneity in materials. Is the heterogeneity the result of randomly distributed local distortions, or is it a hallmark of inherent material instability?

4 Particle Scattering

This chapter will provide background in the physics of scattering neutrons and x-rays from crystalline solids. General statements about scattering and terminology are presented the first section, then information about the preparation of radiation beams for use in neutron and x-ray scattering experiments will be presented. The reader familiar with these experimental techniques may skip this chapter, and the novice may find it to their advantage to carefully review the numerous references on the subject.

Neutron scattering experiments comprise the bulk of the experimental work for this dissertation, so the following chapter pays proportionally more attention to neutron scattering. The works of Squires(181), Lovesay(177), Shirane *et. al*(1), and the famous primer by Pynn(182). are particularly recommended for neutron scatterers looking to gain a firm understanding of the material presented here.

The only connection with x-rays for work done in connection with the dissertation material presented here is for IXS and Nuclear Resonant Inelastic X-ray Scattering (NRIXS) studies, so these will be the focus. The work of Burkel(183) is a comprehensive study in inelastic x-ray scattering, with a progress report issued in 2000 highlighting advances in application of the technique to phonon studies(184). There are copious volumes available on the subject of x-ray scattering used for elastic diffraction purposes,

including Warren(185), Guinier(186), and the comprehensive work on neutron and x-ray diffraction by Pecharsky and Zavalij(187), and readers interested in a more thorough treatment are encouraged to seek out these volumes.

4.1 Scattering Formalism

Most generally, particle beam scattering measures the dynamic scattering function, $S(\mathbf{Q},\omega)$ the dual fourier transform of the time dependent pair correlation function:

$$S(\mathbf{Q},\omega) = \frac{1}{2\pi\hbar N}\sum_{ll'}\int_{-\infty}^{\infty} dt\langle e^{-i\mathbf{Q}\cdot\mathbf{r}_{\mathbf{l}'}(0)} e^{i\mathbf{Q}\cdot\mathbf{r}_{\mathbf{l}}(t)}\rangle e^{-i\omega t} \tag{4.1}$$

The physical meaning of this is that the scattering process measures the fourier transform of the probability amplitude of finding a particle at a position $\mathbf{r}$ and time t knowing that a particle was at some given location $\mathbf{r_0}$ at some earlier time t'.

The particles used as probes in the experiment couple to a field in the sample, and the information collected from the scattering can be used to deduce the properties of the sample. Experimentally, the picture is defined as follows. An incoming particle of energy E_i and momentum $\mathbf{k_i}$ enters the scattering system, and through an interaction with the scattering system is scattered through an angle 2θ to a final energy E_f and final wave vector $\mathbf{k_f}$, and total momentum transfer $\mathbf{Q}$. The definition of incident and final wave vector specifies the momentum transfer, and is in some cases referred to as the "scattering triangle" (figure 4.1). Particle beam scattering directly measures properties of reciprocal and frequency space, so the technique is best suited to directly measure properties that can be expressed in these coordinates, such as phonons and crystal structures.

Signals from particle scattering have four four classifications: elastic, inelastic, coherent, and incoherent. Processes are identified by one energy term (elastic or inelastic) and one phase term (coherent or incoherent). The energy term describes whether the scattered particle energy remains unchanged (elastic case), or has a definite change in energy after interaction with the sample (inelastic). The phase term describes whether

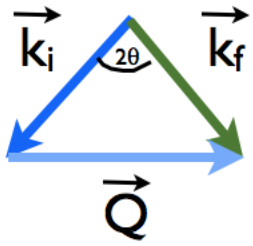

Figure 4.1: Definition of momentum transfer vector and the scattering triangle. This relation holds for all particle scattering studies. In the case of elastic scattering $|\mathbf{k_i}| = |\mathbf{k_f}|$, while for inelastic scattering $|\mathbf{k_i}| \neq |\mathbf{k_f}|$

a definite phase relationship exists between the scattered particles and there is definite interference effects (coherent scattering), or whether there is no phase relationship, and all of the scattered particles have different relative phases (incoherent). Examples of different scattering processes are listed in table 4.1.

Table 4.1: Example scattering process classifications.

Scattering Processes	Elastic	Inelastic
Coherent	Bragg Scattering	Phonons, Magnons, thermal diffuse scattering (TDS)
Incoherent	Nuclear Spin, Laue Monotonic Diffuse	Compton scattering

4.2 Neutron Scattering

Neutrons are powerful probes of bulk material properties. In 1948, Wollan and Shull were able to show that neutrons could be used for structural analysis on crushed powder specimens in a manner analogous to X-ray diffraction(188), as the wavelength of a thermal neutron is of the order of interatomic lattice spacings. Also, the energy of neutrons used in condensed matter studies have an energy near that of dynamic

phenomena, so neutrons can probe dynamical features like phonons, as first shown by Brockhouse(189). Further, neutrons possess a magnetic moment, and can interact with unpaired electrons to study the magnetic structure. Finally, the ability to spin polarize neutrons can be exploited in the studies of the magnetic dynamics of materials like spin waves and magnetically coupled phonons.

The neutron primarily interacts with nuclei via the weak force, scattering predominantly from the very short range nuclear potential. Because the scattering interaction is very weak, the neutrons are able to penetrate very deeply into materials, and neutron scattering is less destructive to samples than other material probes like x-rays or electrons. Also, the scattering cross section for neutrons varies across the periodic table, and even from isotope to isotope, and this property allows the experimenter to contrast scattering from different isotopes. By using isotopic contrast, an experimenter can better understand the contribution to the dynamics of the different elements in a compound, and can complement x-ray studies.

The major drawback to neutrons are the flux limitations and infrastructure required to operate a neutron facility. Neutrons are produced in nuclear reactors or spallation sources. The development of neutron source fluxes as a function of time is shown in Fig. 4.2. A number nearing 10^{15}n-cm^{-2}s^{-1} appears in Fig. 4.2, but it is important to note that this is the peak flux for the entire facility. At a specific beamline, such as the CNCS at the SNS, the flux rate is much closer to 10^{5} n-cm^{-2}MW^{-1}s^{-1}, meaning a substantial portion of the flux is lost between the spallation reaction and the beamline. At both reactor and spallation sources, production of a beam of neutrons suitable for a particular scientific application requires several stages of moderation, resulting in flux decreases by orders of magnitude. For comparison, modern synchrotron sources have fluxes up to 10^{18} photons-sec^{-1}mm^{-2}. Further, in part to improve the available flux, neutron facilities are large installations, requiring substantial operation budgets and staffing to operate. Contrasted against x-ray diffractometers, which are standard lab equipment at most universities, the power of the neutron scattering technique and the relatively small number of research venues makes neutron scattering a very demanding and competitive field.

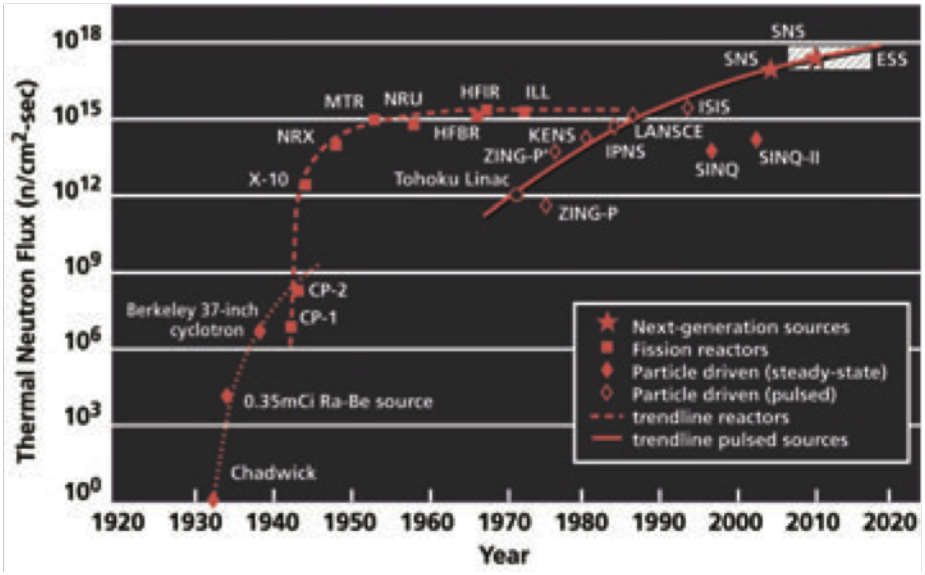

Figure 4.2: Neutron flux distribution as a function of time for domestic and international neutron sources(16).

The following sections will briefly address the mechanisms of neutron production, instrumental details, the mathematical formalism of neutron scattering, and discuss different types of neutron scattering experiments.

4.2.1 Neutron Scattering Formalism

There are several different neutron-sample scattering interactions, a few of which are discussed here. The primary scattering interaction comes from the nuclear force. The nuclear force is sufficiently short-ranged (10^{-15} m), allowing one to treat the neutron as a point scatterer, justified by elementary scattering theory(181; 190). This also allows one to treat neutron scattering in the Born approximation, as the neutron only weakly perturbs the scattering system[1].

Because of the weak interaction between the neutron and the scattering system, one can use “Fermi’s Golden Rule" to establish the formalism using the basis of perturbation theory. In Fermi’s Golden rule, the probability of a particular state transition

[1] i.e., the neutrons may cause a transition in state of the system, but do not *fundamentally* impact or alter the system.

is proportional to the square of its matrix element(191), so the cross section of the interaction of a state $|\phi_i\rangle$ with an arbitrary potential V to become a final state $|\phi_f\rangle$ is written:

$$\mathcal{P} = \frac{2\pi}{\hbar}|\langle\phi_f|V|\phi_i\rangle|^2 n(\epsilon) \tag{4.2}$$

where $n(\epsilon)$ is the density of final states that is available for the system. In the case for neutron scattering, the $n(\epsilon)$ is the number of available final momentum states, which can be determined using box normalization. The final expression for the scattering cross section for the neutron with the sample is written, where λ terms describe the initial and final states of the sample, and $\mathbf{k}$ terms describe the initial and final states of the neutron:

$$\left(\frac{d\sigma}{d\Omega}\right)_{\text{coh}} = \frac{k_f}{k_i}\left(\frac{m}{2\pi\hbar^2}\right)^2 |\langle\lambda_f\mathbf{k_f}|V|\lambda_i\mathbf{k_i}\rangle|^2 \tag{4.3}$$

and to add explicitly the energy dependence, again with λ states describing the sample, and E_i, E_f describing the neutron:

$$\left(\frac{d^2\sigma}{d\Omega dE}\right)_{\text{coh}} = \frac{k_f}{k_i}\left(\frac{m}{2\pi\hbar^2}\right)^2 |\langle\lambda_f\mathbf{k_f}|V|\lambda_i\mathbf{k_i}\rangle|^2\, \delta(E_{\lambda_i} - E_{\lambda_f} + E_i - E_f) \tag{4.4}$$

As the effective potential seen by the neutron is so short ranged, we may treat it as a delta-function, and a lot of ambiguity in the details of the neutron-nucleus interaction can be neglected by replacement of the nuclear potential by a Fermi pseudopotential:

$$V(\mathbf{r}) = \frac{2\pi\hbar^2}{m} b\delta(\mathbf{r}) \tag{4.5}$$

And we can express the scattering of a neutron traveling along the $\mathbf{z}$ direction in the point scattering regime as:

$$\psi_{inc} = e^{i\mathbf{k}\cdot\mathbf{z}} \longrightarrow \psi_{scatt} = -\frac{b}{r}e^{i\mathbf{k}\cdot\mathbf{r}} \tag{4.6}$$

Table 4.2: Summary for absorption data. "Cut-off" is defined as energy of neutrons where the cross section drops below 1000 barns, and is for rough estimation purposes only.

Material	"Cut-off" (meV)	Wavelength (Å)
^{10}B	360	0.48
^{113}Cd	517	0.4
^{155}Gd	260	0.56
^{157}Gd	454	0.42

Where the value of b is the called the neutron scattering length, and is positive in the case of a repulsive interaction. There is no analytical expression of scattering length for atomic nuclei, due in part to underlying complexities of nuclear theory. Each nuclide has a different scattering length, with substantial variation between isotopes, nuclear spin, and the incident beam energy. Experimentally determined tables of scattering lengths are available(192; 1), while energy-dependent data are available from nuclear data centers(193).

In special cases, b is a complex number, and the imaginary component corresponds to absorption of the neutron by the nucleus. This fact is exploited in the design of neutron experiments (e.g., for background reduction). Relatively few nuclides exhibit absorption behavior; the most common varieties used in the field are shown in Tab. 4.2 with their useful energy ranges. The majority of nuclides have scattering lengths with small absorption components and are not affected by the energy of the neutron.

In nuclear scattering, because the potential is treated as a delta function, the fourier transform of the potential gives a $\mathbf{Q}$ independent value for the form factor, meaning that the likelihood a neutron is scattered from the nuclear force has no dependence on the momentum transfer of the interaction.

In magnetic scattering, the neutron is scattered from the electron cloud surrounding atomic sites, specifically interacting with the unpaired electrons. To derive the potential field seen by the neutron, the spin and orbital components of the electron must be included. Using the lowest order expression for a magnetic dipole to represent the magnetic field of an unpaired electron moving with momentum $\mathbf{p}_e$, we can write the

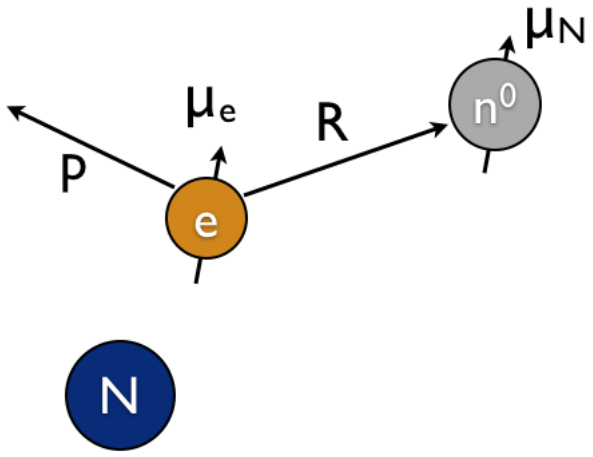

Figure 4.3: Illustration of interaction between a neutron and unpaired electron as occurs in magnetic neutron scattering, illustrating the direction of interaction, and the orbital angular momentum of the electron.

expression for the interaction between the neutron with dipole moment $\mu_{\mathbf{N}}$ in the total field $\mathbf{B}$:

$$-\mu_{\mathbf{n}} \cdot \mathbf{B} = -\frac{\mu_0}{2\pi}\gamma\mu_N\mu_B\sigma \cdot \left(\nabla \times \left(\frac{\mathbf{s} \times \hat{\mathbf{R}}}{R^2}\right) + \frac{1}{\hbar}\frac{\mathbf{p_e} \times \hat{\mathbf{R}}}{R^2}\right) \tag{4.7}$$

Where $\mu_{\mathbf{e}} = -2\mu_B\mathbf{s}$, ($\mathbf{s}$ is the spin operator for the electron), $\mu_{\mathbf{n}} = -\gamma\mu_N\sigma$ (γ is a phenomenological constant equal to 1.913, σ is the spin operator for the neutron). This situation is illustrated in Fig. 4.3.

The situation of magnetic scattering is distinct from that of nuclear scattering in two important ways. The first is that the magnetic interaction is long-range compared to the nuclear scattering potential, and the fourier transform of the magnetic scattering length is dependent upon $\mathbf{Q}$, unlike the $\mathbf{Q}$ independent form factor for nuclear scattering discussed above. Magnetic ions have form-factors dependent upon their spin states and tabulated values required to calculate the form factors are available(194)

Coherence

In addition to the absorption behavior, the issue of coherency of the scattered neutron is important to consider. Coherent scattering maintains a definite phase relationship between the incident and outgoing wave, while in incoherent scattering, this phase relationship is lost. The coherency of a particular sample is reflected in its neutron scattering length. The neutron scattering length for a sample is determined by the scattering lengths of the constituent nuclei:

$$\bar{b} = \sum_r c_r b_r \tag{4.8}$$

and the average coherent cross section:

$$\sigma_{\text{coh}} = 4\pi(\bar{b})^2 \tag{4.9}$$

Incoherent scattering arises in the case of random fluctuations in the potential seen by the neutrons at the scattering site due to $e.g.$ nuclear spin and random atomic displacements. Because of its nature, incoherent scattering is frequently present in scattering samples, but it can be minimized through the use of isotopes with zero nuclear spin. The average incoherent cross section is written in terms of the difference between the total scattering cross section and the coherent component:

$$\sigma_{\text{inc}} = 4\pi\left(\overline{b^2} - \bar{b}^2\right) = 4\pi\overline{(b-\bar{b})^2} \tag{4.10}$$

And the incoherent scattering length:

$$b_{\text{inc}} = \sqrt{\overline{b^2} - \bar{b}^2} \tag{4.11}$$

In some cases, a strong incoherent scatterer is useful, particularly in the case of vanadium, which is used to normalize detector efficiency in neutron scattering experiments.

Cross section

The measured quantity in a neutron scattering experiment is the scattering cross section, or the number of neutrons scattered per second into some solid angle $(d\Omega)$ in some energy range $(E,\ E + dE)$, which directly measures both the coherent and incoherent portions of the sample scattering law $S(\mathbf{Q}, \omega)$:

$$\left(\frac{d^2\sigma}{d\Omega dE}\right)_{\text{coh}} = \frac{\sigma_{\text{coh}}}{4\pi}\frac{k_f}{k_i}NS(\mathbf{Q}, \omega) \tag{4.12}$$

$$\left(\frac{d^2\sigma}{d\Omega dE}\right)_{\text{inc}} = \frac{\sigma_{\text{inc}}}{4\pi}\frac{k_f}{k_i}NS(\mathbf{Q}, \omega) \tag{4.13}$$

These expressions can be related to Eq. 4.1 with the Van Hove transformation which recognizes that the scattering cross section can be expressed as a pair distribution function in space and time using the atomic density operator:

$$\rho_Q(t) = \sum_l e^{i\mathbf{Q}\cdot\mathbf{r}_l(t)} \tag{4.14}$$

Thus the expression Eq. 4.1 can be written in terms of the fourier transform of the time dependent pair-correlation function, using the density operator:

$$S(\mathbf{Q}, \omega) = \frac{1}{2\pi\hbar N}\int_{\infty}^{\infty} dt e^{-i\omega t}\langle\rho_{\mathbf{Q}}(0)\rho_{-\mathbf{Q}}(t)\rangle \tag{4.15}$$

The use of the density operator here gives a better physical intuition of the scattering law when reducing to the various scattering interactions[2]. As the neutron interacts with several properties of the scattering system (*e.g.* the nuclear lattice, magnetic electron density, or nuclear spin) there are distinct cross sections for the different measurements. The cross sections applicable to the work discussed in this dissertation are presented in the following sections with the applicable techniques.

[2] In the humble opinion of the author.

4.3 Elastic Neutron Scattering

Diffraction is a very powerful tool used in materials research, as it allows one to directly probe the atomic arrangement inside of a sample, and answer questions about fundamental symmetries in a direct way. Powder diffraction in particular is useful in these research avenues, as one can obtain meaningful data with a small laboratory x-ray source, while more advanced options for data collection are to be found at synchrotron or neutron sources. In powder diffraction, a sample of a material is prepared by making a powder of very fine crystallites, and encapsulating the powder in a container that (ideally) provides little coherent background to the scattering. The powder process collapses the three dimensional structural data down to the one dimension, but this is frequently sufficient to at least begin describing the structure, particularly with advanced analytical techniques like Rietveld refinement.

Diffraction is elastic scattering, arising from the coherent interference of the radiation with the particles in the sample. The energy of the incoming particles is sufficiently low that the sample is not disturbed, and recoil effects are typically neglected, and the magnitude of the elastic scattering momentum transfer reduces to:

$$|\mathbf{Q}| = \frac{4\pi \sin\theta}{\lambda} \tag{4.16}$$

Where λ is the incident wavelength of the radiation and θ is the half angle of scattering. This limitation on the elastic scattering will be important when discussing local atomic distortions.

The starting point for powder diffraction is Bragg's Law:

$$\lambda = 2\ d\ sin\theta \tag{4.17}$$

where d is the distance between crystalline lattice planes, λ again is the wavelength of the incident radiation, and θ is the angle describing the wave vector and the lattice plane normal. The information in diffraction is obtained on the basis of the wave

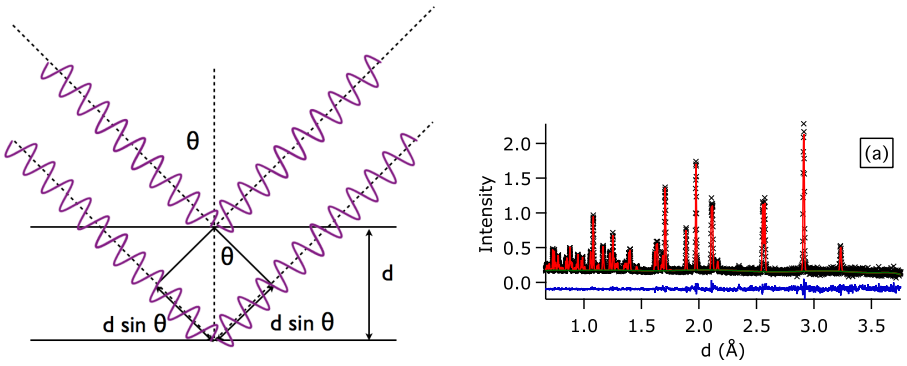

Figure 4.4: (left) Illustration of Bragg's law, where the total path length difference of radiation in a material gives rise to a coherent scattering condition. (right) Canonical diffraction pattern of a body centered tetragonal material.

diffraction theory, and it is the constructive interference of tens of thousand of lattice planes contributing to the diffraction that gives rise to the strong signals provided from single crystals and crystallite powders. With this in mind, it is very important to consider the size of the crystallites in the prepared powder sample. Ideally, crystalline powders should be prepared with a grit on the order of 10's of microns. If the powders are finer than this, the crystallography rules begin to break down[3] and consequently the scattering breaks down, and if the crystallites are too large, the approximation of full reduction to 1 scattering dimension breaks down, and finite size effects may obscure the data. Powder diffractometers have varied designs. The work presented in this dissertation has been conducted with time-of-flight (TOF) powder diffractometers like the POWGEN or NOMAD instruments at the SNS, which operate with an energy-dispersive mechanism. At these instruments, an incident beam of neutrons produced as in the manner outlined in section 4.6 is shaped upon exit from the monochromator to provide a pulse with a given central wavelength, and the beam pulse is tuned with the use of choppers. Using the deBroglie wavelength rewritten to be dependent on time of flight of the neutron (t_{of} stands for TOF, and L for the flight path of the neutron), and the Bragg scattering law from Eq. 4.17 on may make the substitutions:

[3] this is also why diffraction using nanoparticles is particularly tricky

$$\lambda = \frac{h}{mv} = \frac{ht_{\text{of}}}{mL} \rightarrow \text{Time-of-flight} \tag{4.18}$$

$$\lambda = 2d\sin\theta \rightarrow \text{Bragg's Law} \tag{4.19}$$

$$\tag{4.20}$$

to write

$$d = \frac{t}{252.7 \cdot L \cdot 2\sin\theta}\ [\text{Å}] \tag{4.21}$$

making the measured d-spacing proportional to the TOF, allowing one to measure many d-spacings at some fixed angle θ. The resolution of a powder diffractometer is a function of the moderator, moderator to sample distance, and sample to detector distance.

Table 4.3: Specifics of diffractometers used in research presented here.

	POWGEN	NOMAD	NPDF	HIPD
Moderator	Decoupled poisoned supercritical hydrogen	Decoupled poisoned super-critical hydrogen	Water (283K)	Water (283K)
Incident flight path	60 m	19.5 m	32m	9m
Final flight path	2.5-4.5 m	0.5-3m	1.5 m	??

Table 4.4: NIST certified powder diffraction standards with material type and application.

SRM	Material	Application
640c	Silicon Powder	Line Position, Line Profile
675	Mica Powder	Line Position, Low 2θ
660a	LaB_6 Powder	Line Position, Line Profile
1979	CeO_2, ZnO Powders	Line Position, Line Profile

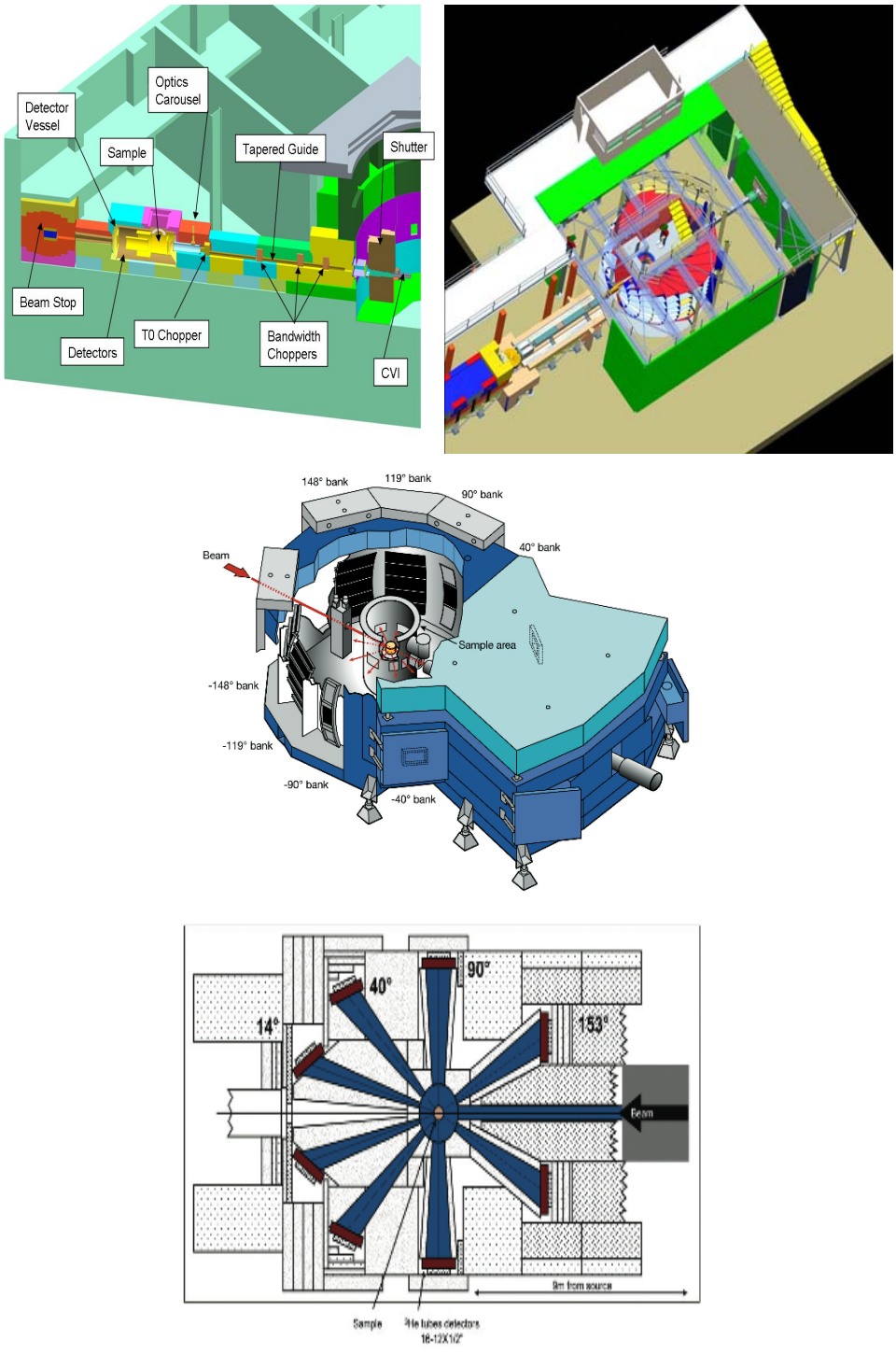

Figure 4.5: Clockwise from upper left, schematic drawings of NOMAD, POWGEN, HIPD, and NPDF.

Microscopically, a neutron powder diffraction measurement measures the coherent scattering cross section of the static system (*i.e.* the time average of the structure). From Eq. 4.15, we consider the time average of the system:

$$S(\mathbf{Q},\omega) = \delta(\hbar\omega)\frac{1}{N}\left\langle \sum_{ll'} e^{i\mathbf{Q}\cdot(\mathbf{r_l}-\mathbf{r_{l'}})} \right\rangle \tag{4.22}$$

where l, l' are different atoms in the sample.

For the idealized Bravais lattice, the only contributions to the static scattering come from points where the diffraction condition is met, *i.e.*, where $\mathbf{Q}$ is equal to a reciprocal lattice vector τ. For a real crystal, the static nuclear structure factor contains information about the atomic positions ($\mathbf{d_j}$) and mean squared displacements of the atoms from their equilibrium positions:

$$F_N(\tau) = \sum_j \bar{b}_j e^{i\tau\cdot\mathbf{d_j}} e^{-W_j} \tag{4.23}$$

And then the problem of crystallography really starts at turning the information from the scattering pattern into a structural model. A number of methods exist to exploit the rules of crystallography to determine the spatial structure from powder diffraction information. Here we will focus on Rietveld refinements for average structural data, and analysis of pair distribution functions for short range structural information. Both methods allow the refinement of structural models against experimental data, and can be applied to both x-ray and neutron data. Both x-ray and neutron data sets can be used in tandem to reduce uncertainty in experimental parameters, and to provide constraints to the refinements.

4.3.1 Rietveld Refinement

The method of Rietveld refinement(195) allows one to fit a structural model to an observed data pattern using a method of least squares refinement. The fundamental concept is to generate a powder diffraction pattern from a model, compare this with the observed pattern, refine the model in a least squares fitting procedure, and then iterate

these steps to find a better model. Using the Rietveld method the experimenter can refine a number of sample properties, as well as understand the thermal motion of the sample, the presence of impurity phases, and site occupancies, as well as the influence of the instrument on the measurement.

The calculated intensity for a diffraction pattern for use in Rietveld Refinments:

$$I_{\mathrm{calc}} = I_{\mathrm{back}} + S \sum_{\mathrm{hkl}} C_{\mathrm{hkl}}(Q) f^2_{\mathrm{hkl}}(Q) P_{\mathrm{hkl}}(Q) \tag{4.24}$$

Where I_{back} is the background intensity, typically estimated by a polynomial or some form of power series expansion in $\mathbf{Q}$. S is a scale factor, the symmetry information is contained in $\sum_{\mathrm{hkl}}$, the structure factor $f^2_{\mathrm{hkl}}(Q)$ contains information about the positions, site occupancy, and thermal motions, and the profile term $P_{\mathrm{hkl}}(Q)$ contains instrument terms that result in information about the particle size, texture, and instrumental resolution. $C_{\mathrm{hkl}}(Q)$ is a correction term to the instrument setup. Note that unit cell information is uncorrelated to atomic position information, with the lattice parameter information appearing in the $\sum_{\mathrm{hkl}}$ term and the atomic positions in the $f^2_{\mathrm{hkl}}(Q)$ term. Considering this, one understands the need for improved statistics to obtain full structural characterization information, where as for a lattice parameter measurement, the structural coherence of the sample will lead to an answer about the lattice parameter and the symmetry very quickly.

The Rietveld refinement method revolutionized crystallography. By reducing complicated structural analysis to an algorithm, which could be computerized, the method made available a robust algorithm to determine crystal structure, and the use of the method resulted in an over ten fold increase in publication of crystal structure data.

Structural models produced by Rietveld analysis are judged by the metrics of *R-factor*, χ^2, and physical reasonability, two of which are developed directly from Rietveld codes. The R-factor, or residuals function, is the difference between the model and the experiment:

$$R = \frac{\int [I_{\mathrm{m}}(Q) - I_{\mathrm{c}}(Q)]^2 dQ}{\int [I_{\mathrm{m}}(Q)]^2 dQ} \tag{4.25}$$

And ideally a value less than 10% will indicate a good fit to the model. The value of χ^2 is defined as the *reduced goodness of fit*:

$$\chi^2 = \frac{f_k \sum M_k}{(N_{\mathrm{obs}} - N_{\mathrm{var}})} \tag{4.26}$$

where N_{obs} is the total number of observations, and N_{var} is the number of variables being refined in the model, and f_k, M_k refer to the model residuals(196). While smaller R and χ^2 values possess certain psychological benefit, the reasonability of the physical model must be considered before any final declaration of victory is made. These determinations are improved with experience, but one must consider at the zeroth order the values of the interatomic bond lengths, the values of the isotropic thermal factors, and the fit of the model to the data.

For proper refinement of powder diffraction data, one must perform a calibration of the diffractometer. This is done using a line shape standard (Tab. 4.4). Standards are available commercially from the National Institute of Standards and Technology(197).

4.3.2 Pair Distribution Function

The total scattering function $S(\mathbf{Q})$ is the intensity of the scattering in $\mathbf{Q}$ space, and the PDF is determined by the Fourier transform of the total scattering function(198).

$$g(r) = \frac{2}{\pi} \int_0^{Q_{max}} Q[S(Q) - 1] \sin(Qr) dQ \tag{4.27}$$

This fourier transform takes us back to real space, showing that what the PDF physically represents is a real space map of the atomic positions within a solid; a probability distribution function providing the $probability$ of finding two atoms a distance r apart within a material (fig. 4.6). This has two important consequences. The first is that the transformation to r allows a direct analysis of real space, rather

than reciprocal space. Further, the PDF retains *all information* collected by the powder diffraction experiment, including diffuse scattering and inelastic scattering(198). This notion is what sets the PDF method apart from other powder refinement methods, where diffuse scattering is typically discarded as background and only the contributions from the Bragg peaks are included(195). The value of $Q_{\max}$ in the upper limit of the integral in eq. 4.27 needs to be as large as possible to prevent termination ripples from appearing in the final PDF. This constraint manifests in the construction of instruments capable of performing a PDF measurement, and the current practical limit is a momentum transfer of 60 Å^{-1}. Further, the value of the total scattering function $S(Q)$ tends to 1 as $Q \to \infty$, so the version of the $S(Q)$ to be transformed has a 1 subtracted from it to subtract contributions from the average continuum, since there is no diffraction in the infinite limit(198).

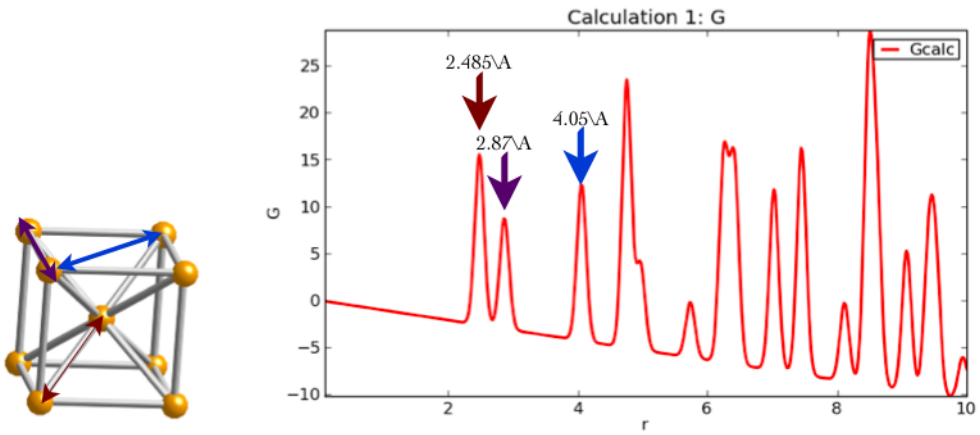

Figure 4.6: Unit cell for body-centered-cubic iron, and the calculated corresponding PDF. Colored arrows indicate atomic distances that map into the PDF.

The real strength of PDF analysis lies in the ability to create a structural model that allows analysis of real space without any *a priori* assumptions about the crystal structure. PDF analysis is the most useful in situations where there is known or suspected disorder in materials, which can be indicated by anomalous powder diffraction patterns or larger than predicted DeBye-Waller factors in Rietveld analysis(199; 200). The PDF is able to detect local distortions, and can determine the point of crossover from local to long range

order(198; 201). In a high-r limit, the results of the PDF refinement should agree with the Rietveld refinement for crystalline data, as the effects of local distortion are minimized at longer length scales(198).

The notion of fourier transformation of the powder diffraction pattern was first demonstrated by Warren in the 1930's (202) with x-rays. With x-rays is the atomic structure factor drops off very rapidly in Q, which limits the resolution of the measurement. Further, computation of Fourier transforms was arduous making the calculations difficult and the rising popularity of the Rietveld Method(195) in the late 1960's(203) made it possible to very rapidly analyze crystal structures in reciprocal space. The PDF method was largely a tool of the liquids and glasses community until it was revived as a crystalline modeling tool in the late 1980's. At this juncture, with the rise in pulsed neutron sources capable of reaching high enough energies and emergence of faster computing methods made crystalline analysis with the PDF feasible(199).

Atomic displacements due to lattice effects (primarily phonons) are described by the DeBye-Waller factor, which can be expressed in a way to highlight its connection to the mean amplitude of the thermal vibrational amplitude:

$$e^{-Q^2\langle\langle u^2\rangle\rangle} = e^{-2Bs^2}, \quad B = 8\pi^2\langle\langle u^2\rangle\rangle \tag{4.28}$$

Where use of the elastic scattering expression for **Q** from Eq. 4.16, and s is $sin\theta/\lambda$. The value of the DeBye-Waller factor is usually less than 0.1 Å for most atoms in a compound, and common elemental values may be found in the literature, approximated using the DeBye model, or directly calculated if the phonon density of states is known.

Generally, disorder in a system may be suggested by DeBye-Waller factors greater than 0.1 Å, although this oversimplifies the situation. Cases where there are correlated atomic displacements will impact the value of the DeBye-Waller factor estimated from a Rietveld type analysis. If atomic motions are correlated, their relative displacement will be overestimated, while for anticorrelated motions, the relative displacement will be underestimated. The displacement of atoms detectable by crystallographic methods goes

as 1/**Q**, so for example a real space displacement of ϵ = 0.1 Å will appear to modify the diffraction intensity near 31.4 $Å^{-1}$, which cannot be detected by long range refinements such as Rietveld, as even if these points are collected in the pattern, the scattering intensity at high **Q** is typically discarded as indistinct from background due to high peak overlap and the reduction in intensity caused by the DeBye-Waller effect.

The reduced pair distribution function $G(r)$ is defined:

$$G(r) = 4\pi r[g(r) - 1] = \frac{2}{\pi}\int_0^{Q_{\max}} Q[S(Q) - 1]\sin(Qr)dQ \tag{4.29}$$

The *pair density function* is defined as:

$$\rho(r) = \rho_0 g(r)$$

so that the value tends to the average density at large r.

Magnetic PDF

Magnetic structure determinations using neutrons is possible, but the PDF of magnetic structures is typically dominated by the nuclear scattering. For example, in Ni, the mean radius of the electron cloud is approximately 0.5 Å, meaning that the full width of the magnetic peak would be 1.4 Å, which will substantially broader than the nuclear peak. Further, since the scattering length is less for magnetic than nuclear scattering, the intensity of the magnetic peak is diminished substantially, making the magnetic scattering a broad background to the PDF. Generally, spin-polarized neutron scattering[4] is required to separate the magnetic component.

Sources of error

The biggest error in PDF analysis arises as termination errors - direct artifacts of the Fourier transform process which appear as spurious peaks in the data. If the value

[4]See section 4.5.

of $Q_{\max}$ is greater than or equal to $3/\langle\langle u^2\rangle\rangle^{1/2}$, then the effect of termination ripples may be minimized(204; 205). Other sources of error include the **Q** resolution of the diffractometer, and the asymmetry of the scattering due to the asymmetric nature of a TOF diffractometer. Both of these present difficulties to Rietveld refinement, and are best handled with careful calibration of the diffraction instruments.

4.4 Inelastic Neutron Scattering

In inelastic scattering, the loss or gain of energy to the scattering system by the probe particle is the quantity of interest. The conservation of energy and momentum dictate:

$$\mathbf{Q} = \tau + \mathbf{q} = \mathbf{k_i} - \mathbf{k_f}$$
$$\hbar\omega = E_i - E_f$$

Where τ is a reciprocal lattice vector, $\mathbf{q}$ is the inelastic momentum transfer, and $\hbar\omega$ is the energy transfer to (from) the sample. The energies $\hbar\omega$ correspond to dynamic features like phonons and magnons, while the momentum discrimination allows the experimenter to probe dispersions.

The scattering cross section for inelastic scattering can be transformed into the scattering function, which in turn is directly related to the imaginary part of the dynamic susceptibility:

$$S(\mathbf{Q},\omega) = \frac{\chi''(\mathbf{Q},\omega)}{1 - exp(\hbar\omega\beta)} \tag{4.30}$$

Where the Bose-Einstein distribution function describes the detailed balance, or relative probability of transition of the neutron to different energy states, based on the thermodynamic fact that the probability of a system being in a high energy state is lower by a factor $e^{-\hbar\omega\beta}$.

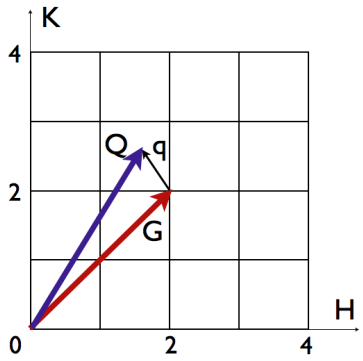

Figure 4.7: Schematic of reciprocal space for probing a transverse lattice excitation near H = K = 2.

4.4.1 Time of flight neutron scattering

Two classes of instruments used for inelastic neutron measurements are time-of-flight (TOF) spectrometers and triple-axis spectromter (TAS). The TOF technique exploits the knowledge of neutron time of flight to perform energy discrimination. Knowing precisely the distance from the source to the sample, and then the sample to the detector distance, one can use the arrival time information of the neutrons to understand the energy loss or gain of the incident neutrons. The TOF technique is applied two ways, through *direct geometry* where the incident neutron beam is of a well defined energy and the scattered beam is of varying final energies; and *indirect geometry* where the incident beam is white (contains many wavelengths) or quasi-white, and the beam scattered from the sample is backscattered into a detector array by use of high-quality crystals that reflect one wavelength. The distinction between the technique is the energy resolution obtained with the backscattered beam from the indirect geometry machine is much higher due to the imposed reflection conditions and the perfection of the crystal analyzers[5].

The time of flight of a neutron at thermal and cold energies is very straightforward to calculate, and in units convenient to neutron scattering can be found from the following expression:

[5]The work presented here makes no use of indirect geometry machines, but the technique is presented for completeness.

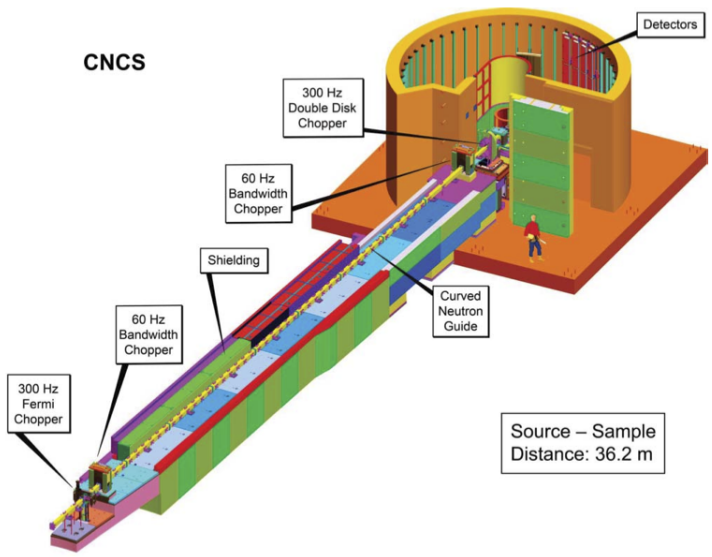

Figure 4.8: The CNCS instrument at the SNS.

$$T_{\mathrm{of}}[\mu\mathrm{s}] = \frac{2286.3\ \mathrm{L[m]}}{\mathrm{E_i[meV]}} \tag{4.31}$$

Time of flight inelastic instruments are well-suited to spallation sources due to the time structure imposed on the source by the pulsed operation of the accelerator. Several time of flight instruments used for the work presented here are in operation at the SNS. The Wide Angular Range Chopper Spectrometer (ARCS)(206) and Cold Neutron Chopper Spectrometer (CNCS)(207) were all used at the SNS to perform studies. These beam lines consist of a stretch of neutron guide on the order of 10 meters and use several choppers for incident energy discrimination. The CNCS instrument is shown in Fig. 4.8, and shows the relative layout of the beamline components. The ARCS instrument is on an ambient moderator and has a relatively short initial (13.6 m) and final (3.0 m) flight path, with wide angular coverage making it ideally suited for high Q measurements required for lattice dynamical studies(206). The CNCS instrument is a flexible resolution spectrometer optimized for the study of low-energy excitations, located on a coupled liquid hydrogen moderator with the initial moderator to sample distance of 36.2 m, and final flight path of 3.5 m(207).

Time of flight instruments are also used at continuous reactor sources, where a time structure can be imposed on the beam by careful use of choppers. The time structure can be imposed using as few as two choppers. In the case of the TOF instrument at the reactor source, the final intensity on sample is orders of magnitude lower than that available at a TAS due to the amount of beam lost in the chopping process to impose the time structure.

The strong advantage of the TOF instrument is to gain access to a large region of $(\mathbf{Q}, \omega)$ space at once. With the large area of pixelated detectors, the instrument has many thousands of individual detectors. Effectively, this allows the experimenter to study a large swath of momentum and energy space, and in the case of crystals, the ability to map the dispersion relation of dynamical features in a single experiment. The disadvantage is the loss of flux incurred by performing the chopping of the neutron beam.

The accessible regions of $(\mathbf{Q}, \omega)$ space for a TOF measurement are dictated by the energy and momentum conservation rules:

$$\frac{\hbar^2|\mathbf{Q}|^2}{2m} = 2E_i - \hbar\omega - 2\cos(2\theta_S)\sqrt{E_i(E_i - \hbar\omega)} \tag{4.32}$$

Where E_i is the incident energy of the neutron beam, $\hbar\omega$ is the magnitude of the energy transfer to the neutron, and θ_S is the scattering angle. At the point where the energy-momentum parabola intersects $S(\mathbf{Q}, \omega)$ is a point where a measurement can be made.

The resolution of a time of flight spectrometer is broken up into two parts, the energy and momentum resolution. The energy resolution is a function of E_i, E_f, L_{mc} - distance from the moderator to the Fermi chopper, L_{sd} - distance from the sample to the detector, L_{cs} - distance from the Fermi chopper to the sample, δt_m - time width of moderated pulse, δt_c - time width of pulse after Fermi chopper:

$$\frac{\Delta E}{E} = \frac{2\delta t_m}{L_{mc}}\left[\left(1 + \left(\frac{E_f}{E_i}\right)^{3/2}\frac{L_{cs}}{L_{sd}}\right)^2 + \left(\frac{\delta t_r}{\delta t_m}\right)^2\left(1 + \left(\frac{E_f}{E_i}\right)^{3/2}\frac{L_{mc}}{L_{sd}}\left(1 + \frac{L_{cs}}{L_{mc}}\right)\right)^2\right] \tag{4.33}$$

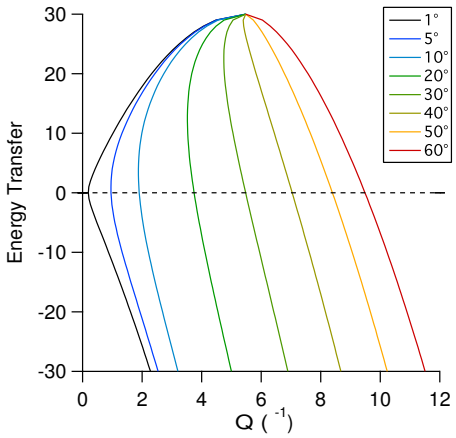

Figure 4.9: Q, E space diagram for the case E_i= 30 meV. Different trajectories show the space accessible to certain values of θ as a scattering angle.

Where all of the time distributions are approximated as Gaussians.

In the TOF experiment, the detector coverage acquires a full four-dimensional data set. To functionally analyze the data, a reduced subset of the full dataset (known as a cut or slice) is created by collapsing the dataset along one of the four dimensions.

4.4.2 Triple Axis Spectroscopy

A triple-axis spectromter (TAS) makes use of three rotational axes to define a particular point in reciprocal space to investigate inelastic events in a material (figure 4.10a). The first rotational axis is the rotation of an incident beam monochromator, which selects the initial neutron energy and wave vector. The second is the sample rotation, which specifies the point of interest in reciprocal space. The third is the rotation of the analyzer crystal to select the final wave vector. The monochromator and analyzer crystal use Bragg reflection in the wave vector selection. The analyzed beam is then sent to a detector array of small ^{3}He tubes. A beam monitor is typically placed in the beam before the sample position to count the incident neutron beam for proper normalization of the spectra. The advantage of the TAS machine is that the flux is several orders of magnitude greater than that at a TOF instrument. Therefore, if a point of interest is very well defined in reciprocal space, the TAS instrument is the instrument of choice.

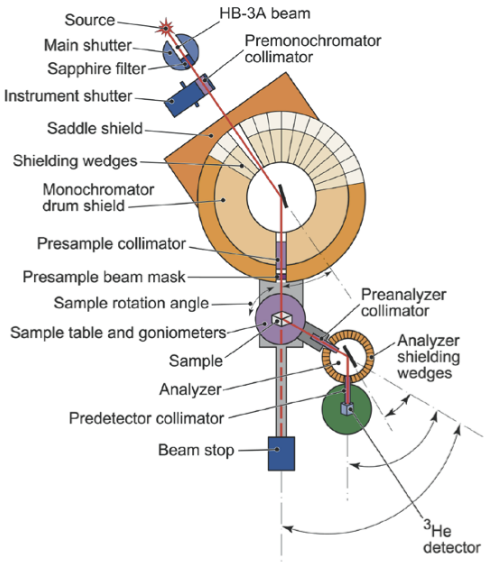

(a) HB-3 instrument at the HFIR at ORNL. HB-3 is a triple-axis spectrometer setup, with a thermal neutron beam, sapphire fast-filter, adjustable analyzer setup, and choice of incident beam monochromators.

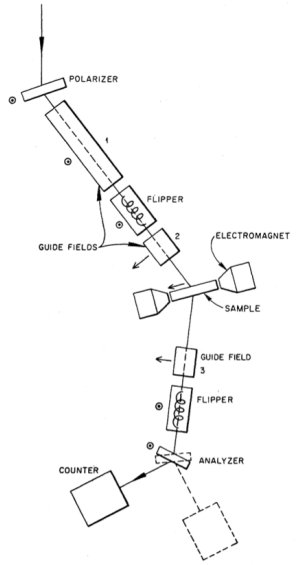

(b) Triple axis polarization setup as described in text. Graphic from (208).

Figure 4.10: Triple axis setups.

Table 4.5: Properties of crystals used for beam selection or filtering purposes on a neutron scattering instrument. Information obtained from (1)

Type	d-spacing	Notes
PG(002)	3.35Å	Good reflectivity, filters λ/n
Si(111)	3.135Å	Eliminates λ/n
Be(002)	1.79Å	Better resolution at high energy transfers
Heusler	3.437Å	Used for polarization

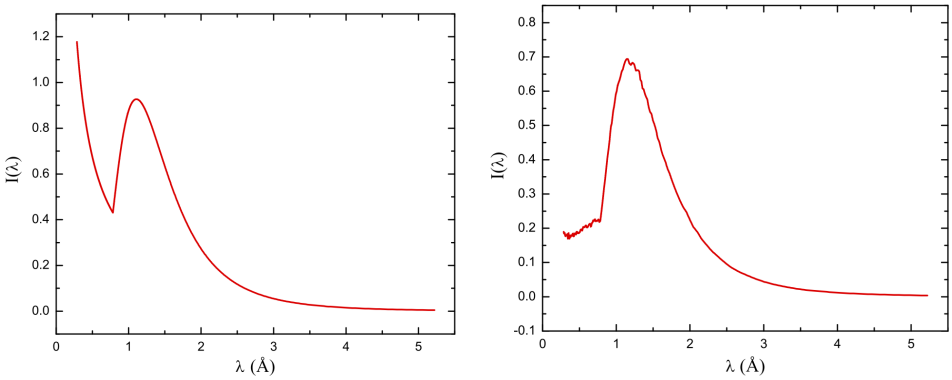

Figure 4.11: (top) Moderated neutron flux spectrum at HB3 including under moderated epithermal tail. (bottom) Reactor spectrum after sapphire fast neutron filter. Figures from (17)

The scattering intensity measured by the TAS is a convolution of the resolution function $R(\mathbf{Q}-\mathbf{Q_0}, \omega-\omega_0)$ with the dynamic scattering function $S(\mathbf{Q},\omega)$, representing a 4 dimensional ellipsoid in ($\mathbf{Q}$,ω) space:

$$I(\mathbf{Q_0},\omega_0) \propto \int\int R(\mathbf{Q}-\mathbf{Q_0},\omega-\omega_0)S(\mathbf{Q},\omega)\, d\mathbf{Q}\, d\omega \tag{4.34}$$

The mathematical formalism for the resolution function is fully explored in Ref. (209) and presented well in Ref. (1). In the TAS setup, the variation in the E_i or E_f is left to the experimenter, though in practice, it is most straightforward to fix the value of E_f and allow E_i to vary. The purpose for this is due to dependence of the resolution function of the TAS on E_f. If an experiment measures using a fixed E_i and variable E_f, a correction to the resolution function must be made at every point of the measurement, whereas if E_i is varied and E_f is fixed, there is only one correction to the resolution function.

An issue with the TAS beam flux is that the Bragg condition for scattering of some arbitrary wavelength λ is also satisfied for wavelengths λ/n, where n is some integer value, [6] which can lead to spurious artifacts in the data. Higher order contamination can be reduced in part by use of a sapphire filter, which preferentially transmits lower energy neutrons and scatters high energy neutrons through thermal interactions (phonons)(Fig. 4.11), and PG filters are used to scatter the incident beam to remove this higher order contamination.

4.5 Magnetic and Polarized Neutron Scattering

This section will discuss magnetic neutron scattering as relevant for the work presented in this thesis. There are several comprehensive sources on this subject which are cited during this passage which can be referred to for more information(177; 181; 210; 211; 1; 212).

With a small but measurable and easily manipulated magnetic dipole moment, neutron scattering is a preferred technique for studying the magnetic behavior of solids. The neutron interacts directly with unpaired electrons in materials giving rise to magnetic scattering, and the spin and magnetic moment of the neutron can be manipulated for polarization analysis. These factors can be used together to understand the degree of magnetic ordering in a system, distinguishing paramagnetic from ordered states, and providing insight on the degree of magnetic frustration in a system.

Magnetic neutron scattering provides information about the spin-spin correlation function, knowledge of which allows the distinction between states of magnetism with different symmetries and correlation lengths, and can be extended to characterize other magnetic excitation like spin waves. The two-spin correlation function describes the interaction between magnetic sites separated by a distance $\mathbf{R}$, with the dynamic scattering law describing the space and time correlation:

[6] The contamination is typically blunted for orders of $n > 3$ due to the flux spectrum of the reactor.

$$S^{\alpha\beta}(\mathbf{q},\omega) = \frac{1}{2\pi}\sum_{\mathbf{R}}\int_{-\infty}^{+\infty} e^{i\mathbf{q}\cdot\mathbf{R}-\omega t}\langle S_0^{\alpha}(0)S_{\mathbf{R}}^{\beta}(t)\rangle\, dt \tag{4.35}$$

where α and β are the spin states at the different atomic sites.

In magnetic neutron scattering, the neutrons interact with the magnetic field generated by unpaired electrons in the sample. This field may have a time varying component as in the case of spin waves, or be constant, in the case of magnetically ordered solids. The amplitude of the scattering is a function of the magnetic form factor of the material and the spin amplitude:

$$\text{amp} = \mathbf{S}\left(\frac{\gamma r_0}{2}\right) g f(\mathbf{Q}) \tag{4.36}$$

Where r_0 is the classical electron radius, and $f(\mathbf{Q})$ is the Fourier transform of the spin density at the atomic site(1):

$$f(\mathbf{Q}) = \int \rho_s(\mathbf{r}) e^{i\mathbf{Q}\cdot\mathbf{r}}\, d\mathbf{r} \tag{4.37}$$

The neutron samples the time fourier transfer of the magnetic field, and interference patterns are generated from the difference in scattering from the different sites. Also, electrons are not at fixed locations in solids, but have some spatial extent in orbitals so there is in principle a spatial variation as well. Further, because of the limitation against magnetic monopoles, there is no neutron scattering interaction for spin density which is parallel to the scattering vector of the experiment. This further modifies the measured scattering function by requiring that only values perpendicular to the scattering vector be tabulated in the final result.

According to the Wigner-Eckert theorem, the spin density on a given atom can be represented as a localized spin operator, rather than the spatially extended field. This

reduction introduces a correction into the scattering scattering function dependent on the square of the magnetic form factor[7] $f(\mathbf{Q})$.

$$\left(\frac{d^2\sigma}{d\Omega dE}\right) = r_o^2 \frac{k_f}{k_i} f(\mathbf{Q})^2 \sum_{\alpha\beta} (\delta_{\alpha\beta} - \hat{q}_\alpha \hat{q}_\beta) S^{\alpha\beta}(\mathbf{Q}, \omega) \tag{4.38}$$

In general the contribution of the magnetic scattering from electrons becomes small with increasing values of $\mathbf{Q}$.

Representing Eq. 4.38 in terms of the Fermi rule formalism, the inclusion of magnetic scattering induces a modification of Equation 4.4 to include spin-state transitions of the atomic electrons:

$$\left(\frac{d^2\sigma}{d\Omega dE}\right)_{\lambda' \to \lambda} = \frac{k'}{k} \sum_{\lambda_i, \lambda_f} P(\lambda_i) \left| \langle \lambda_f | b \sum_l e^{(i\mathbf{Q}\cdot\mathbf{r}_l)} U_l^{s_i s_f} | \lambda_i \rangle \right|^2 \delta(\hbar\omega + E_i - E_f) \tag{4.39}$$

where $U_l^{s_i s_f}$ is the scattering amplitude between spin states at atomic site l(1). More explicitly:

$$U_l^{s_i s_f} = \langle s_f | b_l - p_l \mathbf{S}_{\perp l} \cdot \sigma + B_l \mathbf{I}_l \cdot \sigma | s_i \rangle \tag{4.40}$$

where b is the nuclear coherent scattering length at atomic site l, B and $\mathbf{I}$ are the nuclear spin-dependent and nuclear spin operators, respectively. $\mathbf{S}$ is the atomic spin operator, and $\mathbf{S}_\perp$ is the magnetic interaction vector, derived:

$$\mathbf{S}_\perp = \hat{\mathbf{Q}} \times (\mathbf{S} \times \hat{\mathbf{Q}}) \tag{4.41}$$

which, when taken together with Equation 4.40, indicates that only the component of the atomic spin perpendicular to the momentum transfer will have any scattering amplitude (illustrated in figure 4.12, $\hat{\mathbf{Q}}$ is a unit vector along $\mathbf{Q}$) (208; 1).

[7] Magnetic form factors for the solid state are complex to calculate, and arise from integration of the radial distribution of electrons in an orbital. This involves integration of spherical Bessel functions, and is generally accepted practice to look up the values in a table(213).

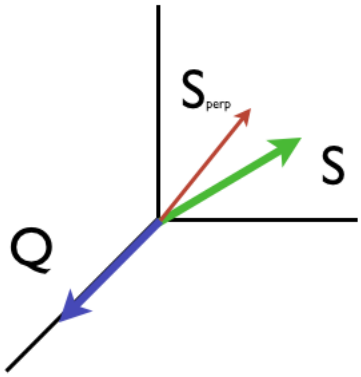

Figure 4.12: Demonstration of the perpendicular component of the spin state which can be detected with polarized neutron scattering. Only the component of $\vec{S}$ perpendicular to the momentum transfer $\vec{Q}$ will be included in the scattering cross section measurement as indicated by equations 4.40, 4.41 .

If the neutron polarization is measured before and after the scattering, one can generate four cross sections for the scattering processes, named *spin-state* cross sections, which take the change in polarization of the neutron into account. Taking (ξ, η, ζ) as the polarization coordinates and ζ as the initial direction of polarization:

$$\begin{aligned} U^{++} &= b - pS_{\perp\zeta} + BI_{\zeta} \\ U^{--} &= b + pS_{\perp\zeta} - BI_{\zeta} \\ U^{+-} &= -p(S_{\perp\xi} + iS_{\perp\eta}) + B(I_{\xi} + iI_{\eta}) \\ U^{-+} &= -p(S_{\perp\xi} - iS_{\perp\eta}) + B(I_{\xi} - iI_{\eta}) \end{aligned} \tag{4.42}$$

Where the superscripts indicate the initial and final spin states. Where the initial and final states are the same (ie, U^{++}, U^{--}), these terms are non-spin-flip (NSF) meaning there is no change in the neutron spin polarization upon interaction with the sample, while the condition where the initial and final states are different (ie, U^{-+}, U^{+-}) are called spin-flip (SF), and arise when the spin of the neutron is impacted by interaction with the sample.

The four cross section terms allow detection of SF or NSF phenomena in the different configurations. For example, coherent nuclear scattering is always NSF, as there is no nuclear component in the cross sections for U^{-+}, U^{+-} in Equation 4.42. Nuclear spin incoherent scattering is both SF and NSF, albeit with different intensities. Paramagnetic systems are particularly well elucidated by the mechanisms of spin polarized scattering, as regions of local spin density can be determined, in addition distinguishing other nuclear coherent components(208).

The many conditions of spin versus non spin flip can be succinctly summarized by Moon et. al(208) as the following points:

- If neutron polarization $\mathbf{P_0}$ is along the scattering vector $\mathbf{Q}$, then all magnetic scattering is spin flip scattering
- Components of $\mathbf{S}_\perp$ that are perpendicular to the neutron polarization will produce spin-flip scattering
- Components of $\mathbf{S}_\perp$ that are parallel to the neutron polarization will produce non-spin-flip scattering.

Using these properties in connection with polarization control, one can distinguish the contributions between SF and NSF properties, and then relate the observations back to system properties. This formalism shows that polarization analysis is a very powerful tool for separating out magnetic and nuclear scattering in a system.

Beamlines with polarization analysis capabilities currently employ one of two methods to polarize the beam. One way is the use of supermirrors that only have a scattering cross section for neutrons polarized in a specific direction. The other method is to use ^{3}He gas polarized by an optical pumping technique where rubidium atoms are polarized, and then transfer their polarization to the helium atoms by means of collisions inside of a pressurized gas cell. The first of these is robust, but very expensive to produce, while the ^{3}He cells require a significant outlay of infrastructure, and rely on the increasingly scarce commodity of ^{3}He.

A triple axis spectrometer is perhaps the most common setup for conducting inelastic polarized neutron studies on materials, and a basic setup is shown in figure 4.10b. The first component of a polarized neutron setup is the polarization of the neutrons, commonly performed on a triple axis setup with a magnetized monochromator. The ideal monochromator is created out of an alloy which has a nuclear scattering amplitude equal to that of the magnetic scattering amplitude, resulting in a diffracted beam that is fully spin polarized. The material closest to this ideal setup is known as Heusler Alloy (Cu_2MnAl), which has its magnetization controlled with permanent magnets which also define the direction of neutron polarization(212). Heusler alloy has d-spacing of 3.44 Å for the (111) reflection, which makes it very good for intensity transmission in balance with the needs of polarized beams(1).

Alternatively, one can exploit the use of ^{3}He spin filters to polarize the beam. These filters work on the principle that polarized ^{3}He has a very high absorption cross section for neutrons that are polarized anti-parallel to the helium atoms, and almost no absorption cross section for neutrons that are polarized parallel to the ^{3}He. The polarized ^{3}He gas cells are created via spin exchange optical pumping with a polarized rubidum-potassium gas mixture(214). These spin filters are used to polarize the incident beam, and analyze the scattered beam, and unlike the permanent Heusler setup identified above, require replacement, and have a time dependence to their polarization effectiveness(215).

Once the beam is polarized, the polarization direction is maintained with a guide field, a very weak magnetic field between the polarizer and the sample position. The direction of the field dictates the terminology for the neutron polarization, typically with "up" defined as parallel to the guide field along the z-axis, with the counterpoint being "down". Before and after the sample are "flippers", radio frequency emitting devices that rotate the polarization vector of the neutron to the opposite direction.

The figure of merit for a polarized neutron set up is the flipping ratio, which is the ratio of nuclear Bragg peak intensities with the flipper off and then on, given by:

$$R = \left(\frac{F_N + F_M}{F_N - F_M} \right)^2 \tag{4.43}$$

The flipping ratio of a polarization setup is dependent on the incident neutron energy, higher order contaminants, the size of the beam, and collimation(1). With a Heusler crystal, one can typically obtain greater than 95% polarization, with a flipping ratio greater than 40. With a ^{3}He setup, flipping ratios are determined with the same procedure, but are time dependent. In addition to determining the quality of the polarized beam, this flipping ratio is also used for determination of magnetic scattering intensity without full polarization analysis(212).

A significant drawback to polarized neutron scattering research is the flux limitations of the technique. Neutron scattering is already a flux limited technique, with the brightest reactor sources only reaching the 10^8 neutrons/second range at the sample position, the polarization setup reduces the flux by a factor between 20 and 40, which can significantly increase times needed to conduct experiments to sufficient statistical confidence.

There are several sources of error in polarized neutron studies. The setup dependent problems can include poor flipper efficiency or incomplete polarization from the polarization source, and inhomogeneities in the magnetic guide fields that can cause the polarization of the neutron to change. Also, for ^{3}He setups, the polarization capabilities are time dependent, resulting in a loss of polarization effectiveness over time, which must be accounted for in a careful polarization analysis. Sample dependent issues like misoriented domains or fluxons in superconductors can decrease the polarization effectiveness by locally distorting the magnetic field in the sample.

4.6 Neutron Beam Production

It is worthwhile to discuss the elements of a neutron beam instrument, as they play a critical role in determining the properties of beam lines suitable for experimental studies. Production of neutrons in quantities useful for condensed matter physics research are

currently limited to reactor and spallation sources. At reactor sources, a self sustaining critical nuclear reaction produces excess neutrons as a byproduct of the chain reaction. These neutrons have energies in a range up to 2 MeV, but can be made useful for scattering research through the use of neutronic techniques to lower the energy of the neutrons, including reflection and moderation.

A spallation source produces neutrons by colliding a high energy beam of protons onto a target. At the SNS, this is done by producing a pulse of of H^- ions from a plasma ion source that has a 1 millisecond temporal extent, chopping that pulse into many pulses of the order of 1 μs, accelerating the beam of H^- ion pulses to high energy (of order 1 GeV), stripping the electrons away to create bare protons, stacking the 1μs pulses on top of one another, and then sending the 1μs pulse to a liquid mercury target. The high energy protons have de Broglie wavelengths that are sufficiently short to allow the proton to interact directly with the nuclei, triggering an internuclear cascade that results in the ejection of nucleons and a highly excited target nucleus. The excited nucleus then reduces its energy through evaporation of nucleons, and the daughter products of these reactions may have sufficient energy to continue the cascade to produce additional neutrons(216).

The intended scientific program of a neutron instrument is the driving factor in designing the beamline. Effectively, the most desirable characteristic is a neutron beam with a well defined temporal extent of suitable energies. These considerations include the energy and length scales of the intended objects of study, and time structure needed to perform the experiments. The neutrons produced by spallation reactions can have energies up to the incident proton beam energy, most often this is way above energies useful for the science, so the neutron beam energy must be reduced. Producing a useful neutron beam can be roughly broken down into a primary and secondary stage. The primary stage uses a series of moderators, reflectors, and couplers to drive as much of the neutron beam to useful energies as possible. The secondary stage uses other beamline elements like neutron guides or choppers to fine tune the energy spectra.

In the primary stage, the goal is to drive as much of the neutron beam into a moderator while maintaining a tolerable degradation of the time structure. After the

spallation reaction, neutrons are ejected from the target, and are ideally directed toward a moderator. A moderator typically contains a large quantity of light-mass material with an equilibrium temperature suitable for some desired energy range. The high energy neutrons enter the moderator face, and undergo a number of elastic collisions, shedding kinetic energy in the process. By the conservation of energy, a the change in velocity of a particle is given by the relation:

$$v_f = \frac{(m_1 - m_2)}{(m_1 + m_2)} v_i$$

where m_1, m_2 are the mass of the two particles involved in the collision, and v_i, v_f are the incident and final velocities. It can clearly be seen that the maximal change in velocity, and thus energy, is found when the masses are close, thus light elements or compounds like water, hydrogen, and methane are used as moderators. The moderated spectrum is approximately Maxwellian with an exponential tail of epithermal or undermoderated neutrons. The position of the moderator relative to the target can influence the neutron beam characteristics. For example, at the SNS, the moderators are set up in a “wing” geometry around the target, ensuring that every neutron that enters the moderator has undergone at least one collision to reduce its energy.

Coupling as a generic term describes the process of getting the neutrons to interact with the moderator, and specific mechanisms are described as being either geometric or neutronic couplers. Geometric couplers are design elements that “direct” neutrons into a moderator. The most common of these are reflectors. As the name suggests, the reflector returns neutrons to the moderator by “reflecting" them. Beryllium is commonly used, but more advanced sources use reflectors comprised of multiple distinct stages contributing to the reflection process(216). Neutronic coupling describes the specifics of the moderating system that result in successful moderation of the neutrons. The interaction between the moderator, coupling elements, and the neutron beam is complex, and each component impacts the time structure of the beam. In the case of decoupled systems, the temporal extent of the incident proton beam is much shorter than the

average thermalization time of the neutrons in the moderating system. This allows one to tailor the temporal extent of the pulse by using slow neutron absorbers in the form of poisons or liners. For coupled moderators, the neutrons communicate with their surroundings to a greater degree, and this has the net effect of increasing the available flux, at the expense of blurring the time structure(216)

Secondary tailoring of the neutron spectrum is achieved with choppers or monochromators. Monochromators are large single crystals or single crystal arrays of a compound that Bragg reflect neutrons of a certain wavelength. Every monochromator has an intrinsic width, known as the Darwin width, which sets the energy resolution. Some monochromators, like those made of Heusler alloy preferentially scatter neutrons of a specific spin state, assisting in the polarization of neutron beams. [8] A table of commonly used monochromators and relevant physical properties are show in Tab. 4.5.

Neutron choppers are disks of neutron absorbing material that spin at high rates of speed, with the timing of the opening coinciding with the arrival at the chopper of neutrons of the desired energy. There are several types of neutron choppers. Historically, the first neutron chopper developed was by Enrico Fermi to measure the thermal cross section of boron(217), and the modern day version of this vertical axis pulse shaping neutron chopper is known as a Fermi Chopper. The Fermi chopper spins at high speeds and has a slit package comprised of neutron absorbing material, and the channels are typically curved in a manner that provides optimal transmission of some desired peak energy. Frame overlap choppers are designed to block the neutrons from different accelerator or chopper pulses. This contamination is known as "frame overlap", hence the moniker. The frame overlap choppers may also be known as "bandwidth" choppers, as they also help to tailor long neutron pulses for energy dispersive beamlines, giving the neutron beam some "bandwidth" for the measurement.

[8] The Darwin width is used to describe the degree of mosaic in samples, and is a good measure of sample quality. The Darwin width for any crystal and can be determined by setting the crystal rotation to the Bragg reflection point, and then varying the angle of incidence of the beam and recording the count rate to watch the degree of drop-off of the Bragg scattering.

At spallation sources, a prompt flash of high-energy neutrons that escape complete moderation can create an unwanted fast neutron background. The "T-zero" chopper ameliorates this by blocking the prompt flash of neutrons from the incident proton beam at a spallation source. The "T-zero" choppers are usually large blocks of neutron absorbing material like inconel that spin in sync with the incident proton beam pulse. Pulse shaping or double disk choppers are comprised of two counter rotating disks that can provide a final tailoring of the neutron pulse before the sample. These may have variable speeds and openings to customize the energy resolution achieved at the beamline.

The neutron beam then travels down to the sample area, located some distance from the source. In some cases, there is an evacuated supermirror guide that slightly collimates the neutron beam, and can also assist in energy selection. The guide evacuation is done to reduce residual scattering from atmospheric elements. Mirrors are used because a neutron at a grazing incidence can be reflected with the refractive index n given by:

$$n = 1 - \frac{\lambda^2 N b_{\text{coh}}}{2\pi} - i\left(\frac{\lambda}{4\pi}\right)\mu \tag{4.44}$$

Where N is the atomic mass density, b_{coh} is the scattering length, and μ is the linear attenuation of the mirror. The neutron that strikes the mirror at a sufficiently small angle will be reflected, while neutrons of higher angle than this will be transmitted through the material. For low-energy beams, the use of neutron guides may improve flux transmission to the sample area by as many as two orders of magnitude(216)

Neutron collimators are also used to reduce the beam divergence. Linear collimators are effectively straight lines made of absorbing or strongly scattering material that are inserted into the beam path. Neutrons with a divergence less than the effective length of the collimator will be absorbed or scattered out of the beam path. Radial collimators can be used as well to reduce the degree of scattering away from a radial line - these are frequently found around sample environment equipment or along a line from the sample to a detector. The collimator principle is illustrated in Fig. 4.13.

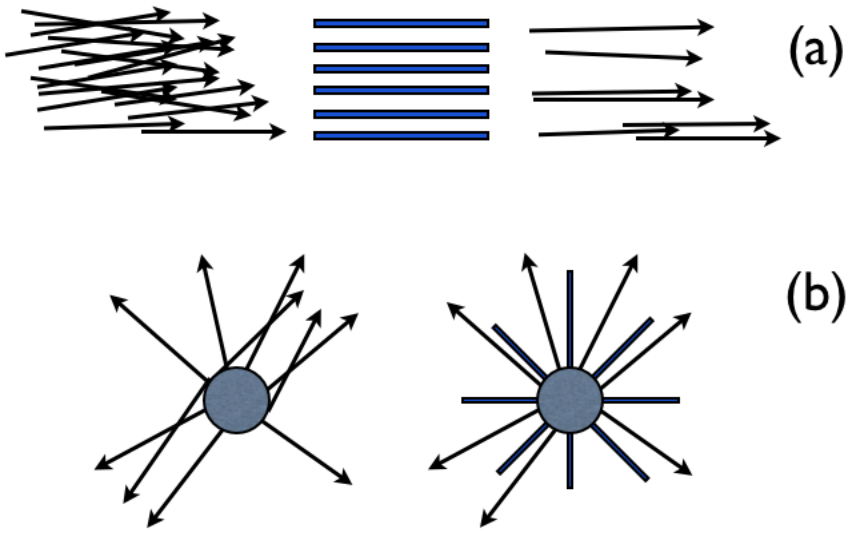

Figure 4.13: Illustration of collimator principles. Black arrows indicate neutron spatial paths, and blue lines illustrate absorbing material used in the collimators. (a) Linear collimator where divergent neutrons are removed by transiting narrow channels of absorbing material. (b) Radial collimator where divergent neutrons are removed from the radial path to the detector array.

While studying a sample in ambient conditions is interesting by itself, frequently one wants to study the properties of the sample as a function of some extensive variable, such as temperature or pressure, and the "sample environment" provides access to these extensive variable. Constructing sample environment equipment capable of providing the desired conditions with sufficiently low background remains a very large challenge in neutron scattering. The work in this dissertation studied materials as a function of temperature, and these temperature controlled studies were done largely with closed-cycle refrigerators and helium-exchange cryostats. Some of the work performed here was also done with the use of diamond-anvil cell (DAC) equipment, which is capable of providing high pressures - though these were limited to the x-ray experiments due to the large amount of equipment mass that one must put into the beam. Further, for single crystal samples, some rotational device is used to orient the sample in the beam to probe a certain direction of the crystal reciprocal space. These devices can usually be made

with a minimum of equipment in the beam, but there are quickly restrictions when using them in combination with other sample environments.

The sample a neutron scattering experiment must be of sufficient size that it will scatter neutrons in a manner that is time effective, but not so large that there is a substantial contribution from multiple scattering or is absorbs the neutron beam. This is particularly important in INS studies, where multiple scattering can be deleterious to data interpretation. Also, the contribution from hydrogen and water must be reduced, as hydrogen has a large incoherent scattering length[9], and the presence of water or hydrogen in a sample can easily dwarf the weaker inelastic scattering.

4.6.1 Neutron Detection

After interacting with the sample the scattered neutrons are collected in a detector. Many neutron instruments make use of ^{3}He detectors, increasingly constructed with position sensitivity. The position sensitive detector consists of a steel tube filled with pressurized ^{3}He gas with a long wire running down the center. A neutron enters the tube, interacts with a ^{3}He particle, creating an excited particle that rapidly decays into a very energetic triton. The triton then interacts with the the quench gas to produce a string of ionize particles that are attracted to the central wire. The ionized particles are then accelerated to the anode/cathode of the detector tube and recorded. The difference in time of the arrival of the pulses at the anode/cathode determines the position where the neutron absorption occurred.[10]

Neutron detection is also performed with scintillation materials. At the SNS, scintillating neutron detection is done with wavelength-shifting (WLS) fibers glued on top of ZnS/^{6}LiF scintillating plate(219; 220) The scattered neutron is absorbed by the ^{6}Li in the scintillating plate, resulting in emission of an alpha particle and tritium nucleus. These particles generate an ionization cascade in the scintillating plate, resulting in a light distribution peaked at 420 nm. A fraction of the photons emitted are able to

[9] See Sec. 4.2.1 for information about neutron scattering lengths.
[10] See Ref. (218) for more information.

diffuse through to the WLS fibers, where they are downshifted in wavelength, and then propagated along the fiber down to photomultiplier tubes using total internal reflection. (220) The fibers are double-layered to create an $x - y$ grid allowing for correlation of position information.

The WLS design has its roots in high energy physics, and is appealing for good timing discrimination, pixellation, and radiation hardness,(221) though its primary advantage is in reducing the size of the transport medium required to send the scintillation light to the photomultiplier tube. WLS fibers provide a mechanism to exploit the Liouville theorem of phase-space conservation by downshifting the energy of the collected photons, providing a factor of 10^4 reduction in required transmission area.(222) In addition to reducing the material needed to transport the scintillation signal, the WLS fiber improves light collection from scintillation by improving the match of the scintillation light to the absorption frequency of the photomultiplier tube, and reducing the likelihood of a reabsorption of an escaped photon by the scintillating material which would result in a spurious count.

After the detection event, the neutron events are collected in some manner of data analysis system. Advanced data collection techniques are available at the SNS. The data acquisition system (DAS) is based on the idea that each neutron detection is a unique event, and the data format is known as "event data format." In principle, every neutron has a unique timestamp identifying its arrival at the detector position, and this identifier can be correlated to a number of external parameters.

The varying needs of timing accuracy drive the design of the subsystems. Fundamentally, there are fast processes like the actual neutron detection requiring a real time response within 100 nanoseconds, and this is done mostly with custom built electronics. This “real time” component of the timing system allows the signal from the detected neutron to be collected by the detector electronics, and is then transmitted to a preprocessor via a high speed data link for aggregation and/or histogramming. The real time network also collects information from the chopper systems to help identify pulses that are not reliable because of chopper phase errors or other accelerator problems.

For ancillary systems that support the beamline science (e.g., temperature controllers), these are the millisecond range response systems, and have individual control computers that have custom interfaces written to the DAS (written usually in C++ or Labview), which communicate using national instruments data socket protocols, making them directly addressable elements on a private network. The output from these instruments is logged and stored with the neutron data on the SNS file system.

The clear advantage of this system is the ability to correlate neutron detection events with external time sensitive parameters lile pulsed magnetic fields(223), conducting experiments on *in-situ* application of strain(224), or with undesirable excursions in experimental setups (e. g., long beam-off periods or temporary loss of temperature control).

4.7 X-ray scattering

X-rays are used to probe condensed matter in the same manner as neutrons, though x-rays provide complementary information. Where neutrons probe the nuclear and magnetic interactions, x-rays scatter from the spatially extended electrons in a material, giving rise to a scattering that is essentially linear in Z, and dependent on the size of the electron cloud.

4.7.1 X-ray Production

X-ray sources can be lab bench equipment, but sources can be made substantially brighter through the use of light emitted from the bending of charged particle trajectories. Synchrotron sources are electron-beam accelerators that exploit the natural emission of *bremsstrahlung* radiation emitted when the electron's orbits are bent by magnetic fields. In synchrotron sources, the electrons are accelerated to speeds close to the speed of light, and their trajectories are controlled by magnetic fields. A radio frequency (RF) source restores the energy to the beam on each subsequent pass.

To zeroth order, the power of the emitted x-ray beam in a synchrotron is given by the fourth power of the relativistic γ of the electron beam over the square of the synchrotron radius, where the angular distribution is preferentially in the forward direction (where forward in this context describes the instantaneous velocity vector).

Synchrotron sources are particularly flexible, able to produce a range of photon energies that can be used in experiments and very high-brilliance beams. The important concern to the experimentalist is are the details of how beams are produced, as this relates to the spatial divergence, energy, and bandwidth of the x-ray beam. The *bremsstrahlung* radiation naturally has a white frequency distribution that is linearly polarized in the plane, with an out-of-plane divergence proportional to γ^{-1}. The white distribution can be altered with the use of specific insertion devices. The insertion devices use magnetic fields to locally perturb the electron trajectory, and have an impact on the spatial divergence and brilliance of the emitted beam.

There are four primary types of insertion device, the bending magnet, the wavelength shifter, the undulator, and the wiggler. The bending magnet is the simplest device, and is a simple dipole field that deflects the beam resulting in broadband x-ray emission. The wavelength shifter locally perturbs the radius of the synchrotron, and can be optimized for the desired energy range and horizontal divergence. An undulator is a periodic magnetic structure that produces interference effects that serve to increase the overall brightness while reducing the spatial divergence. A wiggler is a periodic magnetic structure similar to an undulator, but that more strongly perturbs the local orbit, resulting in a high brightness beam of increased horizontal divergence. The different insertion devices and their effect on the spatial divergence of the beam are shown in Fig. 4.14.

4.7.2 Inelastic X-ray scattering

The advent of the synchrotron source had a dynamic affect on research of the condensed matter, bringing intense, brilliant photon beams to bear on the very smallest of samples. As with neutron scattering, x-rays can also probe the interatomic distances in materials.

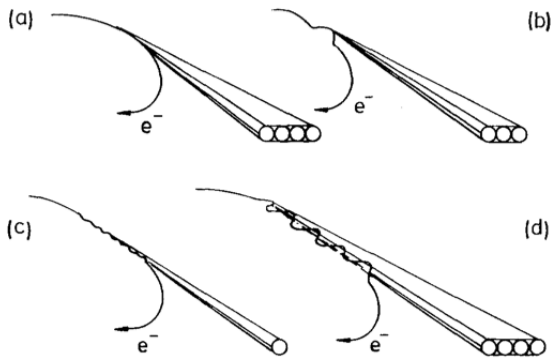

Figure 4.14: Insertion devices used at synchrotron sources. The cones are used to represent the horizontal beam divergences. $(\mathbf{a})$ bending magnet, $(\mathbf{b})$ wavelength shifter, $(\mathbf{c})$ undulator, $(\mathbf{d})$ wiggler. Image from (18).

However, neutrons with a wavelength suitable for the study of material excitations have an energy comparable to the energy of the excitation itself (of the order of a few to few hundred meV). For a synchrotron source, in order to study excitations of materials, the photon energy transfer would need to be of the order of tens of millielectron volts, while the incident beam energy of the photon beam is of the order of tens of kiloelectronvolts, thus requiring an energy resolution of $\frac{\Delta E}{E} \approx 10^{-7}$, a substantial technical challenge. Nevertheless, by exploiting a backscattering geometry, Burkel and colleagues demonstrated the proof of principle with the INELAX spectrometer at HASYLAB located at DESY in Hamburg. INELAX was able to obtain a resolution of 9.3 meV at the elastic line(225). The first published data on phonon dispersions was recorded in 1987 when 13.8 keV x-rays were used to measure the dispersion of phonons in a single crystal of Beryllium, obtaining an energy resolution of 55 meV(226). Developments in the analyzer construction quickly followed, with energy resolution reaching the 1.5 meV range(227; 228). Currently there are four instruments in the world capable of reaching this sort of energy resolution for inelastic measurements, two at the Advanced Photon Source at Argonne National Lab, one at the ESRF in Grenoble, and one at SPring-8 in Japan(229; 230).

The clever bit about inelastic x-ray scattering is the use of perfect silicon crystals in a backscattering geometry to achieve beams with a narrow energy bandwidth.

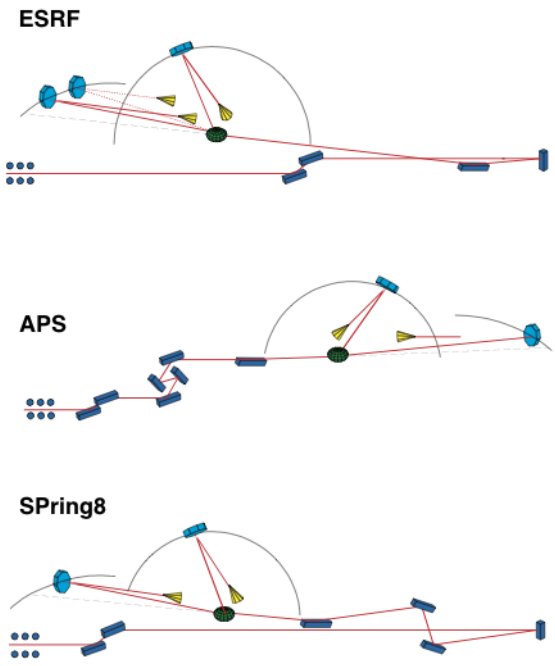

Figure 4.15: Schematic design of inelastic x-ray spectrometers at different facilities.

This also provides a benefit in momentum resolution, as traditional Cooper-Nathans formalism(209) for the determination of the inclination of the resolution ellipse $R(\mathbf{Q}, \omega)$ in $(\mathbf{Q}, \omega)$ space is zero, and collapses to a circle in $(\mathbf{Q}, \omega)$ space a backscattering geometry.

The inelastic x-ray spectrometer has a close analog in the neutron triple axis spectrometer. The initial beam energy is defined by an incident monochromator, and the loss or gain of incident photon energy is interpreted as an inelastic signal from the sample. The use of perfect Si monochromator crystals with high reflectivity make it possible to achieve very narrow bandwidth required for IXS scattering studies.

The advent of IXS has opened many avenues for research in condensed matter studies. In addition to making it possible to study lattice dynamics on μg of crystalline compounds, IXS is an excellent probe of higher energy optical modes in crystals, with little background and decoupled momentum resolution. Also, the method is substantially cleaner, leaving no activated material in its wake, and significantly reduced background over the neutron methods(231). Another advantage is the ability to go to very high

pressures to examine phonon dispersions, such as with a diamond-anvil cell. These experiments typically cannot be performed in a neutron beam due to the presence of the sample environment. The small and precise beam of IXS makes such experiments much more feasible.

As it applies here, IXS measures the sample scattering function $S(\mathbf{Q}, \omega)$, with the modification to account for the x-rays scattering from the electron cloud instead of the nuclear potential.

The scattering cross section for x-ray photons from the electrons in a sample again can be performed using the Born approximation, as the energies of the synchrotron photons are substantially higher than those of the lattice excitations. The Thompson scattering cross section:

$$\left(\frac{d\sigma}{d\Omega}\right) = r_0^2 \cdot (\mathbf{e}_i \cdot \mathbf{e}_f)^2 \cdot \left(\frac{\omega_f}{\omega_i}\right) \tag{4.45}$$

where $\mathbf{e_i}$ and $\mathbf{e_f}$ describe the polarization vector of the incident and outgoing photon. Because the final energy of the photon is very close to the incident (the incident photon energy is of order keV, and lattice excitations of order meV), the value $\omega_f/\omega_i \approx 1$, making the cross section for the interaction of the order of 0.1 barn. The cross section for x-ray scattering from dynamic magnetic features in a sample is still too low to be detected by modern synchrotron instruments(184), and developing techniques sufficiently sensitive to these features remains an open challenge.

4.7.3 Nuclear Resonant Inelastic X-Ray Spectroscopy

In NRIXS nuclear transitions of a very well defined energy are excited by x-rays having a very specific energy. The nuclear transitions have a very limited energy bandwidth (of the order 0.01 to 0.1 μeV near the nuclear transition), and these energies cannot be influenced by experimental apparatus, providing excellent energy references(232). By clever time discrimination, one can separate resonant nuclear scattering from non-resonant electronic scattering due to the lifetime of the nuclear levels. Prerequisites

for the technique include a source with a narrow bandwidth, and a beam which has sufficiently high energy to excite nuclear levels.

The mechanism of the NRIXS experiment is to place a flux of x-rays onto a sample that are tuned to a range near that of a nuclear resonance, and slowly sweep the beam energy through the resonance location (commonly used beam resonances shown in table **??**). The energy of the radiation scattered by the sample is analyzed using a resonance detector with a bandpass of 0.5 μeV, which is a large area fast-avalanche photodiode covered with a foil of enriched α-iron, with over 95% of the content the ^{57}Fe isotope. This detector is then placed below the sample, covering a large solid angle of acceptance, which accepts a range of momentum transfers between 1 and 15 Å^{-1}. The energy bandpass of the detector was determined by the process of resonant nuclear scattering. If the energy of the radiation coincided with the energy of the nuclear level, it excites the ^{57}Fe nuclei, and is reemitted with a time delay equal to that of the nuclear excited state (τ_0 = 141 ns). If the radiation has an energy far from that of the resonance, it appears in the prompt flash, and is not counted. A second detector is placed downstream of the sample to determine the zero point on the energy transfer axis. Count times are typically in the range of Hz for standard inelastic signals (i.e. phonons). NRIXS data are provided as intensity versus the angle of the monochromator crystals, which is then converted into intensity versus energy transfer. The first few bins on the low energy side are used to determine an energy independent background, and the elastic peak is removed using the measured instrument resolution function. Contribution from multiphonon processes is subtracted with a Fourier log method, and the phonon density of states is obtained by correcting for the thermal occupation factor(138).

Because the energy resolution of the detector is so high, the instrumental resolution is equal to the energy bandpass of the monochromator, which can be as low as 0.9 meV, but typically in the range of 1-1.5 meV, and is described in more detail in Sec. 4.7.2.

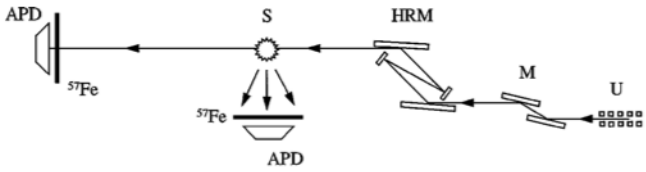

Figure 4.16: Schematic NRIXS setup with an avalanche photodiode.

Nuclear Resonant Isotopes		
Isotope	Res. Energy (eV)	τ (ns)
^{181}Ta	6.214	8730
^{169}Tm	8.410	5.8
^{83} Kr	9.404	212
^{73} Ge	12.263	4260
^{57}Fe	14413	141
^{151}Eu	21.541	14
^{149}Sm	22.496	10.2
^{119}Sn	23.88	25.7
^{161}Dy	25.651	40.5
^{40}K	29.83	6.1

Table 4.6: Isotopes with nuclear resonances within range of inelastic x-ray spectrometers, with resonant energy and lifetime. Data from(2)

5 Structure of FeSC

5.1 Structure of $BaFe_2(As_{1-x}P_x)_2$ and $Ba(Fe_{1-x}Co_x)_2As_2$

We present study of the average structures of $BaFe_2As_2$ $Ba(Fe_{1-x}Co_x)_2As_2$ (x=0.08, 0.1) and $BaFe_2(As_{1-x}P_x)_2$ (x=0.1, 0.2, 0.33, 0.7) as a function of temperature determined from time of flight neutron powder diffraction. The diffraction data evince a small but definite degree of negative thermal expansion in the samples exhibiting superconducting behavior, with onset of negative thermal expansion commensurate with the transition to the superconducting state. Negative thermal expansion is absent in fully paramagnetic specimens.

Using Rietveld refinement(195) on neutron time of flight diffraction data we present a study of the average and short-range atomic structure of isovalent and electronic substitution in $BaFe_2As_2$. The substitution of isovalent phosphorus for arsenic to form $BaFe_2(As_{1-x}P_x)_2$ (x=0, 0.2, 0.33, 0.7) allows an examination of the local changes in tetrahedral shape, while electronic doping with cobalt to form $Ba(Fe_{1-x}Co_x)_2As_2$ (x=0, 0.08, 0.1) allows investigation of the disorder induced in the iron layer. We report two key results. First, we show that the effect of chemical substitution is to modify the long-range structure in the paramagnetic, non-superconducting states, in a way commensurate with chemical substitution and other experimental reports, but that in the case of phosphorus doping, the changes in Fe-Pn bond lengths are driven mostly by compression along the $a-b$ plane and not due to a changing separation of the Fe-Pn layers along the c-axis.

Second, we find that there are finite regions of null or negative thermal expansion of the c-axis below T_c in samples exhibiting superconductivity.

Neutron time-of-flight powder diffraction experiments were conducted at the Manuel Lujan Neutron Scattering Center at Los Alamos National Laboratory using the NPDF and HIPD powder diffractometers(233), and at the Spallation Neutron Source at Oak Ridge National Laboratory using the POWGEN diffractometer(234). The $Ba(Fe_{1-x}Co_x)_2As_2$ samples were single crystals ground into a powder while $BaFe_2(As_{1-x}P_x)_2$ samples were prepared by powder synthesis. Samples were then sealed in vanadium cans backfilled with helium gas, and a helium cryostat was used to perform the temperature studies at Lujan, while the rapid sample changer FERNS was used at POWGEN. The crystal structure of the parent compound $BaFe_2As_2$ in the tetragonal and orthorhombic states is shown in Fig. (5.1).

The diffraction data were analyzed using Rietveld refinement as implemented in GSAS.(196) An impurity phase of Fe_2P was identified in all P doped samples. The structural data on the impurity Fe_2P was obtained from the International Crystallographic Structural Database(235; 236; 237). In all refinements, the lattice parameters, atomic positions, relative phase mixture, diffractometer zero, u_{iso} factors, and profile terms were refined. The profiles used in GSAS refinements were profile function 1 for NPDF, -3 for POWGEN, and 4 for HIPD data. In all cases the background was described as a 15 term Chebyshev polynomial. Sample absorption was refined for the lowest temperature for each sample and then held fixed. Select refinement parameters for $BaFe_2As_2$ are shown in Tab. 5.1, while results for $BaFe_2(As_{1-x}P_x)_2$ are shown in Tab. 5.2 and 5.3.

We focus on two key points: the effect of chemical substitution on the structure, and the presence of NTE. First, Co and P doping of $BaFe_2As_2$ both follow Vegard's Law, with the c-axis exhibiting a linear decrease in length as a function of substitution (P case shown in Fig. 5.2b). For the P doped case, Rietveld results show that the As and P atoms assume distinct z positions in the structure, commensurate with the results of (238). Looking at the perpendicular distance of the pnictogen to the iron plane (z_P, z_{As}) we find that the z_P, z_{As} distances are composition-independent (Fig. 5.3). Recent studies

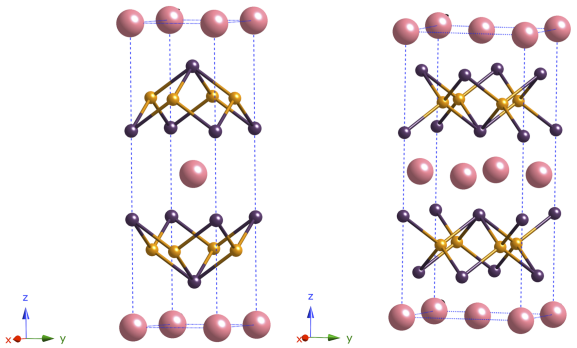

Figure 5.1: Unit cell of $BaFe_2As_2$ in the paramagnetic tetragonal state (left), and antiferromagnetically ordered orthorhombic state (right). Ba atoms pink, Fe atoms golden, As atoms purple.

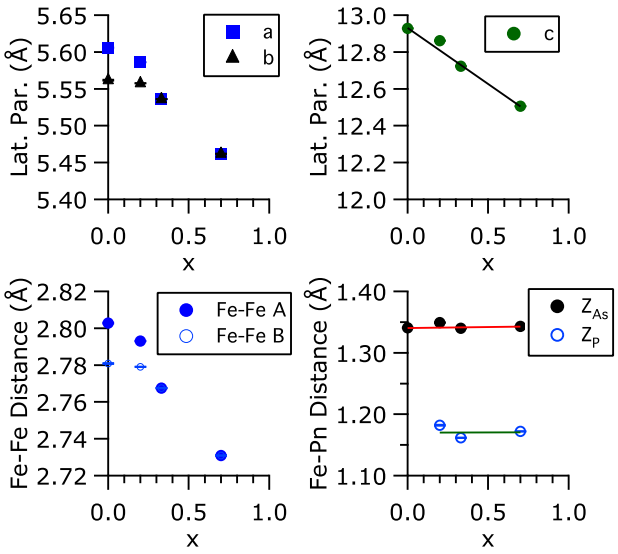

Figure 5.2: (upper left) a/b lattice parameter evolution as a function of P doping for data at 15K. Values for $x > 0.2$ are multiplied by $\sqrt{2}$. (upper right) c-axis evolution as a function of P doping obtained from Rietveld refinement at 15K (20 K for x = 0.2). Straight line is linear fit to the data showing the system exhibits a Vegard's law dependence. (lower left) evolution of Fe-Fe plaquette side distances as a function of doping. Data are obtained from Rietveld refinement and are at 15 K (20 K for x = 0.2). (lower right) P-z, As-z values obtained from Rietveld refinement at 15 K (20 K for x = 0.2). Straight lines are linear fits to the data. There is little compositional dependence of the z distance above the Fe plane for either As or P.

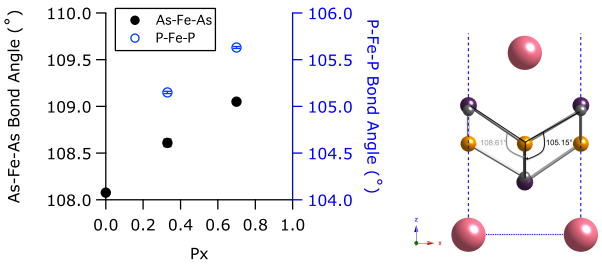

Figure 5.3: (left) Evolution of Pn-Fe-Pn bond angle as a function of composition. The z-distance of the As, P atoms above the Fe plane (Fig. 5.2) indicates that the angular changes are due to contraction of the lattice along the $a-b$ plane (right) Lower half of the unit cell of $BaFe_2(As_{1-x}P_x)_2$, x = 0.33 emphasizing the dissimilar tetrahedral bond angles for As and P . The sites are shown with double occupancy to emphasize the distinction in height of the P and As above the Fe plane.

of the simultaneous doping of Co and P into $BaFe_2As_2$ have shown that the maximal T_c is obtained in the absence of one or the other dopants,(239), suggesting that the distinction in bond lengths is responsible for the suppression of the magnetic spin-density wave (SDW) phase. The composition independence of the z_P, z_{As} in $BaFe_2(As_{1-x}P_x)_2$ observed in our study suggests that the suppression of the magnetic ordering is not due to a change in the distance of the pnictogen above the iron plane, but is due instead to the contraction of the system along the $a-b$ plane.

Next we address the topic of negative thermal expansion (NTE). The evidence of null or NTE of the optimally doped systems shown in Figs. 5.4 and 5.5 where the c-axis lattice parameter obtained from the Rietveld refinement is scaled by the value at base temperature. NTE has been demonstrated in dilatometry studies on FeSC.(134; 240; 241) The presence of NTE in this and other superconducting samples is a clear indication of magnetostrictive behavior in the long-range structure. The degree of NTE in the system is small, and it is fair to question whether the observed NTE can be explained by typical lattice expansion behaviors. We believe this can be ruled out by the following argument. In the absence of strong magnetoelastic effects, the lattice expansion should follow similar behavior in the paramagnetic non-superconducting over-doped compound as the superconducting compound. As can be seen in Fig. 5.4a, the degree of lattice expansion is greater for the overdoped, non-superconducting compound than

the optimally superconducting compound. Further, our data show that superconductivity occurs in the absence of a pronounced c-axis lattice collapse, allowing us to draw a parallel with the $CaFe_2As_2$ system. In the collapsed tetragonal state of $CaFe_2As_2$(242) the degree of hybridization between the Fe and As atoms has a strong impact on the Fe spin state(132). The absence of an abrupt c-axis collapse in this system as in $CaFe_2As_2$ indicates that the Fe and As states are strongly hybridized, contributing to a strong magnetoelastic coupling, a natural extension of which is NTE. Further, we posit that the presence of NTE indicates spin-phonon coupling in the system. The c-axis-polarized Raman-active mode in $Ba(Fe_{0.92}Co_{0.08})_2As_2$ corresponding to the oscillation of the As atoms orthogonal to the Fe plaquette is shown to be several meV softer than DFT calculation, requiring the explicit inclusion of magnetism to describe the softening.(106) A Landau mean field theory(243; 9) developed from the description of the perpendicular distance between the As atoms and the Fe plaquette shows that the softening of the mode indicates the presence of spin-phonon coupling in the system. That the lattice resists expansion along the c-axis up to the T_c for the $Ba(Fe_{0.92}Co_{0.08})_2As_2$ system further confirms the extent of this spin-phonon coupling.

The preceding has presented a detailed study of the average structure for isovalent and electronic substitution in $BaFe_2As_2$. We show evidence from neutron powder diffraction of null or NTE in the superconducting compounds, with the onset of NTE behavior at the sample T_c. NTE behavior is absent in the paramagnetic overdoped compounds. The presence of NTE in the superconducting state and absence in the paramagnetic, over-doped, non-superconducting state provides evidence of strong magneto-elastic coupling in the superconducting systems. We have also shown that the effect on the chemical structure is largely commensurate with doping expectations, but that the changes in the Fe-Pn bonds is due more in part to the contraction of the system along the $a - b$ plane than along the c-axis.

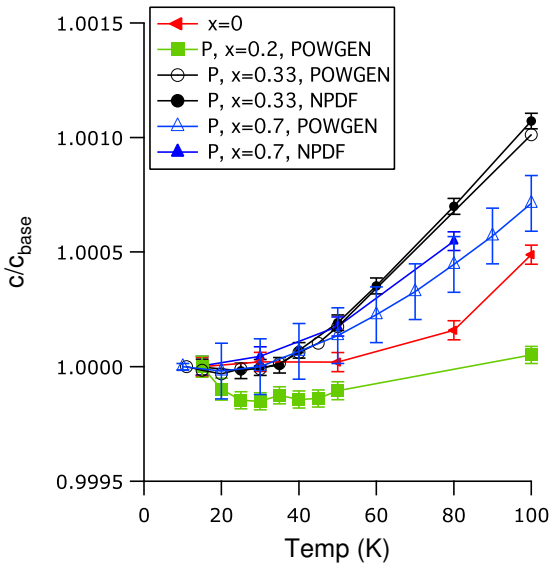

Figure 5.4: (a) c-axis lattice parameter data scaled by the value at base temperature for $BaFe_2(As_{1-x}P_x)_2$, x = 0 (red, $T_N \approx 140$ K), 0.2 (green, $T_N \approx 120$ K, T_c approx 4 K) 0.33 (black, $T_c \approx 30$ K), 0.7 (blue, non-superconducting, non-magnetic). Lines are guides to the eye.

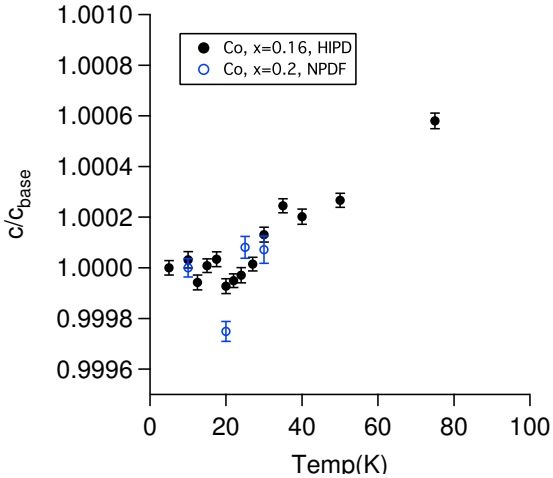

Figure 5.5: c-axis lattice parameter data scaled by the value at base temperature for $Ba(Fe_{1-x}Co_x)_2As_2$, x = 0.16 (black, $T_c \approx 22$ K), 0.20 (blue, $T_c \approx 18$ K).

Table 5.1: Rietveld refined parameters for $BaFe_2As_2$ at 15 K and 148 K obtained from GSAS.

Temperature	15K	148 K
Space group	$Fmmm$	$I4/mmm$
a (Å)	5.6067(15)	3.95171(9)
b (Å)	5.5628(15)	–
c (Å)	12.9281(3)	12.9440(3)
Volume (Å^3)	403.210(19)	202.13(1)
Ba	(0,0,0)	(0,0,0)
	u_{iso} = 0.0031(4)	u_{iso} = 0.0056(5)
Fe	$(\frac{1}{4}, \frac{1}{4}, \frac{1}{4})$	$(\frac{1}{2}, 0, \frac{1}{4})$
	u_{iso} = 0.0029(27)	u_{iso} = 0.0053(3)
As	(0,0,z)	(0,0,z)
	z = 0.35381(8)	z = 0.35370(9)
	u_{iso} = 0.0031(3)	u_{iso} = 0.0053(3)
R_p, wR_p	0.0481, 0.03386	0.0550, 0.0388
χ^2	1.656	1.83

Table 5.2: Selected refinement parameters for $BaFe_2(As_{1-x}P_x)_2$ compositions from the POWGEN instrument.

x	0.2	0.2
Inst.	POWGEN	POWGEN
T (K)	30	100
Sym.	$Fmmm$	$Fmmm$
a (Å)	5.5552(1)	5.5671(2)
b (Å)	5.5841(1)	5.5754(2)
c (Å)	12.8610(3)	12.8630(3)
u-Ba	0.0012(2)	0.0024(2)
u-Fe	0.0021(1)	0.0027(1)
u-As	0.0015(2)	0.0016(2)
u-P	–	–
As-z	0.3549(1)	0.3549(1)
P-z	0.3419(4)	0.3414(5)
R_{Wp}	0.0368	0.0386
χ^2	2.342	2.591

Table 5.3: Selected refinement parameters for $BaFe_2(As_{1-x}P_x)_2$ compositions from the NPDF instrument.

x	0.33	0.33	0.7	0.7
Inst.	NPDF	NPDF	NPDF	NPDF
T (K)	15	100	15	100
Sym.	$I4/mmm$	$I4/mmm$	$I4/mmm$	$I4/mmm$
a (Å)	3.9139(3)	3.9144(2)	3.8618(2)	3.8626(1)
b (Å)	–	–	–	–
c (Å)	12.723(1)	12.7372(96)	12.5064(9)	12.5173(5)
u-Ba	0.0035(4)	0.0053(4)	0.0035(3)	0.0050(7)
u-Fe	0.0036(2)	0.0045(2)	0.0035(2)	0.0038(4)
u-As	0.0027(4)	0.0036(4)	0.0028(2)	0.010(2)
u-P	0.0007(1)	0.0004(1)	0.0024(4)	0.0013(1)
As-z	0.3553(1)	0.3552(1)	0.3574(7)	0.3566(9)
P-z	0.3414(4)	0.3414(4)	0.3437(3)	0.3441(5)
R_{Wp}	0.0387	0.0357	0.040	0.051
χ^2	1.579	1.390	1.363	1.116

5.2 Pair Distribution Function Analysis of Pnictides

Neutron time-of-flight powder diffraction experiments were conducted at the Manuel Lujan Neutron Scattering Center at Los Alamos National Laboratory using the NPDF and HIPD powder diffractometers.(233) A polycrystalline sample of $BaFe_2As_2$ was prepared using powder synthesis methods (T_N = 138 K). Samples were sealed in extruded vanadium sample cans backfilled with helium gas, and placed into a helium exchange cryostat for temperature controlled studies; samples were exposed to the neutron beam for 4 hours. The diffraction data were analyzed by Rietveld refinement as implemented in GSAS.(196) Rietveld refinement of the diffraction pattern at 30 K is shown in Fig. 5.7a. Refined parameters from the Rietveld analysis include the lattice parameters, isotropic thermal parameters, diffractometer zero, absorption, and profile parameters. The z position of As is not restricted by symmetry and was refined.

PDF data were produced using PDFGetN(244) and PDF modeling and fitting were performed with PDFgui(245). The Rietveld structural model was the starting model for the PDF analysis. Initial fits of the PDF to the Rietveld structural result are poor (Fig.

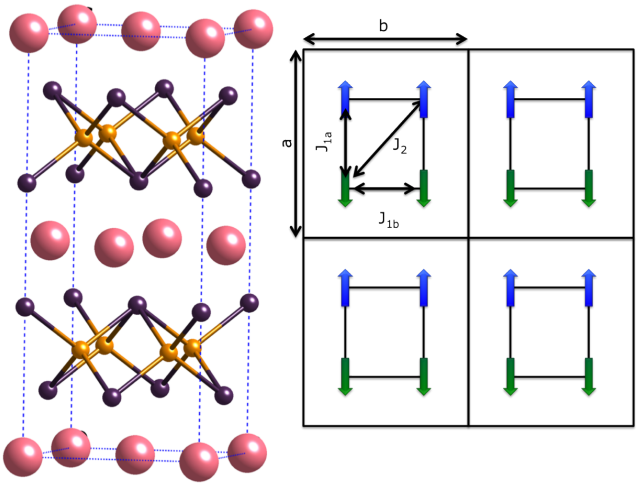

Figure 5.6: Orthorhombic crystal structure and spin alignment of $BaFe_2As_2$ as suggested by neutron scattering experiments. Magnitude of experimentally determined exchange constants decreases with the relationship $J_{1a} > J_2 > J_{1b}$.

5.7b). The short range fit (2 - 4.2 Å) is most poorly described by the Rietveld data (Fig. 5.8a) while PDF data at the long range (10 - 20 Å) is better fit (Fig. 5.7b). Allowing lattice parameters and isotropic thermal factors to be free parameters to the fit, we find that the fit is markedly improved (Fig. 5.8b) and that different lattice parameter values describe the system for the different fitting ranges. The Fe-Fe distance changes to reflect the change in the lattice parameters as a function of fitting distance (Fig. 5.10).

We characterize the behavior of the $a - b$ plane through a quantity orthorhombicity, defined as: $\mathcal{O} = \frac{a-b}{a}$. The value of the $\mathcal{O}$ is maximal at the shortest fitting range measuring 1.38%. For comparison, the value determined from the Rietveld refinement is 0.78%, representing a 60% increase in $\mathcal{O}$ at the short range.

As observed above, the structural model obtained from Rietveld refinement fails to accurately describe the local structure data obtained from the PDF. At the shortest range (2 - 4.2 Å) the fit is poorest (Fig. 5.8), exhibiting a crossover at 10 Å where the Rietveld refinement and PDF models converge (Fig. 5.7b). The discrepancy in the lattice parameter and resultant increase in $\mathcal{O}$ at the short range shows that $BaFe_2As_2$ is locally distorted. Fundamentally, the increase in the lattice constant at the shortest range shows that the inter-atomic distances at the shortest range are not well described by the average

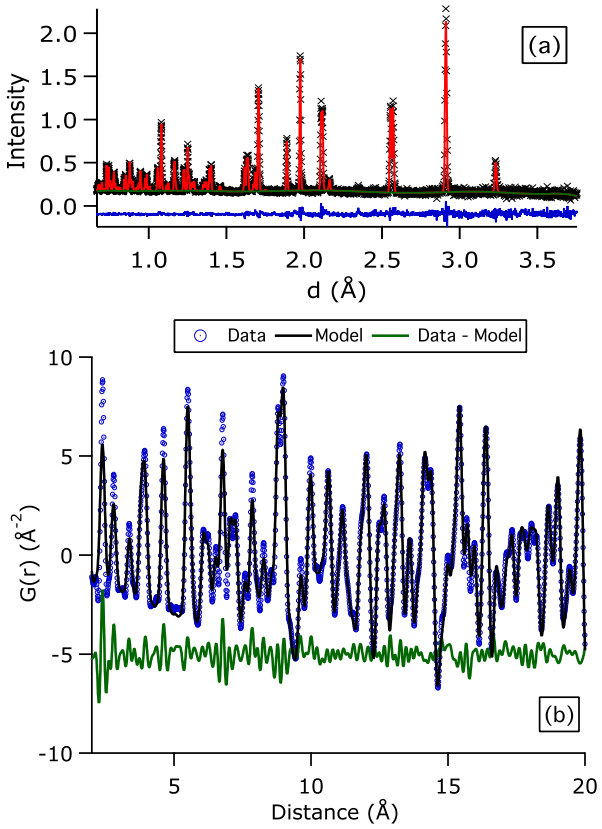

Figure 5.7: a) Rietveld refinement for $BaFe_2As_2$ at 30 K. a = 5.60652(15) (Å), b = 5.56277(15) (Å), c = 12.9284(4) (Å), R_p = 0.0301, χ^2 =1.657. b) PDF data compared to structural model from Rietveld refinement. The Rietveld obtained structural model deviates from the PDF most substantially at the shortest range, exhibiting a clear crossover at 10 Å. This crossover point shows that the local and long-range structure of $BaFe_2As_2$ are distinct, and that the long-range structure is well described by the Rietveld structural model.

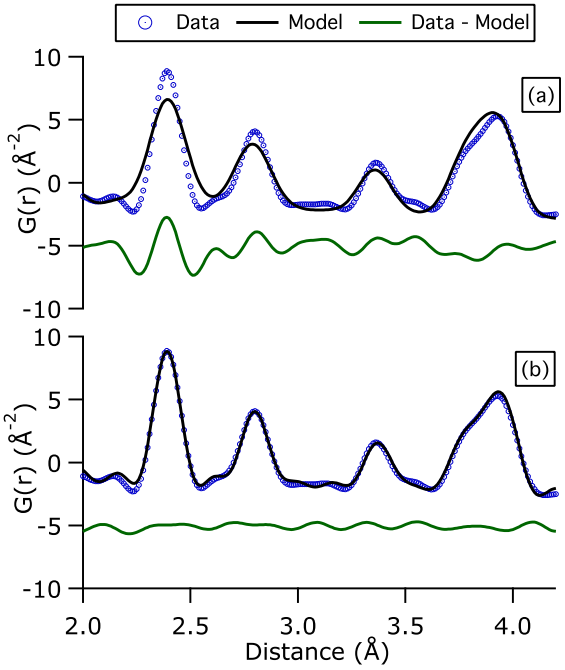

Figure 5.8: Comparison of short range (2 - 4.2 Å) PDF data to the (a) Rietveld and (b) refined PDF structural models. The Rietveld structural model deviates in peak positions at the Fe-As, Fe-Fe, and As-As distances, while the peak heights indicating the coordination in the local environment are not accurate. In b) the lattice parameters and isotropic thermal parameters are free parameters to the fit, improving the fit markedly.

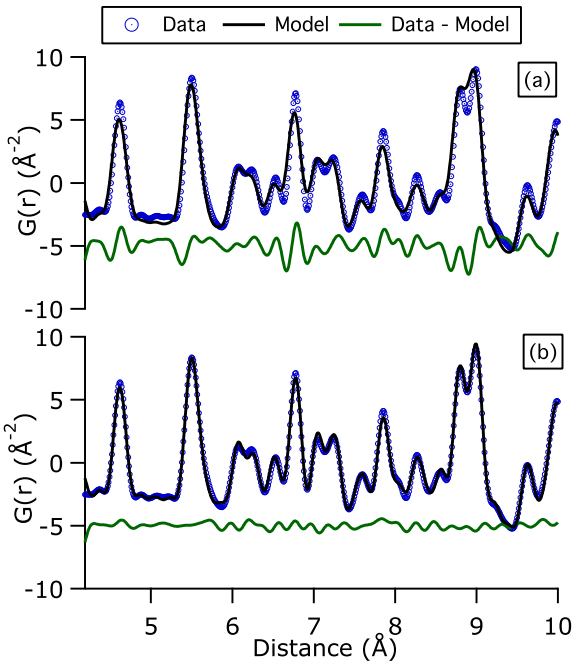

Figure 5.9: Comparison of medium range (4 - 10 Å) PDF data to the (a) Rietveld and (b) refined PDF structural models. As in the case of the short range data, the fit of the Rietveld structural model to the data improves when the lattice parameters and isotropic thermal factors are free parameters to the fit, shown in b).

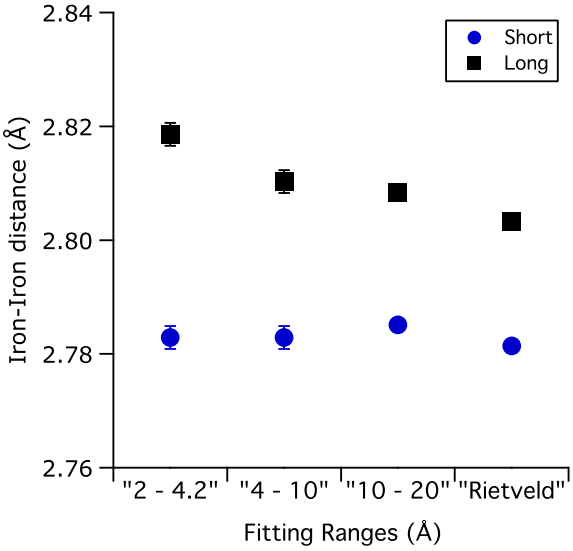

Figure 5.10: Iron bond lengths from fit PDF for $BaFe_2As_2$ at 30 K. The length of the long side of the plaquette gradually decreases as a function of fitting range reflecting the degree of short range distortion in $BaFe_2As_2$.

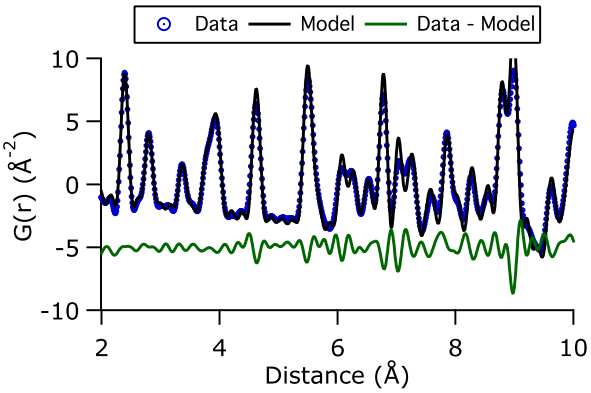

Figure 5.11: Application of the short range structure applied to the medium (4 - 10 Å) range structure. The short range structural model fails to describe the medium range structure, indicating that the short range structure of $BaFe_2As_2$ is distinct and distorted.

structure. The local stretching of the a-axis reflects an in-plane distortion of the iron plaquette, resulting in a plaquette that is longer along the a direction than the b direction at the short range (Fig. 5.10). Additionally, the short range structure from the fit PDF does not describe the medium or long-range structure (Fig. 5.11), showing that the local structure is distinct from both the medium and long-range structure.

In $BaFe_2As_2$, the magnetic exchange energy is greater along the longer AF direction, and smaller along the shorter FM direction. (12; 246) With a local in-plane distortion of the iron sublattice, the system will experience a geometrical frustration as the system compensates for the distortion. The frustration of the system from the distortion in the magnetic order serves to lower the magnetic moment through the flipping of the spins to preserve the shorter range FM correlation. In this scenario, the distorted plaquettes collectively form nano-domains, most naturally represented in a stripe-like formation (Fig. 5.13). The formation of nano-domains is distinct from effects of twinning, as powder diffraction measurements are insensitive to the effects of a macroscopic twin. Further, the distortion is not macroscopic, as the diffraction pattern lacks strong superlattice peaks.

The magnetic instability is further indicated in inelastic studies. The transverse acoustic phonon mode of $BaFe_2As_2$ softens as a function of temperature.(21) The softened mode corresponds to the shear mode of the system, resulting in the distorted

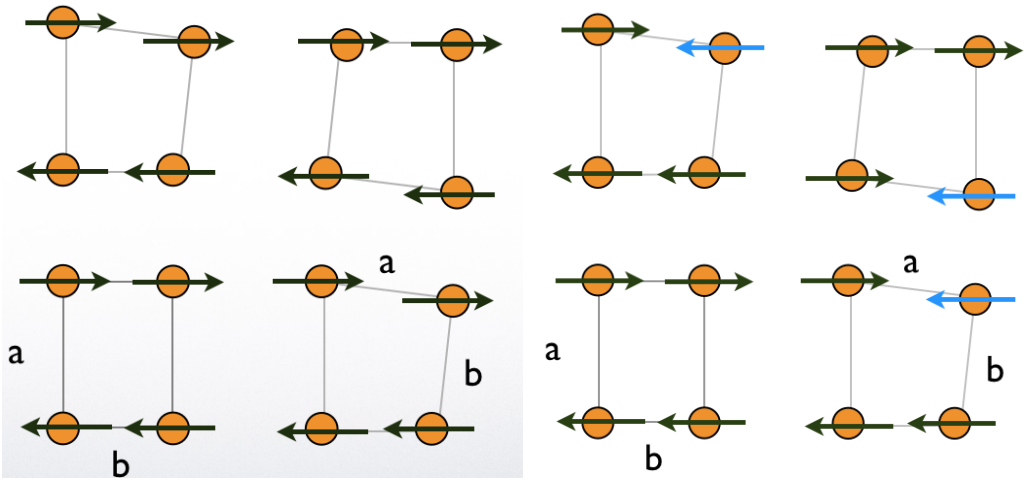

Figure 5.12: Demonstration of magnetic misalignment brought on by nano twin boundary formation. The figure on the left reflects the structural distortion, while the figure on the right represents the final spin alignment of the system. The light blue arrows indicate the spins most affected by the structural distortion.

structure. The softening of this mode starts well above the magnetostructural transition temperature of the system, indicating that the short range disorder sets in gradually becoming maximal at the point where long range order manifests. Further, the resulting increase in the magneto structural transition temperature by compressing the orthorhombic b-axis(153) is naturally explained by this model. By applying the uniaxial strain to the b-axis, the compression of the system along the FM ordered direction applies a mechanical force to the system, allowing the relief of the magnetic frustration and the increase in the onset temperature. The local disorder also explains the recent observation that it costs more energy to rotate the spin in in the $a - b$ plane than rotating it perpendicular to the FeAs layers(247). As the system already possesses the nano-domain disorder, the system naturally resists additional spin rotation due to the established frustration.

To conclude, we present evidence from neutron power diffraction for a local distortion of the $BaFe_2As_2$ system in the $a - b$ plane, resulting from the formation of nano-domains. The presence of the nano-domains prevents the full manifestation of static magnetic order in the $BaFe_2As_2$ system, lowering the static magnetic moment of the

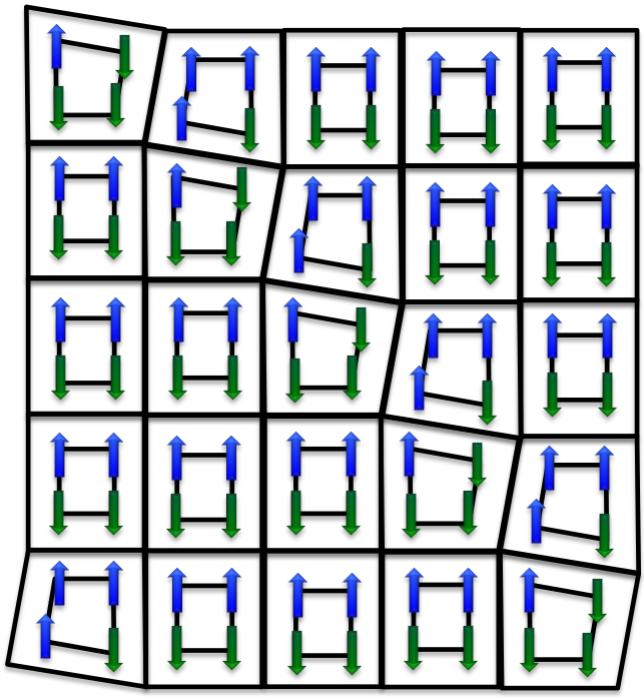

Figure 5.13: Suggested local distortion of $BaFe_2As_2$ with corresponding alteration of magnetic alignment. The distortion locally stretches the iron plaquette, forcing the spins to realign to maintain the exchange anisotropy. The spin misalignment results in an overall reduction of the magnetic moment of the system as measured by neutron diffraction. The $J_{1a} > J_{1b}$ relationship is maintained, while the J_2 AF interaction is weakened in the distorted plaquettes. The distorted plaquettes form a stripe like pattern that does not substantially impact the observed long-range order.

system. These observations are made in the as-grown compound $BaFe_2As_2$, absent any structural distortions that might be expected from chemical substitution, showing that the system exhibits a fundamental structural and magnetic frustration. This result addresses one of the fundamental questions in the study of high temperature iron-based superconductors, explaining that the source of the discrepancy between the DFT calculations and experimentally determined moments is derived from a reduction in overall moment due to structural distortion.

5.3 PDF analysis of doped compounds

Using the data obtained from our average structural refinements, we have made PDF models for compounds where Co is substituted on the Fe site, and for P substitution on the As site. The PDF is the sine fourier transform of the total scattering function $S(\mathbf{Q})$, and provides information about the local correlations between atomic sites. (198; 248). Structural effects from neutron and x-ray scattering have been presented in a number of FeSC. A study combining x-ray PDF and μSR demonstrates a conflict for electrons between the magnetic and superconducting states in the underdoped region of $Ba_{1-x}K_xFe_2As_2$.(144) PDF analysis on $FeTe_{1-x}Se_x$ shows direct variation in the local environments as a function of doping, leading to ambiguity in the structural phase identification for short atomic ranges.(146) A PDF study on non superconducting $BaFe_2Se_3$ demonstrated that introduction of local distortion to the lattice position of the iron atoms was indistinguishable in long-range Rietveld refinement, but provides a substantial improvement in the match of the local structural model to the experimental data.(147) A study of the superconducting phase of $Fe_{1.01}Se$ demonstrates a modulation of the crystal structure arising from displacements of the iron atoms.(148) A PDF study on SmFeAsO and superconducting $SmFeAsO_{0.85}F_{0.15}$ found a distribution of Fe-As distances(150) when compared to the average structural analysis obtained from Rietveld.(151)

Using Rietveld refinement(195) and PDF analysis(198), we present a study of the average and short-range atomic structure of isovalent and electronic substitution in $BaFe_2As_2$. The substitution of isovalent phosphorus for arsenic to form $BaFe_2(As_{1-x}P_x)_2$ (x=0, 0.2, 0.33, 0.7) allows an examination of the local changes in tetrahedral shape, while electronic doping with cobalt to form $Ba(Fe_{1-x}Co_x)_2As_2$ (x=0, 0.08, 0.1) allows investigation of the disorder induced in the iron layer. The PDF modeling indicates that there are finite local distortions in the $FePn_4$ layers, and that the assignment of a strict symmetry class in the paramagnetic state is ambiguous, indicating short-range structural distortions persist into the paramagnetic state. Finally, we observe that though the systems suffer large scale changes due to substitution, the degree of distortion in the short-range structure is independent of doping and temperature. This final observation is the most surprising, and the most complex.

Neutron time-of-flight powder diffraction experiments were conducted at the Manuel Lujan Neutron Scattering Center at Los Alamos National Laboratory using the NPDF and HIPD powder diffractometers(233), and at the Spallation Neutron Source at Oak Ridge National Laboratory using the POWGEN diffractometer(234). The $Ba(Fe_{1-x}Co_x)_2As_2$ samples were single crystals ground into a powder while $BaFe_2(As_{1-x}P_x)_2$ samples were prepared by powder synthesis. Samples were then sealed in vanadium cans backfilled with helium gas, and a helium cryostat was used to perform the temperature studies at Lujan, while the rapid sample changer FERNS was used at POWGEN. The crystal structure of the parent compound $BaFe_2As_2$ in the tetragonal and orthorhombic states is shown in Fig. 5.1.

The diffraction data were analyzed using Rietveld refinement as implemented in GSAS.(196) The refinements identified impurities in the compounds present at the level up to 4% of the primary phase. These were identified as FeAs (flux used to grow the sample) or Fe_2P. In none of the cases were the impurity statistics sufficient to ascertain more than the lattice parameters. The structural data on the impurity Fe_2P was obtained from the International Crystallographic Structural Database(235; 236; 237). The lattice parameters for the $BaFe_2As_2$ data at 15K as refined by Rietveld are all within 0.5% of

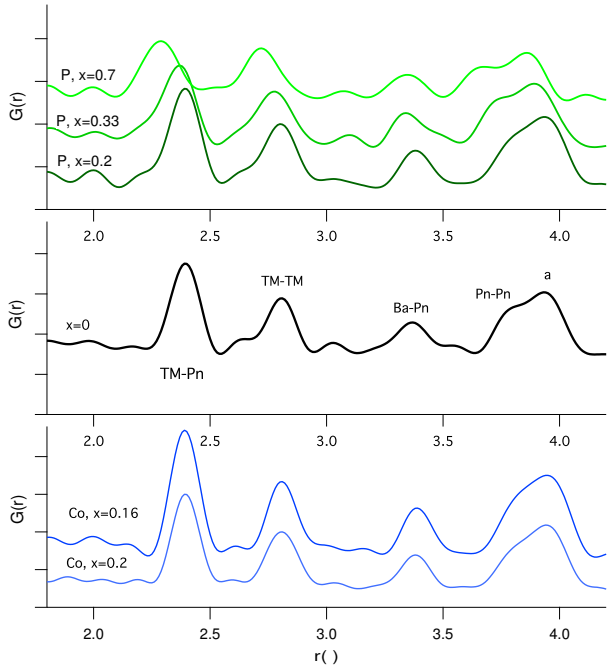

Figure 5.14: Comparison of PDF as a function of doping for system at 15K. $BaFe_2As_2$ is shown as thick black line in the middle (labeled x=0), labels indicating the interatomic pairs (TM=(Fe,Co), Pn=(As,P)). Increasing P content is shown above (shades of green), and increasing Co content below (shades of blue).

the values found in the literature(3). In all refinements, the lattice parameters, atomic positions, relative phase mixture, u_{iso} factors, absorption, and profile terms were refined. The profiles uses in GSAS refinements were profile function 1 for NPDF, -3 for POWGEN, and 4 for HIPD data. In all cases the background was described as a 15 term Chebyshev polynomial.

Reduced atomic pair distribution functions were obtained using PDFGetN(244), and PDFgui(245) was used to carry out structural refinements on the PDF data. The PDF is obtained by taking the sine fourier transform of the total scattering function $S(\mathbf{Q})$, which is the raw diffraction intensity corrected for sample self shielding, contributions from the container, and multiple scattering $G(r) = \frac{2}{\pi}\int_0^\infty Q[S(Q)-1]\sin(Qr)dQ$, where Q is the magnitude of the diffraction vector. The subtraction of 1 is to reduce termination errors in the transformed $G(r)$ by subtracting the background of uniform material density, and the integral is carried out to the maximal value of Q obtained in the diffraction measurement.

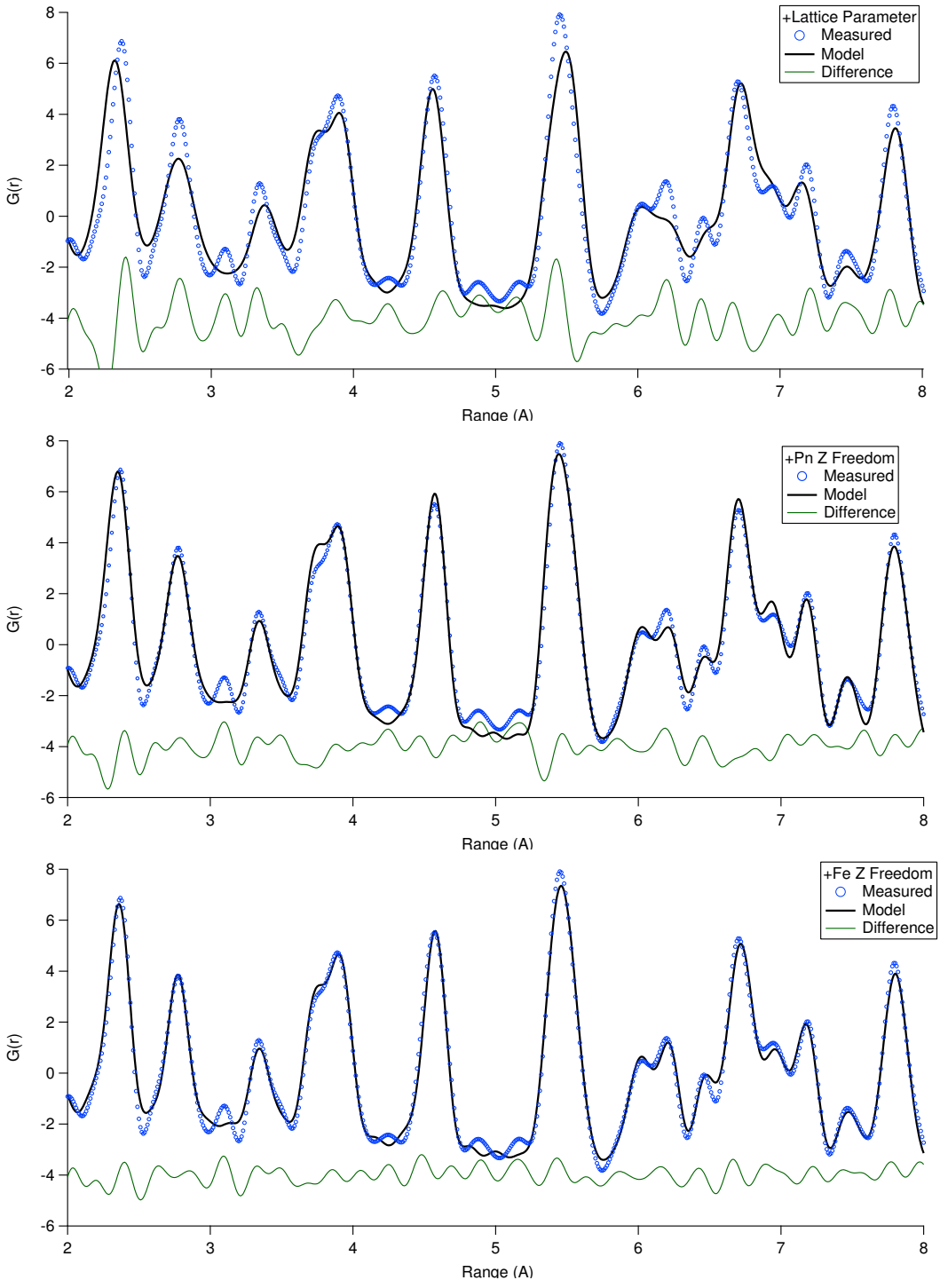

Figure 5.15: Fits to PDF models for $BaFe_2(As_{0.66}P_{0.34})_2$ at 15K. (top) Results from Rietveld refinement with lattice parameter allowed to refine. Clear discrepancies are note at 3.8 Å, 6 Å, and in the location of the first peak, which is underestimated by the Rietveld analysis. (middle) With lattice parameter, u_{iso}, and Pn-z allowed to refine the fit improves markedly at the 6 Å range. (bottom) With lattice parameter, u_{iso}, Pn-z, and Fe-z allowed to refine. The peak at 3.1 Å does not correspond to any distances in the local structural or Rietveld models, and is possibly termination error.

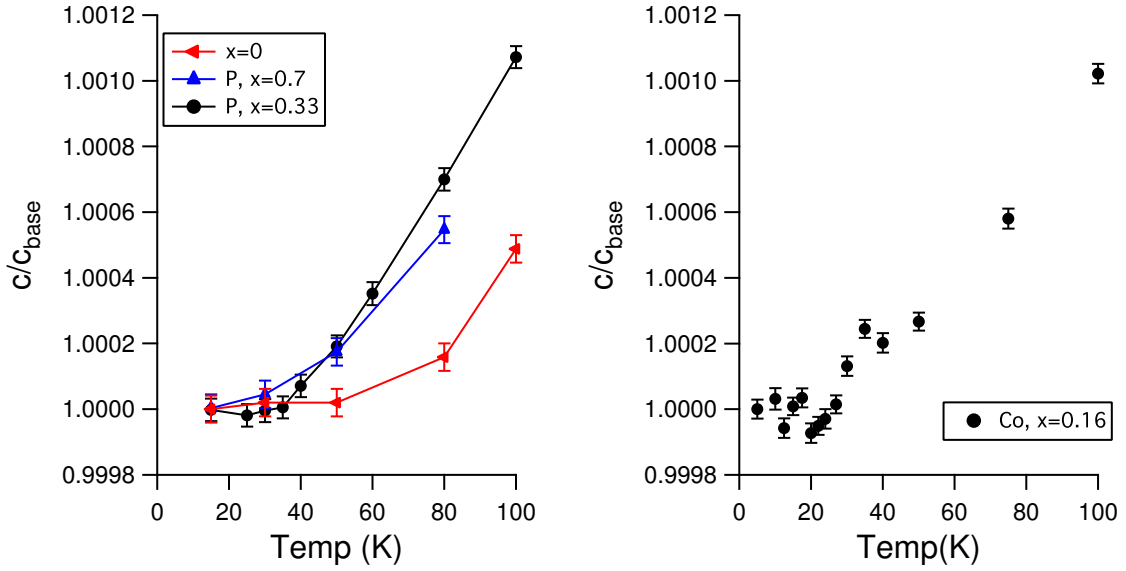

Figure 5.16: (left) Comparison of c-axis refinement data from Rietveld for $BaFe_2(As_{1-x}P_x)_2$, x=0, 0.33, 0.7. Lines are guides to the eye. (right) c-axis scaled data from Rietveld $Ba(Fe_{1-x}Co_x)_2As_2$ x=0.16.

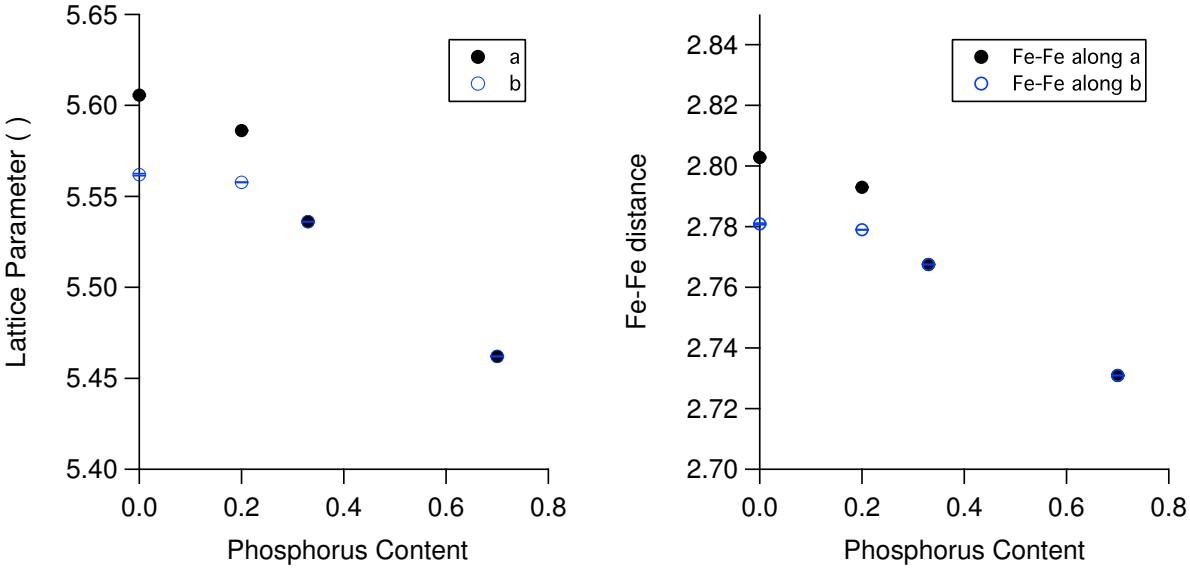

Figure 5.17: (left) a/b lattice parameter evolution as a function of P doping for data at 15K. (right) evolution of Fe-Fe cross plaquette distances as a function of doping. Data are obtained from Rietveld refinement and are at 15K.

The Rietveld results were used as the starting point for all PDF refinements. In Fig. **??**, the Rietveld result is applied to $BaFe_2As_2$ at 15K, and shows that Rietveld parameters fail to describe the structure below 10Å, but provide an adequate description of the structure at distances longer than 10 Å. Fig. 5.14 shows the PDF of all compounds over the range of 2 - 4.2 Å at 15K. At 15K, $BaFe_2As_2$ and $BaFe_2(As_{0.8}P_{0.2})_2$ are in the orthorhombic state, while the $Ba(Fe_{1-x}Co_x)_2As_2$, $BaFe_2(As_{0.66}P_{0.34})_2$, and $BaFe_2(As_{0.3}P_{0.7})_2$ are in the tetragonal state. At the shortest range, these symmetry distinctions are absent. The P-doped lattice contracts as the doping is increased, consistent with Vegard's law. Phosphorus substitution broadens the first PDF peak, which corresponds to the FePn_4 tetrahedra edge. Increasing P content serves to *shorten* the Fe-Fe neighbor distances, showing that the quenching of magnetism in the overdoped P case is partly the result of a constricted iron distance, and not solely the decrease of the FePn_4 distance.

For all materials, the PDF peak near 4 Å (which marks the a/b lattice parameter in the tetragonal state) has a well-defined shoulder corresponding to the Pn-Pn distance within the FePn_4 tetrahedron (tetrahedral edge). This peak becomes broader with increasing P content, and also more distinct from its own nearest neighbor (Fig. 5.14). If the tetrahedra were regular, the peak shoulder would be sharp, but instead we observe that it is broader compared to other interatomic distances, indicating distortion in the Pn-Pn distance.

PDF data were analyzed at a local range of r = 2 - 4 Å, and medium range for r = 4 - 10 Å, and then a long range of 10 - 20 Å using PDFgui. Peak fit analysis of the PDF data used gaussian functions convoluted with a the sinc function. The use of the gaussian peak to fit a PDF distance is most correctly applied in the case of a perfectly harmonic crystal(249), though the corrections to real data are at the one percent level.(250) Four models were used for quantitative PDF analysis. In all models, the lattice parameter, scale factor, and isotropic thermal values were free parameters to the model. The distinction between the models lies in the symmetry assignment class and the degree of c-axis freedom for the iron atoms (fixed or free to move from the fixed symmetry point). The first model fixed the symmetry in the tetragonal state with the Fe atoms restricted to their symmetry positions reported from the Rietveld analysis (model T_A). The second

model also used the tetragonal symmetry, but removed the constraint of Fe symmetry (model T_B). The third model reduced he symmetry to orthorhombic, and allowed the Fe atoms to move from their symmetry positions (model ORTH). The final model allowed the symmetry class to be fully relaxed to the P_1 class. In all cases, lowering the symmetry class and allowing the iron atoms to move from their fixed c-axis positions improves the fit to the data as measured by the improved weighted residuals. Further, lowering the symmetry class reduces the absolute values of the isotropic thermal factors from the Rietveld values, indicating that the Rietveld results are masking the effect of the local disorder with a larger value for the different u_{iso} values. Figure 5.15 shows data at 2 - 8 Å for $BaFe_2(As_{0.66}P_{0.34})_2$ in the cases of Rietveld data only, freedom of Pn-z and Fe-z positions.

The results from the Rietveld refinements are used as the starting point for PDF refinement. The Rietveld results fail to accurately describe the local structure, shown for the $BaFe_2(As_{0.66}P_{0.34})_2$ case at 15K in Fig. (5.15). After refinements of scale factors and lattice parameters, the discrepancy in the fits was still notable over the fitting range. By allowing Pn-z positions to vary, and the fits improve when there is a non-uniformity in the siting of the Pn-z. Reducing the local symmetry by allowing the iron atoms to vary from their symmetry restricted c-axis position improves the fit further, completely eliminating discrepancies at 6 Å and nearly eliminating discrepancies at 3.8 Å. This reduction indicates a buckling of the iron planes. This final case, relaxing the c-axis positions of the iron atoms improves the model fit to the data in all cases. The natural result of this type of buckling is a distribution of Fe-Pn bond lengths, and these are shown for the case of $BaFe_2As_2$ and $BaFe_2(As_{0.66}P_{0.34})_2$ in Fig. 5.18.

Our primary result is that there are small but finite distortions in the FePn_4 layers. These distortions are present in all of the compounds studied, including the undoped parent $BaFe_2As_2$, showing that the system possesses an intrinsic structural instability. In light of evidence regarding the sensitivity of the magnetic and superconducting properties on the structure of the FePn_4 layer. The distortions are of the order of 0.05 Å, are sufficient to result in substantial distortion of the magnetic properties in

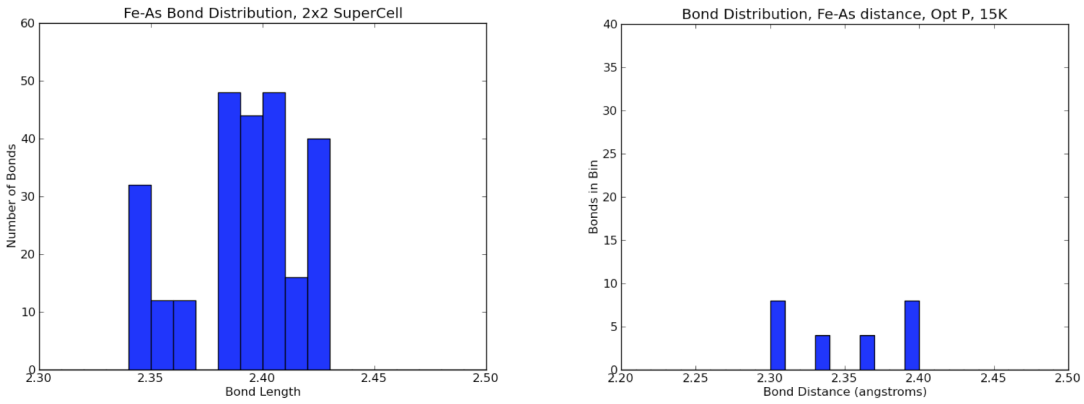

Figure 5.18: Bond length distribution for nearest neighbor (FePn_4) tetrahedral distances in (left) $BaFe_2As_2$ PDF model, and (right) $BaFe_2(As_{0.66}P_{0.34})_2$, both at 15 K. The difference in population is due to the difference in supercell considerations.

the case of $CeFeAs_{1-x}P_xO$, where a change of the presumed static FePn_4 distance of 0.01 Å reduces the magnetic moment by as much as 30% in the region approaching the Stoner instability.(10) Given a range of tetrahedral shapes, one will find a distribution of local magnetic density serving to modify the overall magnetic moment in the compound, reducing it from a value expected from DFT calculations. A computational result showing the impact of a distribution of static shapes on the electronic properties of the material is currently unexplored in the literature.

The best models for PDF data present when the structure is fully relaxed, and settles for an orthorhombically distorted state through to room temperature, with finite displacements of the iron atoms from their symmetry positions, consistent with the work of McQueen(148) and Malavasi(150) This is in contrast to the experiments of Joseph *et. al*, who find no serious deviations in structure at the local level at 300K(Ref. (145)), but we point out that these experiments used x-ray diffraction, and so are of lower real-space resolution than our neutron measurements. The ambiguity in the assignment of the local symmetry of $BaFe_2As_2$ at room temperature raises the possibility that the system is fundamentally unstable against the atomic motions. With locally orthorhombic character, the presence of strong electronic anisotropy existing in the tetragonal state(12) finds a natural explanation - the electronic anisotropy is the result of the locally orthorhombic

character distributed in the system, so the local breaking of the structural symmetry permits the C_4 symmetry breaking, enabling the electronic anisotropy.

Further, we point out that the displacements that we are assigning to a static distortion are of the level of the atomic displacement due to zero-point phonon amplitudes. If these displacements reflect phonons, they clearly indicate anharmonic phonon behavior. In the results of Malavasi(150) an assumption of anisotropic thermal factors was required to obtain a reasonable fit between the model and the PDF data, further bolstering this hypothesis. If the distortions are the result of phonons, this measurement serves to highlight that the phonons distort the local structure in a way as to impact dynamically alter the local symmetry, with resulting consequences for the magnetism.

Whether these distortions are truly the result of finite static distortions or dynamic structure effects such as phonons cannot be explicitly determined. We reiterate that the electronic properties of the system are strongly dependent on very small changes to the average structure, and that distribution of tetrahedral shapes in the compounds will locally affect the electronic properties. The implications of this work are twofold. The first implication is that the static structure descriptions obtained by traditional powder diffraction analysis may not provide an adequate starting basis for electronic structure calculations, and that to properly capture the electronic properties of the system, finite small distortions must be considered. The second is of a more profound nature, where we question the fundamental stability of the structure. The finite small distortions present in all compounds, including the undoped parent, highlight a fundamental instability of the system against static displacements, which is reflected in the anisotropic behavior of the electronic properties, and requires further investigation to be fully understood.

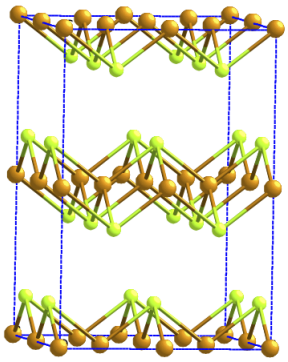

(a) Structure of FeTe(Se,S)

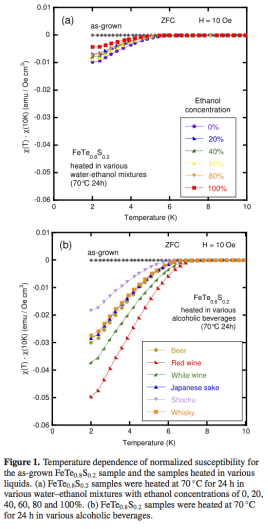

Figure 1. Temperature dependence of normalized susceptibility for the as-grown $FeTe_{0.8}S_{0.2}$ sample and the samples heated in various liquids. (a) $FeTe_{0.8}S_{0.2}$ samples were heated at 70 °C for 24 h in various water–ethanol mixtures with ethanol concentrations of 0, 20, 40, 60, 80 and 100%. (b) $FeTe_{0.8}S_{0.2}$ samples were heated at 70 °C for 24 h in various alcoholic beverages.

(b) Superconducting volume fraction as a function of heat treatment. Figure from (160).

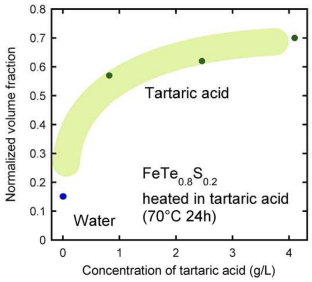

(c) Dependency of SC volume fraction on tartaric acid concentration (160).

5.4 Pair Distribution Function Analysis of Treated Iron Selenides

As grown (Fig. 5.19a) iron selenide compounds do not display superconductivity. With a certain level of treatment, most notably when heating in a bath containing a concentration of tartaric acid, or sulfuric acid, the selenides become superconducting with a high volume fraction (Fig. 5.19b, Fig. 5.19c)(160; 251). Tartaric acid is a primary component of commercially available red wines, and while the source of this change is believed to be the result of deintercalation of the excess iron by the acid, work remains to be done on understanding why alcoholic beverage treatments generally work to improve the superconductivity in the FeTe(Se,S) samples.

A series of samples with varying FeTe(S,Se) were subject to a variety of heat treatments and then analyzed using the PDF technique to study the changes in the local structure. Samples were pellets of polycrystalline material sealed in extruded vanadium cans supplied by the Takano group from , and sealed with indium wire in a helium

glove box with O_2 readings less than 1 ppm, and H_2O readings less than 5 ppm. The temperature of the samples is controlled using a closed cycle refrigerator or an orange cryostat. Data sets were collected for 20 minutes, with the SNS beam power at 1 MW. Also, the high count rate of the NOMAD instrument permits sampling the data on cool down ramps at a statistic suitable for basic data refinement and time series analysis of g(**r**), so these data were acquired as well. Temperature control was provided by a closed cycle cryostat and an orange cryostat. Background and vanadium standards were collected in both sample environments.

The powder diffraction pattern used for Rietveld refinements do not show substantial local disorder, but show a clear disparity in the level of background between the treated and untreated samples (Fig. 5.19), representing an overall increase in the diffuse scattering. The increase in diffuse scattering represents an increase in local disorder. In investigating the local structure, it is seen that the changing compositions are reflected in shifting peak heights, as would be expected from the different site coordinations.

The PDF integral is carried out to the maximal value of **Q** obtained in the diffraction measurement. In principle, this can be as high as 100 for the NOMAD instrument, but we have truncated the Fourier transforms at **Q**=25Å^{-1}, as the is the point at which the $S(\mathbf{Q})$ is essentially flat for all compounds, showing the breakdown of the long range structural coherence.

As noted above, the effect in compounds treated with tartaric acid is to remove excess iron from the structure(160; 251). However, the increased background in the treated samples compared to the as grown as shown in Fig. 5.19 is not fully borne out by this claim. The structure suffers from a high degree of intrinsic disorder, and it is possible that the tartaric acid treatment techniques serve to exacerbate the disorder, giving rise to the superconductivity.

The structure as developed from the PDF model shows that the treatment induces a level of disorder in the system that is not present in the as-grown compounds, with little change in the location of the iron atoms. It is clear that in these compounds, the impact of the local disorder plays an important role.

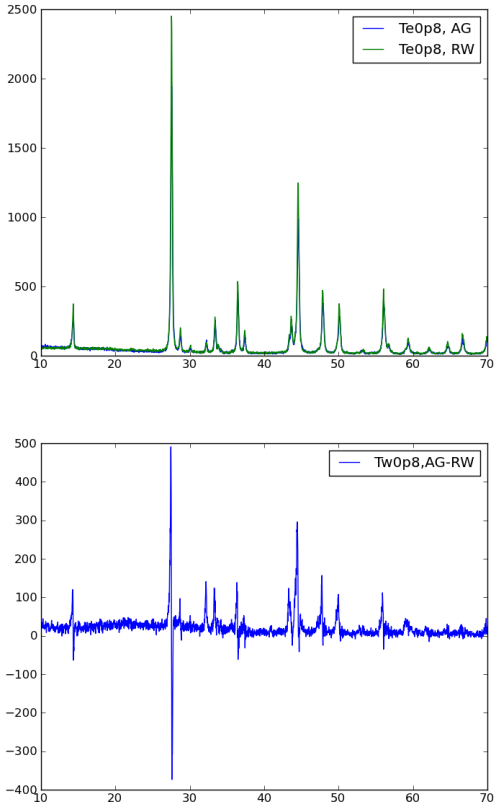

Figure 5.19: Comparison of diffraction patterns measured at NOMAD at the SNS and difference pattern showing the increase in background of the red wine annealed sample over the as-grown.

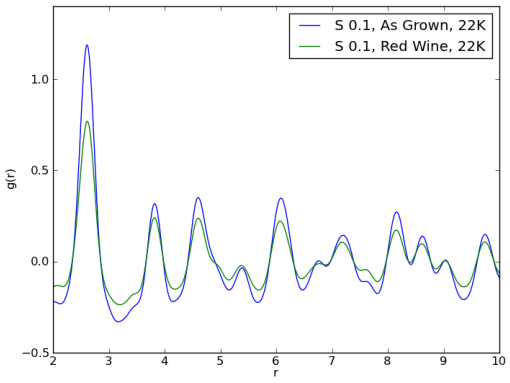

Figure 5.20: Comparison of PDF for the as-grown and red-wine annealed samples of S = 0.1 doping. Difference in intensity is related to sample normalizations.

6 Dynamics of FeSC

6.1 Phonons in FeSC

To eludicate mechanisms of exotic coupling between the spin and lattice degrees of freedom in iron-based superconductors (FeSC), we must study the direct momentum and energy dispersion relations. inelastic neutron scattering (INS) [1] is a powerful tool to make these determinations, so a series of several experiments on the role of spin-phonon coupling in the FeSC system has been conducted using time-of-flight (TOF) and triple-axis spectromter (TAS) spectrometers, as well as inelastic x-ray scattering (IXS).

In INS and IXS, the neutrons or photons are able to excite or de-excite lattice vibrations by imparting or removing energy from the structure, and the scattered neutrons are analyzed for their energy and momentum dependence.

The dynamic structure factor provides the scattering amplitude for a neutron scattering from a phonon polarized along ξ_{js}, where $\mathbf{d}_j$ is the position of the atom in the unit cell.

$$\mathcal{F}(\mathbf{Q}) = \sum_j \frac{\bar{b}_j}{\sqrt{m_j}} (\mathbf{Q} \cdot \xi_{js}) e^{i\mathbf{Q}\cdot\mathbf{d}_j} e^{-W_j} \tag{6.1}$$

The dynamic susceptibility of the system undergoing a single event of phonon creation or destruction is:

[1] See Chap. 4, in particular Sec. 4.4 for an extensive review of neutron scattering techniques and information about the instruments used in these studies.

$$\chi^{''}(\mathbf{Q},\omega) = \frac{1}{2}\frac{(2\pi)^3}{v_0}\sum_{\mathbf{Gq}}\delta(\mathbf{Q}-\mathbf{q}-\tau)\sum_{s}\frac{1}{\omega_{\mathbf{q}s}}|\mathcal{F}(\mathbf{Q})|^2 \times [\delta(\omega-\omega_{\mathbf{q}s})-\delta(\omega+\omega_{\mathbf{q}s})] \quad (6.2)$$

where $\omega_{\mathbf{q}s}$ is the frequency of the particular phonon.

In FeSC, the impact of electron phonon coupling was initially thought not to be of sufficient strength to account for the superconductivity(104; 103; 252), though the coupling strength improves with the explicit inclusion of magnetism(105).

As part of this work, a number of studies of the properties of phonons in FeSC, in particular the pnictide families, were carried out, focusing on the changing behavior of the phonon system as a function of temperature and doping. By using both $SrFe_2As_2$ and $BaFe_2As_2$, the impact of the alkali earth metal as a spacing layer allows one to examine the changing force constants of the material, while the doping allows an examination of the phonon behavior as a function of changing disorder in the material.

6.2 Phonon softening in $BaFe_2As_2$

In this section we present the results of an inelastic x-ray scattering experiment detailing the behavior of the transverse acoustic [110] phonon in $BaFe_2As_2$ as a function of temperature. When cooling through the structural transition temperature, the transverse acoustic phonon energy is reduced from the value at room temperature, reaching a maximum shift near inelastic momentum transfer $\mathbf{q} = 0.1$. This softening of the lattice results in a change of the symmetry from tetragonal to orthorhombic at the same temperature as the transition to long-range antiferromagnetic order. While the lattice distortion is minor, the anisotropy in the magnetic exchange constants in pnictide parent compounds is large. We suggest mechanisms of electron-phonon coupling to describe the interaction between the lattice softening and onset of magnetic ordering.

We investigated the behavior of the transverse acoustic phonon mode in $BaFe_2As_2$ near the $(2,2,0)_O$ position, which is the [110] mode in the reduced scheme. The

orthorhombic notation and the $Fmmm$ symmetry are used throughout this report. The measurements were made using the HERIX instrument on beamline 3-ID of the Advanced Photon Source at Argonne National Laboratory(253; 254). The HERIX instrument is on an insertion device beamline with a six-bounce monochromator setup providing an incident energy of 21.657 keV, and a resolution of 2.3 meV at the elastic line.

Our sample was a single crystal of $BaFe_2As_2$ measuring 1mm x 2mm x 60 μm, grown using a self-flux method(89). Calculated optimal thickness for a transmission mode geometry for an incident energy of 21.657 keV was 55 μm. The crystal was oriented in transmission mode with (2, 2, 0) and (1, 1, 3) in the scattering plane. This alignment allows measurement of the phonons in the basal plane of the form $\mathbf{Q} = \mathbf{G}+\mathbf{q} = (\mathbf{H}-\mathbf{q}, \mathbf{K}+\mathbf{q})$, where $\mathbf{G} = (\mathbf{H}, \mathbf{K})$ is the reciprocal lattice vector of the Bragg peak in the $a-b$ plane, and $\mathbf{q}$ the inelastic momentum transfer. For temperature dependent studies, the crystal samples were mounted on copper holders with a small amount of varnish, and the copper holders were attached to the cold finger of a closed cycle cryostat sealed by a beryllium dome.

The beam size on sample was 50 μm by 350 μm. Only one analyzer-detector pair was used for these measurements, and an analyzer mask was used to limit Bragg contamination for low $\mathbf{q}$ measurements. The mask size was 4 cm by 4 cm at $\mathbf{q} \geq 0.07$, and 1 cm by 1 cm for all $\mathbf{q} < 0.07$. The Stokes and anti-Stokes profiles were measured in most cases, but at points where an anti-Stokes contribution to the phonon spectra was dynamically limited, a contribution from elastic scattering was ensured by transversely scanning the crystal space at zero energy transfer. All data were normalized to the incident monitor count, a low efficiency ion chamber.

For all temperatures, the phonon spectra were fit with Voigt profiles, employing the Whiting approximation to determine the width(255; 256). Phonon spectra were corrected for the Bose thermal population factors.

Fitted phonon peak widths are constrained to that of a phonon measured at $\mathbf{q} = 0.2$ at T = 130 K. Data for values of $\mathbf{q} > 0.07$ were fit with two phonon peaks and an elastic

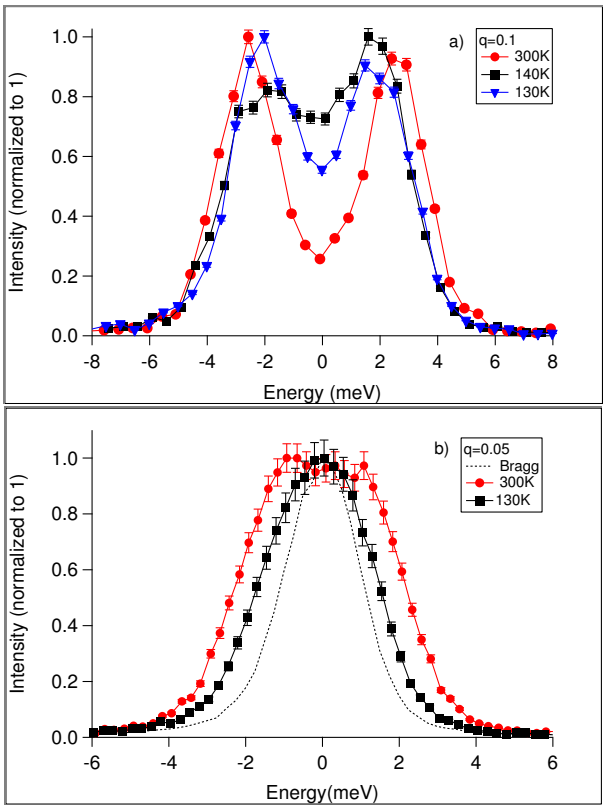

Figure 6.1: a) Comparison of 300 K, 140 K, and 130 K phonon spectra at $\mathbf{q} = 0.1$. b) Comparison of 300 K and 130 K phonon spectra at $\mathbf{q} = 0.05$. The dotted line shows the Bragg peak measurement at T=130 K, $\mathbf{Q}$=(2,2,0)$_O$. All spectra are Bose factor corrected and normalized to one. Errors are statistical errors propagated through Bose correction.

contribution. The phonon energy for $\mathbf{q} > 0.07$ is determined by the average of the fitted peak positions of the Stokes and anti-Stokes contributions.

Data for $\mathbf{q} \leq 0.07$ at temperatures below 300 K can not be resolved as distinct peaks, so the width of the observed peak is used as a proxy for the degree of softening (Fig. 6.1). The peak width is determined using a single Voigt profile.

The primary result of our investigation is the observation of a reduction in energy of the $[110]_O$ transverse acoustic phonon in the low $\mathbf{q}$ region, evident from the measured phonon spectra (Fig. 6.1). The data show this reduction is most pronounced at $\mathbf{q} = 0.1$, reaching a maximal amount near T = 140 K (Fig. 6.2). As the temperature is decreased, the phonon energy decreases, and then recovers, but not to the full energy observed at room temperature (Fig. 6.2) before decreasing again at low temperatures and low $\mathbf{q}$.

For data with $\mathbf{q} \leq 0.07$ the fitted width of the peak centered around zero energy transfer exhibits a linear behavior for 300 K (Fig. 6.3a), with the width of the spectra collapsing into the Bragg peak width for lower temperatures (Fig. 6.3b).

The lattice softening observed in the shear elastic measurements show a drop in the shear mode to a minimal values at T_S, and then a slight recovery to low temperatures(133; 257), or no recovery at all(258). This is in contrast to our observations here, as the phonon energy recovers most of the energy after softening, and the slope of the dispersion changes at low temperature.

The only mode investigated in this work was the low energy transverse acoustic mode, and there was only a local softening of the mode - the traditional linear dispersion is recovered by $\mathbf{q} = 0.20$ in all temperature cases (four temperature cases shown in Fig. 6.3). This result is not captured in published density functional theory (DFT) calculations reviewed in preparation of this manuscript.

The softening of the low energy transverse acoustic mode observed by IXS is expected in the context of soft mode transitions, as the decrease in energy of the long wavelength phonons is always seen in structural phase transitions of the type observed here(259). But it has a few possible interpretations for microscopic mechanism.

The first interpretation invokes Fermi surface nesting, which results in a regime of enhanced electron-phonon coupling. The Fermi surface structure of pnictides is well established to consist of hole pockets centered at the zone center, and electron pockets at the zone boundary(115; 111), with electron or hole doping serving to change the levels of the two pockets relative to one another(120). The softening of the TA phonon has a natural explanation in two-dimensional Fermi surface nesting giving rise to a Kohn anomaly, where strong quasiparticle excitations below $\mathbf{q} = 2\mathbf{k_F}$ result in enhanced electron-phonon coupling (164). Indeed we observe softening from the zone center to a maximal phonon softening below $\mathbf{q}$ = 0.1, which is consistent with the value of $2\mathbf{k_F}$ = 0.1 for the inner hole pocket in $BaFe_2As_2$(260).

In a work on $CaFe_2As_2$, a series of line broadenings is observed(139), though this is not used to draw the conclusion of Kohn anomalies, but may be related to the work

here. However, possible broadening of the phonons for the $BaFe_2As_2$ compound studied here is too small to be fully resolved by the current technique. Line broadenings of this type have been observed in studies of elemental superconductors, where the phonon anomalies were fully resolved only when using high resolution spin-echo neutron spectroscopy(261). In order to confirm the presence of phonon broadening and/or a Kohn anomaly in $BaFe_2As_2$, a careful analysis of the phonon lineshape using a higher energy resolution is required. Note also that there is some softening tendency at temperatures much below T_s. The $\mathbf{q}$ range of this low temperature softening is distinct from the softening at T_s; below $\mathbf{q} = 0.12$ at low temperatures, whereas softening is observed below $\mathbf{q} = 0.16$ near T_s. It appears that this softening has a different origin, and either one could be related to a Kohn anomaly.

A second interpretation is to consider the phonon softening in the context of coupling between the low energy acoustic mode and the orbital fluctuations. In this scenario, softening of the shear mode causes in-plane shifting of the iron atoms, impacting the interatomic distances along the FePn_4 layer. As these atoms shift their positions, the tetragonal orbital degeneracy between the d_{xz} and d_{yz} orbitals is broken, allowing the manifestation of magnetic order. While the orthorhombic structural distortion is small (of order 0.3%, with the change in the iron square lattice 2.8 Å on a side to a rectangle 2.79/2.81 Å), and several works show that there is a strong dependence of the electronic structure on small details of the lattice, in particular the height of the pnictogen atom above the iron plane(115; 122). Additionally, it has been shown that there is an enhancement of electron-boson coupling arising from orbital anisotropy(262), behavior which is in contrast to lower mean field values for the estimate of such couplings(103; 105). Further, the pnictide systems are very close to the Stoner criticality, where even a small lattice distortion can have a large consequence to the magnetism in the system(9).

The proposed mechanism indicates that other phonon modes may be involved in the structural transition via a similar softening behavior(9). Modes that directly influence the dynamics of the $FeAs_4$ tetrahedra are being examined. Further, a coupling of acoustic and

optical modes as is seen in other structural phase transitions(261) is not ruled out, and requires further examination.

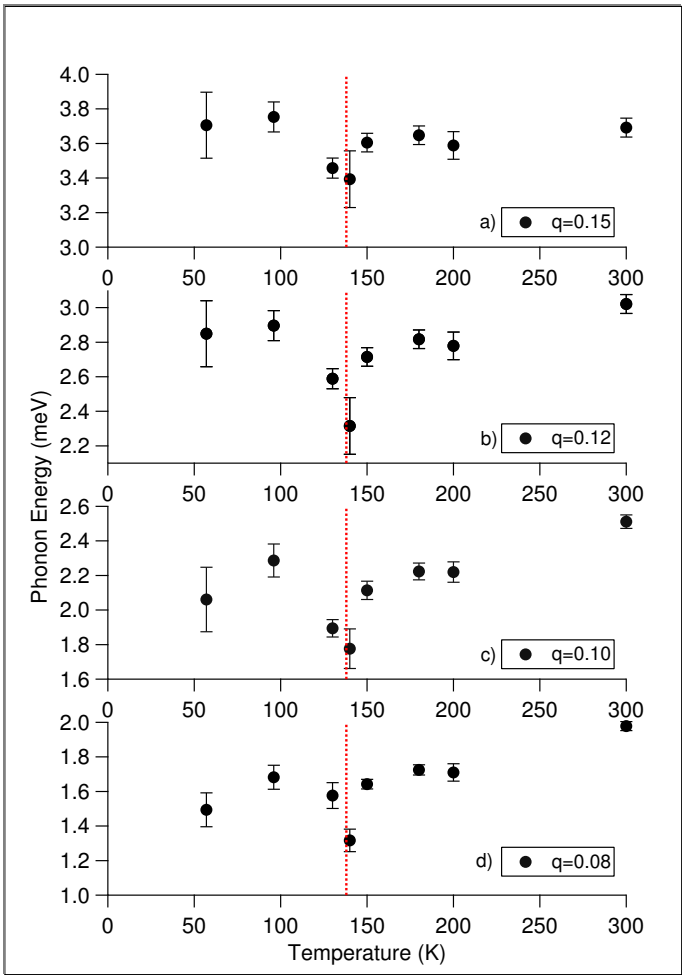

Figure 6.2: Energy of transverse acoustic phonon as a function of temperature for $\mathbf{Q} = (\mathbf{H} - \mathbf{q}, \mathbf{K} + \mathbf{q})$ for $H = K = 2$ and $\mathbf{q}$ = (a) 0.15, (b) 0.12, (c) 0.10, (d) 0.08 in orthorhombic reciprocal lattice units. Dotted line indicates T_S. Error bars are statistical errors propagated through Bose correction and peak averaging. Two softenings are observed, one at T_S and additional softening at low $\mathbf{q}$ at low temperature.

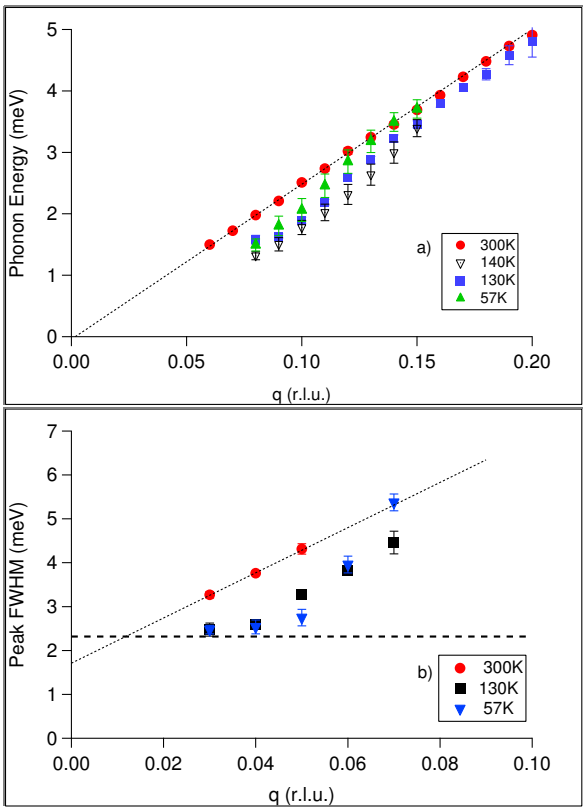

Figure 6.3: a) Dispersion of TA phonon at 300 K, 140 K, 130 K, and 57 K. Dotted line indicates a linear fit to the 300K data. b) Central peak width as a function of $\mathbf{q}$ for T=300 K, 130 K, and 57 K. Heavy dashed line at $E = 2.3$ meV indicates the width of the Bragg peak measured at $\mathbf{Q} = (2, 2, 0)$ T=130 K. Dotted line on 300 K data represents the fitted peak width. Error bars are statistical errors propagated through Bose correction and the curve fitting procedure.

6.3 Phonons in $Ba(Fe_{1-x}Co_x)_2As_2$

6.3.1 Phonon Softening

With the observation of phonon softening in $BaFe_2As_2$ described in 6.2 and commensurate observation of the softening of the shear elastic constant of $Ba(Fe_{0.92}Co_{0.08})_2As_2$, an experiment designed to characterize the softening of the low energy phonon modes as a function of doping was attempted.

Using IXS with an E_i of 21.5 keV, and energy resolution of 1.6 meV at BL35XU at the SPring-8 synchrotron, the dispersion of the transverse acoustic mode of $Ba(Fe_{0.92}Co_{0.08})_2As_2$ was studied as a function of temperature. Characteristic spectra are shown in Fig. 6.4a, and the energy of the mode at $\mathbf{q}$ = 0.11 is shown in Fig. 6.4b.

The softening of the mode is very slight, consistent with the small value of the softening observed in measurements of the shear elastic constant. One way the softening of the shear elastic constant has been explained is through the coupling of nematic fluctuations to the lattice. If this theory is true, one would expect that the shear mode to experience some softening. The ratio of elastic constant measurements at room temperature and low temperature measured by Resonant Ultrasound Spectroscopy (RUS) for the parent and the superconducting compound is $\frac{0.62-0.1}{0.62} = 0.84$, and for the superconducting $\frac{0.32-0.28}{0.32} = 0.13$, for a total factor of 6. Thus, we would naively expect the phonon softening to be a factor of 6 less for the superconducting compound from the parent. The maximal softening of the TA mode in $BaFe_2As_2$ is 0.8 meV, reached at $\mathbf{q}$ = 0.1. The maximal softening for $Ba(Fe_{0.92}Co_{0.08})_2As_2$ is 0.2 meV, a factor of 3.8.

The future for this work includes a repeat of this measurement, to confirm the presence of the softening. There is some doubt from the experiment, due to an issue with non-reproducibility at the beamline at the time of the measurement, which was traced to an error in the established setup. Repeating this measurement is crucial, as other phonon measurements in the literature do not explore the low-$\mathbf{q}$ region in this fashion, and may be missing some essential physics.

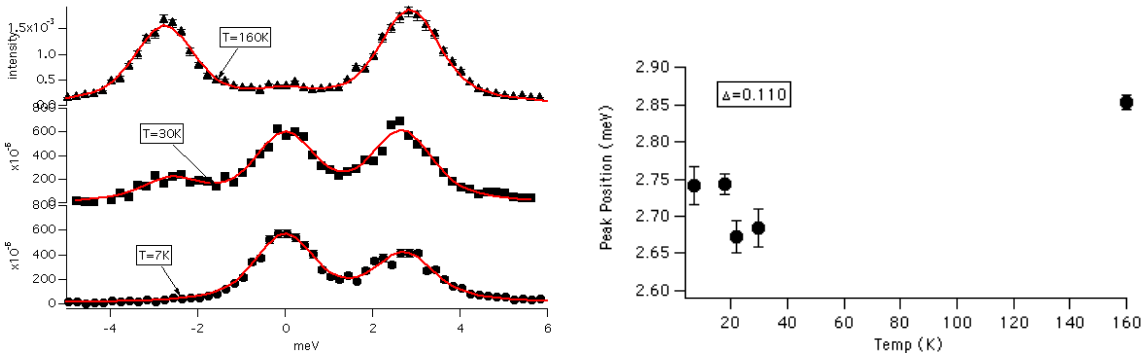

(a) Characteristic IXS spectra of the TA mode of $Ba(Fe_{0.92}Co_{0.08})_2As_2$ for three temperatures. The softening of the mode toward lower temperature is very slight.

(b) The temperature dependence of the **q** = 0.11 component of the TA mode of $Ba(Fe_{0.92}Co_{0.08})_2As_2$. A slight softening from high temperatures is observed, with a minimum at the superconducting critical temperature.

Figure 6.4: IXS spectra of TA mode of $Ba(Fe_{0.92}Co_{0.08})_2As_2$.

6.3.2 Phonon Broadening

Phonon line shapes provide clues about the level of electron-phonon interactions in a structure. A TOF INS experiment was carried out at the Cold Neutron Chopper Spectrometer (CNCS) at the Spallation Neutron Source (SNS) to study the shift in phonon energies as a function of temperature, but as a side offering provided a mechanism to measure the phonon line shape.

The sample was a single crystal array of $Ba(Fe_{0.96}Co_{0.04})_2As_2$ crystals, four in total, with a total mass of 4 g. The sample has T_N = 60 K, and T_c = 11 K. The A_{1g} mode of $Ba(Fe_{0.96}Co_{0.04})_2As_2$ was studied using an E_i of 25 and 37 meV, with energy resolution 1 and 1.5 meV at the elastic line. The phonon width changes (Fig. 6.6) as a function of temperature, to where it was completely resolution limited below T=10K, and broader beyond the resolution limit above T=10K. The broadening indicates that the phonon lifetime is longer in the superconducting state. The broadening of the phonon above T_c would indicate the presence of a stronger electron-phonon coupling in the statically ordered but non-superconducting state. The dispersion has a sharply different character approaching the zone boundary between the two temperatures (Fig. 6.5), indicating an enhanced interaction with spin-fluctuations above T_c.

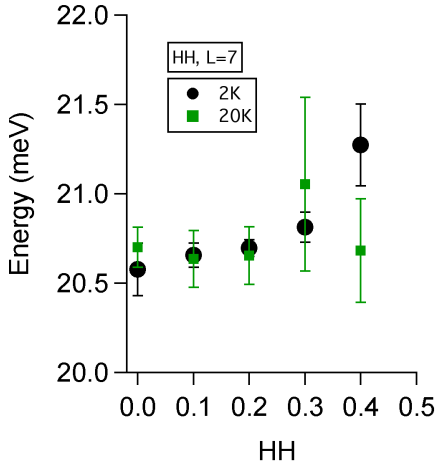

Figure 6.5: Dispersion of As-mode as a function of temperature for the $Ba(Fe_{0.96}Co_{0.04})_2As_2$ sample (T_N = 60 K, T_c = 11 K). There is a marked change in the dispersion toward the zone boundary above and below the T_c.

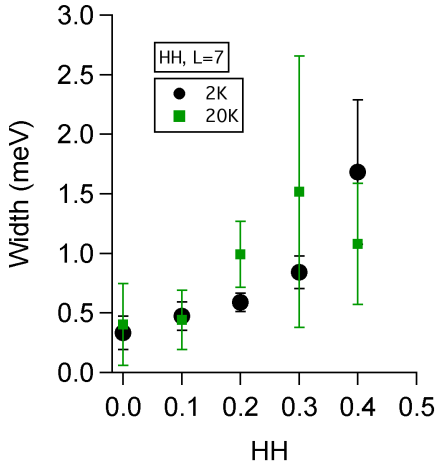

Figure 6.6: Phonon line width as a function of temperature for the $Ba(Fe_{0.96}Co_{0.04})_2As_2$ sample. The presence of a shorter phonon lifetime indicates stronger electron-phonon coupling in the non-superconducting, magnetically ordered state. The experimental resolution at the point of the measurement is 0.5 meV.

6.4 Phonons under pressure in $BaFe_2As_2$

Using pressure, one can probe the mechanical response of a system to the external stresses, and modifications in the dynamic behavior can give important information about the state of the system.

Using a diamond-anvil cell (DAC) to apply hydrostatic pressure, we studied the impact of pressure on the phonons in $BaFe_2As_2$ using IXS with an E_i = 23.7 keV on a sample approximately 60 μm thick. The pressure medium was He gas[2]. The sample was aligned to allow probing of in-plane modes. The pressure was checked using fluorescence from a ruby included in the sample vessel, and all measurements were conducted at room temperature. The primary result was the observation of a collapsed tetragonal (cT) phase when the pressure was raised above 9.5 GPa, consistent with observations of cT phases in $CaFe_2As_2$ and $SrFe_2As_2$. The lattice parameter changes are summarized in Tab. 6.1. The calculation of the lattice parameters in the pressurized state is performed using the change in the alignment reflections calculated *in-situ* after the change of pressure.

In changing the pressure on $BaFe_2As_2$ from ambient to 4 GPa, the phonons harden substantively, averaging a change of 2-3 meV, consistent with results from NRIXS(138). Changing from 4 to 10 GPa, and entering the cT phase, the impact is a slight softening of some phonons, substantial reduction the scattering intensity of the c-axis phonons and the splitting of high frequency in-plane phonon modes. The mode that is most impacted is a high frequency mode near 38 meV which appears to split into two peaks (Fig. 6.7b). The intensity in the As-As mode that appears near 25 meV at 4 GPa is substantially reduced, indicating a loss of activation of this mode, due to the collapse of the magnetic coupling (Fig. 6.7a). In plane modes at 10 meV and 15 meV soften slightly.

Addressing these results, we first note that the softening and hardening of the phonons with pressure can be understood with a changing force constant due to a changing lattice parameter. The softening of the in-plane modes in the 10 GPa phase is consistent with the reduction of the force constant caused by the increase in the a-axis

[2]The assumption that these conditions are truly hydrostatic is questionable.

Table 6.1: Lattice parameters of $BaFe_2As_2$ as function of pressure at ambient temperature. Ambient values taken from Rietveld refinement data(3), and lattice parameters under pressure calculated from alignment reflections in situ.

Parameter	Ambient	4GPa	10 GPa
a (Å)	3.9625(1)	3.945(2)	3.985(1)
c (Å)	13.0168(3)	12.232(1)	11.66(2)

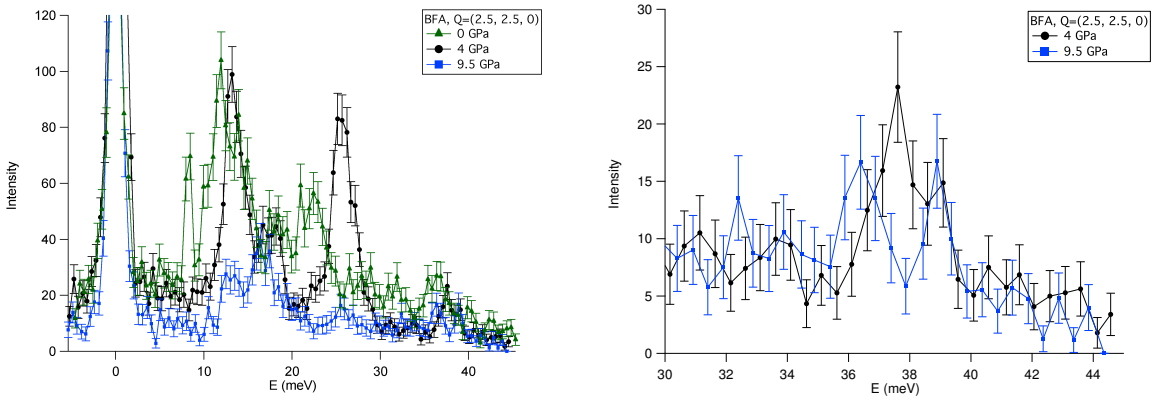

(a) Scattering intensity from IXS study on $BaFe_2As_2$ under pressure.

(b) Zoom of splitting of high frequency mode with pressure.

Figure 6.7: Response of phonons in $BaFe_2As_2$ to the application of pressure. A cT phase is reached when the pressure is raised above 9.5 GPa, resulting in the loss of scattering intensity and shifting of phonon energies, and the splitting of the high energy mode near 38 meV shown on right.

lattice constant. The reduction in scattering intensity of the c-axis modes precludes a precise determination of the energy, but the loss of scattering intensity shows the deactivation of these modes with pressure, consistent with the collapse of the c-axis.

Next we postulate on the effect of magnetism and the phonons. The cT phase is found to be consistent with the loss of all magnetic character in $CaFe_2As_2$(242; 132). in the ambient pressure calculation(106). The mode that appears to split at 38 meV in the 10 GPa measurement corresponds to a mode where the Fe-As atoms are shearing out of phase, modulating the volume of the Fe-As tetrahedron. If this mode splits, it reflects a lifting of a systemic degeneracy. This may represent a number of things, including a lowering of the system symmetry, or coupling of the magnetism and the lattice. The lowering of the

symmetry, i.e., from tetragonal to orthorhombic, would imply the presence of additional Bragg peaks, and additional splitting of phonon modes. Additional Bragg peaks were sought, but not observed. Mode splitting is only observed in the 38 meV mode, leading to the conclusion that the system remains tetragonal, but with a reduced c-axis constant. If there is a coupling between the lattice and the dynamic magnetism in the normal state driven by the Fe-As interaction, the quenching of this magnetic interaction will result in the resulting in the splitting of the high energy mode.

6.5 Phonon DOS of $BaFe_2(As_{1-x}P_x)_2$

A number of quantities of interest can be obtained from the study of the phonon density of states (DOS) of a system, in particular anharmonicity in phonon modes may be detected. The phonon density of states of $BaFe_2(As_{1-x}P_x)_2$ was measured using INS and Nuclear Resonant Inelastic X-ray Scattering (NRIXS) to study the impact on the phonon system as a function of doping.

Three samples of $BaFe_2(As_{1-x}P_x)_2$, with x = (0.2, 0.33, 0.7), were measured using the Wide Angular Range Chopper Spectrometer (ARCS) spectrometer, while an optimally doped $BaFe_2(As_{1-x}P_x)_2$ composed with isotopically enriched ^{57}Fe was studied at the XX instrument at the Advanced Photon Source (APS). These sample configurations represent an under doped compound with a magnetic and structural transition before entering the superconducting phase (x = 0.2); an optimally doped configuration with no static magnetism (x = 0.33); and an overdoped phase with no static magnetism or superconductivity (x = 0.7). Each sample was loaded into an extruded aluminum can inside of a helium glovebox, and a seal of indium wire was used to isolate the sample from the atmosphere. The samples were loaded into the bottom loading closed-cycle refrigerator (CCR) at ARCS, which has a base temperature of 4K. Sample quantities, critical and magnetic transition temperatures are presented in Tab. 6.2. The samples had previously been characterized by neutron diffraction measurements, so lattice parameters and impurity phases as a function of temperature are understood. All samples possess

some percentage impurity of Fe_2P, but the amount of impurity phase detected is less than 5% of the main phase in all cases, and amounts this low are unlikely to have substantial impact on the DOS measurements.

Table 6.2: Parameters of $BaFe_2(As_{1-x}P_x)_2$ samples used in phonon DOS studies.

Parameter	x = 0.2	x = 0.33	x = 0.7
Sample mass (g)	4.2	3.9	3.7
T_c (K)	4 K	30 K	–
T_N K)	120 K	–	–

From basic lattice theory, one would expect that the substitution of P for As results in the shifting of some phonon modes to a higher energy. The data analysis is complicated by the presence of an impurity in the x = 0.2 sample.

Debate about Fermi liquid theory, non-fermi liquid behavior in $BaFe_2(As_{1-x}P_x)_2$ persists. While no direct conclusions about this can be drawn from our DOS studies, the development of the phonon frequencies as a function of doping may shed some additional light on this topic.

Additionally, the superconducting resonance as a function of temperature was measured in the x = 0.2, 0.33 samples and found to be consistent with other superconducting samples, following the relationship $E_r = 5k_BT_c$.

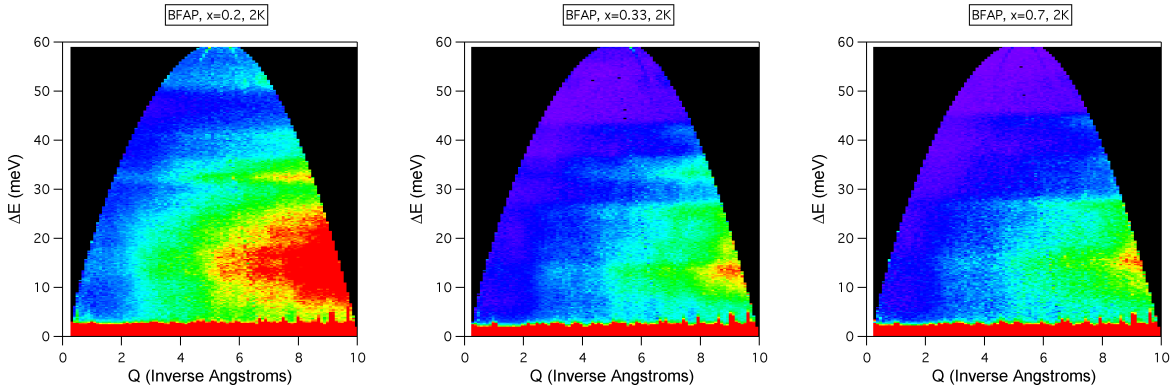

(a) x = 0.2, T = 2K **(b)** x = 0.33, T = 2K **(c)** x = 0.7, T = 2 K

(d) x = 0.2, T = 2 K **(e)** x = 0.33, T = 100 K **(f)** x = 0.7, T = 100 K

Figure 6.8: $S(\mathbf{Q}, \omega)$ for $BaFe_2(As_{1-x}P_x)_2$, x = 0.2, 0.33, 0.7 at 2 K and 100 K.

6.6 Spin excitations in $Ba(Fe_{1-x}Co_x)_2As_2$

Magnetic fluctuations as the source of electronic pairing is one of the schools of thought regarding the mechanism of high temperature superconductivity. INS measurements of a "resonant" spin excitation are offered as supporting evidence for this phenomena. The excitation is observed at the anti-ferromagnetic (AF) wave vector, the signal scales with T_c, and is enhanced with the onset of superconductivity in the cuprate materials. In the FeSC materials, the evidence of spin fluctuations is present above the T_c for different materials, but is enhanced below T_c.(55) The presence of the resonant excitation is used as evidence for the sign-changing $s_\pm$ state, where a strong resonance is indicative of inter-band scattering at the AF wave vector(263)

Inelastic neutron scattering measurements (264)were conducted on a three-crystal mosaic of $Ba(Fe_{0.92}Co_{0.08})_2As_2$ at the ARCS spectrometer at the SNS and the HB-3 TAS at High Flux Isotope Reactor (HFIR). Spin excitations had previously been observed by Lumsden(55), but this work extended the study to a higher energy range to permit a more direct comparison to the resonance phenomena seen in cuprates.

The sample was aligned to have the scattering plane in the (HHL) configuration. At HB-3, the incident energy was 30.5 meV, pyrolitic graphite (PG) filters were used to reduce higher order contamination, and PG monochromators and analyzers were used to prepare the beam. Final collimation produced a resolution of 3 meV at the elastic line. At ARCS, an incident energy of 60 meV was used, producing an elastic line resolution of 4 meV.

The primary result of this work is to show that the spin excitation spectrum is anisotropic in energy (figure 6.9a), which is distinct from the cuprate case where the peak is narrower and more symmetric in energy(265). Anisotropic spin excitation spectra are noted in Ni doped systems(266; 267). Additionally, residual scattering intensity persists to relatively high energies and also to relatively high temperatures (Fig. 6.10a), with evidence of the spin excitation signal still present at 200 K. The excitation has nearly zero

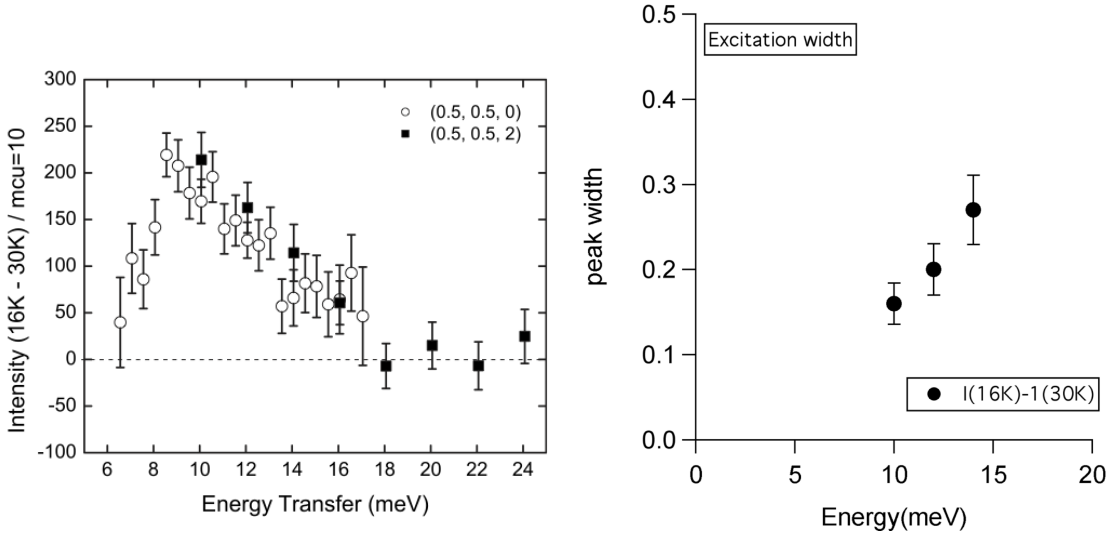

(a) Spin excitation spectrum for $Ba(Fe_{0.92}Co_{0.08})_2As_2$obtained on HB-3 at HFIR. Figure from(264)

(b) Width of spin excitation signal in the superconducting state of $Ba(Fe_{0.92}Co_{0.08})_2As_2$ as a function of energy. Fits are from pure gaussians, and error bars are 1 standard deviation.

Figure 6.9: Observations of anisotropy in the spin excitation spectra of $Ba(Fe_{0.92}Co_{0.08})_2As_2$.

dependence on L, indicating a strong two-dimensional character, with the line width increasing as a function of energy transfer (Fig. **??**), indicating a dispersive excitation.

The presence of the resonance and the established scaling relationship between the resonance energy and T_c shows that the physics of superconductivity of the cuprates and FeSC are related. Nevertheless, the resonance appears independent of superconducting gap symmetry, showing that the sign change of the gap is the crucial element to producing the resonance in a repulsive pairing scenario. The anisotropy of the spin excitation in energy remains unexplained in sufficient detail, but is used as a challenge to the assertion that the resonance is a singlet excitation of the Cooper pairs(266).

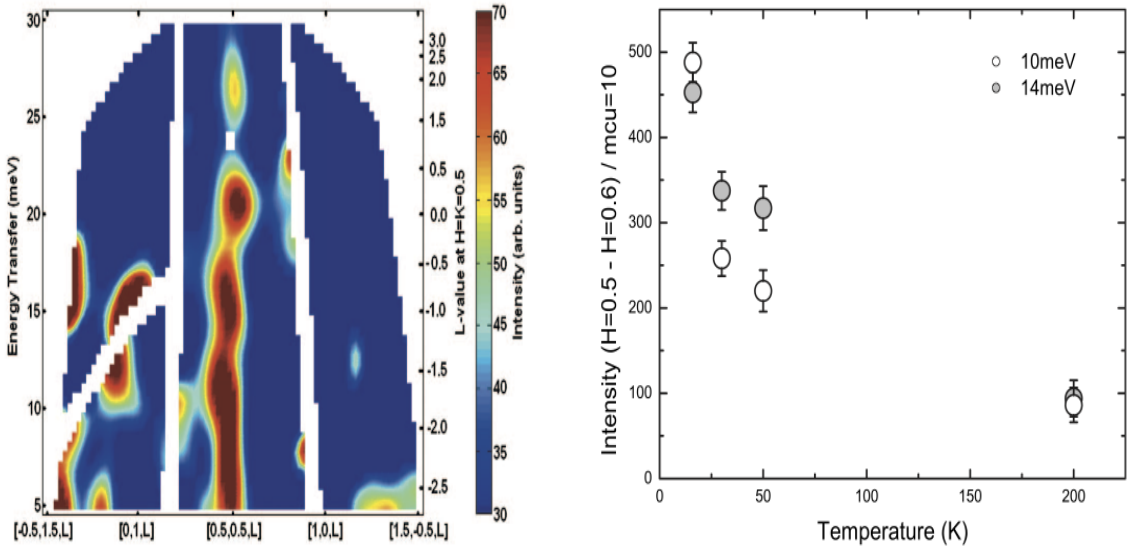

(a) Spin excitation for $Ba(Fe_{0.92}Co_{0.08})_2As_2$observed as a line of scattering intensity at $\mathbf{Q} = (0.5, 0.5, L)$. This scattering intensity persists to high energy, and also to high temperature. Figure from (264)

(b) Column intensity as a function of temperature. Substantial scattering intensity still observed at T=200K. Figure from (264)

Figure 6.10: Spin excitation scattering rod for $Ba(Fe_{0.92}Co_{0.08})_2As_2$.

6.7 Magnetic phonons in $BaFe_2As_2$

Magnetically coupled phonons are detectable through judicious use of polarized neutron scattering. One signal of strong spin-phonon coupling arises from an anomalous enhancement of magneto vibrational scattering. The topic of exotic electron-phonon coupling in superconductors has a long history. There are a number of theories in the cuprates discussing the presence of anomalous phonon behaviors including softening and renormalizations, as well as anomalous phonon effects as potential drivers for dynamic charge inhomogenities due to localized changes in the behaviors.

What is fundamental to the study presented here is the detection of a spin-phonon coupling that would contribute to a dynamic adjustment of the local magnetization. In such a scenario, a phonon results in a local modulation of the spin density, the result of which is the switching the spins dynamically from the minority to majority band. Such phenomena are detected in two ways - observation of an interference term between the

magnetism and phonon spectra in the polarized neutron analysis, and the mismatch of the dynamic and static form factors.

Due to the strong experimental and theoretical dependence of the static Fe-As distance on observables like the magnetic moment, natural candidates to look for evidence of spin-phonon coupling included any phonon mode that served to modulate the local environment of the iron atoms. Several phonons which are observable by Raman spectroscopy were determined theoretically and fit to measured phonon DOS using neutron scattering(110). Three of these phonons are also shown in dynamical mean-field theory (DMFT) to result in modulation of the electronic DOS at the Fermi surface, so are of particular interest. Using the results from *anapert*[3], we can also explore phonon modes using INS or IXS.

Although the evidence against electron-phonon coupling as a primary mechanism for the superconducting pairing in FeSC began to build early(103; 252; 104), so did evidence of phonon anomalies. Raman scattering observed the softening of high energy modes, INS studies on the phonon density of states (pDOS) present evidence of anomalous modes(139; 110), and also some softening behavior. Explicit inclusions of magnetism are required to reproduce phonon spectra measured with IXS(106) and INS(110; 157) In the light of the mounting evidence, the connection between phonons and magnetism was re-evaluated, and found to be strongly enhanced when specific coupling matrix values were evaluated, high enough that the role of unconventional electron-phonon coupling could not be neglected(105). Recent work with fast-pulsed probe spectroscopies show that the spin-density wave (SDW) order in $BaFe_2As_2$ can be melted, and then renormalizes with a frequency equal to that of the A_{1g} phonon mode(19). The A_{1g} mode depicts an oscillation of the As atoms against the Fe plane, and is predicted to modulate the spin density close to the Fermi surface(110)

Using the TOF INS ARCS spectrometer at the SNS we observe the signature of three signals that have substantial intensity dependence with temperature, shown in Fig. 6.12.

[3] *anapert* is a program that performs phonon eigenvector calculations based on DFT results, and was written by Rolf Heid at Karlsruhe Institute of Technology. *anapert* allows the user to calculate the phonon eigenvectors at arbitrary **Q**, and away from high symmetry positions.

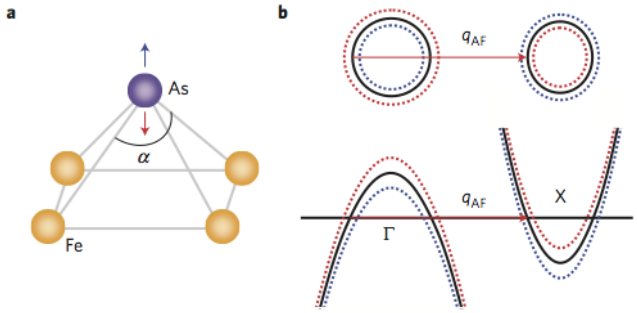

Figure 6.11: Demonstration of A_{1g} phonon mode, and the modulation of the electronic density close to the Fermi Surface in $BaFe_2As_2$. Figure from (19).

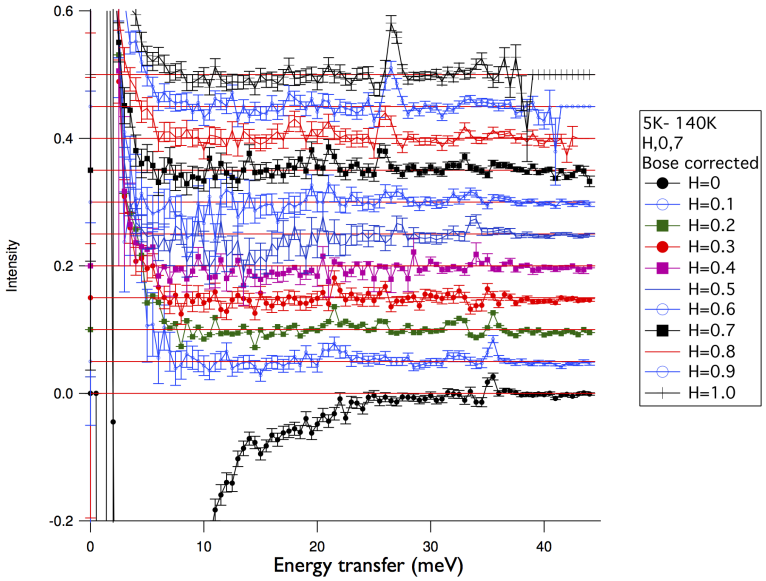

Figure 6.12: Dispersion plot depicting the temperature difference in scattering intensity for two of three phonon signals that are directly modulating the Fe-As tetrahedra in $BaFe_2As_2$. Each data series depicts a cut through the collected data set, and the error bars are one standard deviation. Data series are offset for clarity, with increasing central value of H. Data sets have been corrected for thermal population factors.

Using the polarized TAS instrument at the HFIR, and the Orphee reactor at the Laboratoire Léon Brillouin (LLB) we have investigated the presence of a weak magnetic signal in the $BaFe_2As_2$ (BFA) system. This signal is present at $\mathbf{Q} = (11L)$, an presents a weak L dependence.

To fully distinguish the presence of spin coupling to the phonons, full neutron polarization analysis is required[4] The first test used the ^{3}He polarized TAS at the NIST Center for Neutron Research (NIST), where we attempted to measure the magnetic component of the A_{1g} mode using a single crystal array of $Ba(Fe_{0.96}Co_{0.04})_2As_2$. The sample was a 4 crystal array, with crystals co-aligned in the HHL scattering plane. The crystals were affixed to aluminum plates, and the aluminum plates were embedded in an aluminum base piece painted with Gd_2O_3 to reduce the scattered neutron background. Temperature control was performed with a standard orange cryostat. BT-7 is a double focussing graphite monochromator with graphite analyzer, with no sapphire fast-neutron filter in the pile. ^{3}He polarization cells were set up on $\mathbf{k_i}$, and Mezei flippers were installed on $\mathbf{k_i}$ and $\mathbf{k_f}$, and a graphite filter was used on $\mathbf{k_f}$ to reduce the effect of the higher energy contamination from the incident beam. The polarization efficiency for the ^{3}He system is strongly time dependent, but the flipping ratio was maintained in the range of 10-20. Measurements were carried out with a fixed final $\mathbf{k_f}$. All measurements were conducted in the $\mathbf{Q}_\parallel$ $\mathbf{P}$ configuration, ensuring that all magnetic scattering is spin-flip scattering. The BT-7 setup includes a number of door detectors, which are useful in understanding spurious signals resulting from various elastic scattering processes. We were able to confirm the presence of one magnetic signal at $\mathbf{Q}$ = (117) near E = 21 meV (Fig. 6.13, when performing the magnetic analysis using a flipping ratio estimate of 8 and a background level of 10 counts per monitor unit. Both of these estimates are conservative. This point in $\mathbf{Q}$ space corresponds to the nuclear zone center, and magnetic zone boundary of $Ba(Fe_{0.96}Co_{0.04})_2As_2$, and to a phonon which shears the As and Fe atoms in opposition, as shown in Fig. 6.14. The phonon signal is very weak in the non-spin-flip (NSF) channel, which is unsurprising as it has a small structure factor. The presence

[4] See Sec. 4.5.

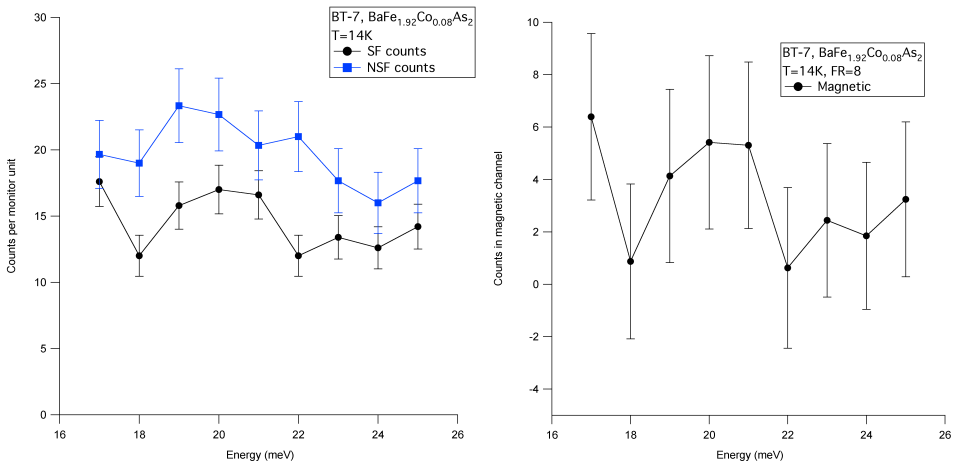

Figure 6.13: (left) SF and NSF signals from $Ba(Fe_{0.96}Co_{0.04})_2As_2$ at $\mathbf{Q}$ = (117) at 14K as measured at NIST. (right) calculated magnetic signal applying a flipping ratio of 8 and a background level of 10 counts per monitor unit.

of the spin-flip (SF) and magnetic signals therefore directly indicates the presence of an anomalous coupling between the spin and lattice channels that is only able to be detected via polarized analysis.

To confirm this result, inelastic polarized neutron studies were carried out on a single crystal array of $BaFe_2As_2$ at the Orphee reactor at the Laboratory Leon Brillouin. The sample is a 9 crystal array of $BaFe_2As_2$, aligned in the HHL scattering plane, total sample mass about 4 grams. The sample pieces are mounted aluminum posts with Al wire, and then the posts are mounted in Al blocks. The Al blocks are surrounded by boron nitride shielding pieces. The sample was aligned on the (008) and (110) Bragg peaks. The 2T1 setup at Orphee consists of a standard triple axis with double-focussing Heusler monochromator and analyzer, a beam monitor is placed on $\mathbf{k_i}$, and a Mezei flipper is installed on $\mathbf{k_f}$. All measurements are conducted with a fixed final $\mathbf{k_f}$=2.662Å^{-1}. The crystal is mounted in a displex capable of reaching 3K. The sample guide field is capable of providing neutron polarization field in the configurations H$\|$ $\mathbf{Q}$, H$\|$z, and H$\|$y.

Using longitudinal polarization analysis and the assumption of perfect polarization anti-parallel to the guide field, the field configurations and measured cross sections are

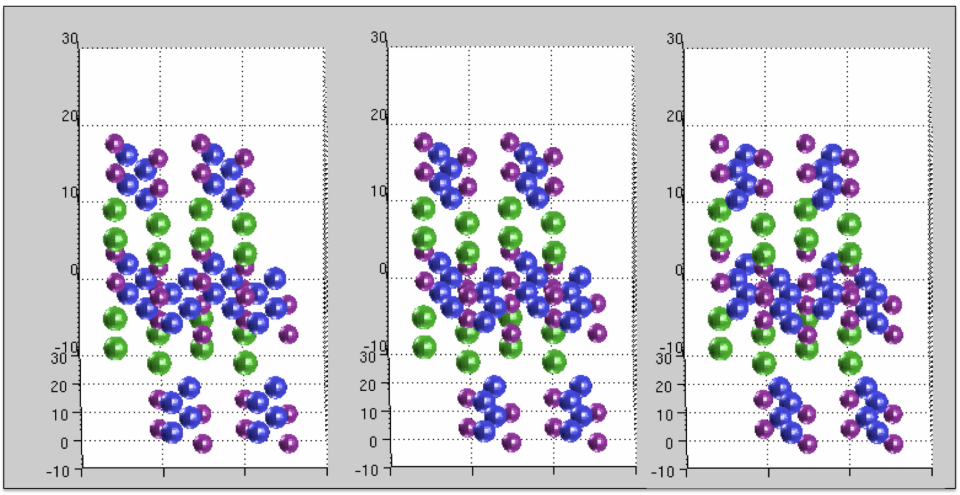

Figure 6.14: Representation of phonon activity at **Q** = (119), E = 25 meV, showing the shearing modulation of the Fe-atoms. (Fe - Blue, As - magenta, Ba - green.)

given in Tab. 6.3. In the table, the interference terms refer to scattering due from phonon-magnon interactions. These can create polarization along the direction of the magnetic interaction vector, but generally cancel when the phases differ by a factor of $\pi/2$.

Table 6.3: Field configurations and measured cross sections for spin flip and non-spin flip scattering from a perfectly polarized beam oriented anti-parallel to the guide field. Interpreted from (4).

Field State	Spin Flip	Non Spin Flip
H$\|\|$ **Q**	M_z + M_y	phonons (no magnetic scattering)
H$\|\|$z	M_z	phonons + M_y + interference terms
H$\|\|$y	M_y	phonons + M_z + interference terms

And using equations:

$$\textbf{Background} = I_x - I_y + I_z \tag{6.3}$$

$$\mathbf{M} = 2I_x - I_y - I_z \tag{6.4}$$

and

$$I_j = I_j^{SF} - \frac{I_j^{NSF} - BG}{FR} + BG \tag{6.5}$$

where j goes over the three applied field directions, and FR indicates the flipping ratio of the setup. BG indicates the estimated background subtraction, which the FR should not be applied.

Using the linear background estimate from Eq. 6.3 above, we analyze the scattering component from the three different field configurations, and these are shown in Fig. 6.15. The results are shown in Fig. 6.16 for the low temperature case, and in Fig. 6.17b above T_N. The corrected data clearly indicate the presence of a magnetic coupling above T_N for the 22 meV As mode that modulates the volume around the iron atoms. The presence of a clear magnetic signal at the low temperature is less obvious, but there is confirmation that the increased scattering intensity observed from the ARCS experiment has a SF component. To fully determine whether this intensity increase is magnetic in origin will require a more thorough polarization analysis.

In conclusion, the study confirmed the existence of a magnetic excitation near 22 meV at the 11L, L=odd position, corresponding to the phonon mode where the As atoms are transiting perpendicular to the iron plane. The effect of this mode is to distort the local iron environment directly, enabling a dynamic switching between the high and low spin state. The signal has temperature dependence, and there is also confirmation of a previous ARCS study showing an increase in scattering intensity for a mode at 25 meV at low temperatures.

The future for this work will include mapping the dispersion of these anomalous features, and determining the extent of the coupling among different modes in the system. To do so will require a substantial amount of polarized neutron beam time at a facility capable of performing full polarization analysis, and proposals are in preparation for continuation at the Institut Laue-Langevin (ILL) and NIST.

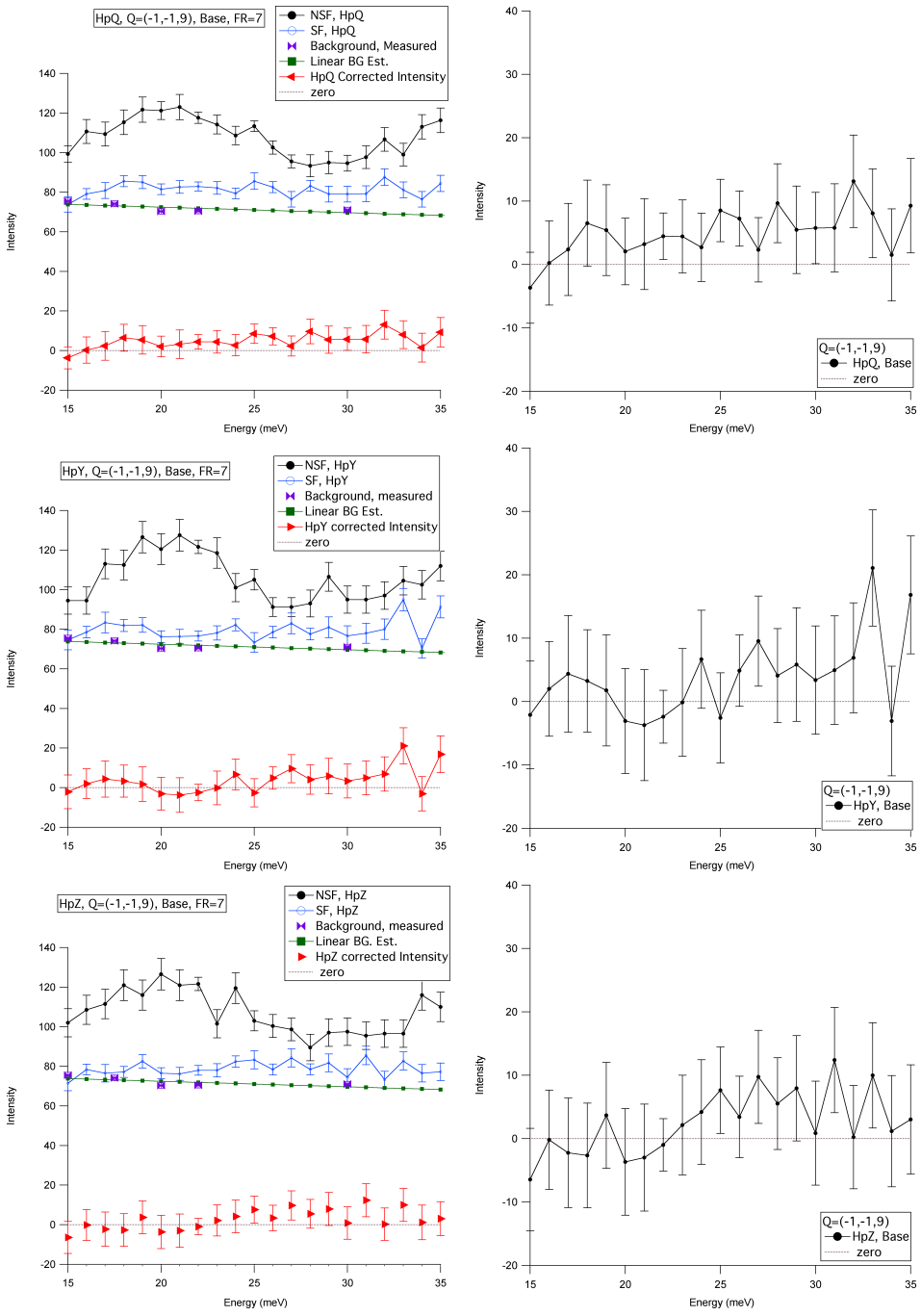

Figure 6.15: NSF, SF, background, background estimate, and corrected intensity for the three field configurations at base temperature, zoom of the corrected intensity for each configuration shown on the right..

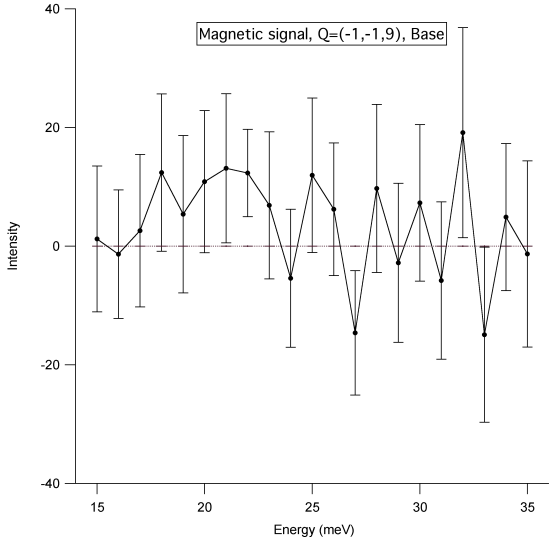

Figure 6.16: Calculated magnetic intensity at base temperature using Eq. 6.4.

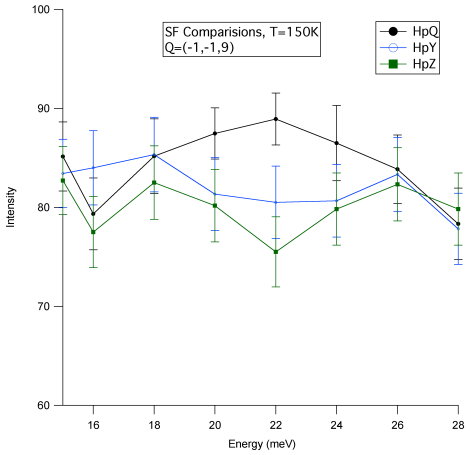

(a) SF intensities for the three field configurations at T=150K.

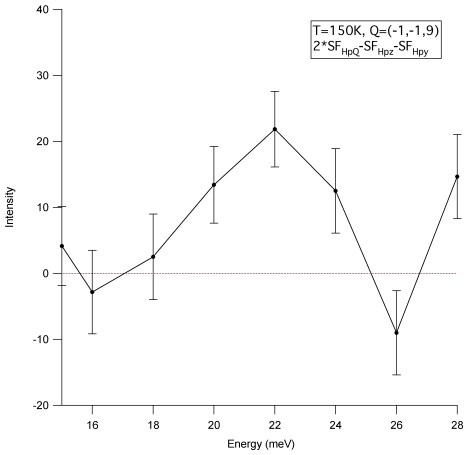

(b) Magnetic signal near 22 meV, showing the direct presence of a magnetic contribution to this volume-modulating mode above the T_N of the sample

Figure 6.17: SF scattering intensities at T = 150K on $BaFe_2As_2$.

6.8 Synthesis of Dynamic Studies

There are a number of experimental results presented here, so we now establish a collective interpretation of these data. The interplay of the lattice and the magnetism are demonstrated clearly in the IXS and INS studies. In the IXS study on the softening of the TA mode, we observe a range of softening for the mode, making the magneto structural transition in this system distinct from a canonical "soft-mode" transitions, the hallmark of which is sharp softening at a specific wave vector, and a non-recovery of the phonon mode below the transition temperature. We clearly demonstrate that the phonon mode goes soft at a range of $\mathbf{q}$ values, and then recovers most of its energy. The link to magnetism in this case is that the local lattice distortions demonstrated in Sec. 5.2 directly represent a coupling between the spin and lattice. Above T_N, the system exhibits broad quasi-elastic signals at the AF wave vector in inelastic neutron studies (12; 268), indicating retention of strong in-plane medium-range spin order in the paramagnetic state in spite of a loss of inter-planar correlation. As the temperature of the system is lowered toward T_N, the spatial range of spin correlation increases and the fluctuation frequency is lowered. Thus spin correlation couples with the lattice, resulting in local distortion. This effect is represented by the softening of the transverse phonon mode near T_N. (21) The softening occurs over a finite range of inelastic momentum transfers $\mathbf{q}$, so the correlation length of the fluctuations never diverges as in the standard second-order phase transition. Indeed this transition has first-order signature (269; 268; 270), suggesting the local nature of the transition. Further, the resulting increase in the magneto-structural transition temperature by compressing the orthorhombic b-axis(153) is naturally explained by this model. Applying uniaxial strain to the b-axis induces partial de-twinning, resulting in the increase in the volume fraction of the twin with one sense and the intensity of the magnetic diffraction peak.

Additionally, systematic differences in the magnetic moment from neutron diffraction are observed in $BaFe_2As_2$ as a function of cooling temperature. As observed in Ref. (143), the level of hysteresis in the magnetic transition is highly sample dependent, in addition

to depending on the rate of cooling used in the experiment(152; 271; 269), highlighting the instability of the formation of the magnetic structure in these systems.

Fundamentally, there are two energy scales of consideration in the pnictides, a point of growing consensus, as demonstrated by Liu(267), Yin(114) and colleagues. The low energy component, under 100 meV is sensitive to doping of carriers, while the high energy component is insensitive to doping. The high energy spectra look identical, leading to the calculation of nearly equivalent total moments(267). The major implication of these findings is that the high energy component is set for the system, so small details of the low energy spectra dominate the particular state selection, and these low energy details are dominated by the local structural variations of the system. The local atomic disorder demonstrated in $BaFe_2As_2$ and doped systems shows that local disorder in the FeSC is intrinsic to these systems, driving the low energy physics in these materials.

7 Conclusions

The main theme of this work is that the lattice complexity gives rise to unexpected effects. At the most fundamental level, high temperature superconductivity (HTSC) in the iron-based superconductors (FeSC) represents one entry into a unique class of complex materials: those that experience a fundamental structural frustration that results from the interplay between lattice and spin degrees of freedom available to the system.

This work presents a number of findings. The first is that the local structural distortions in $BaFe_2As_2$ present a mechanism by which the static magnetic moment may be modified. The structural distortion also shows that the magneto-structural phase transition in $BaFe_2As_2$ is localized and driven by a coupling between the spin and the lattice. The softening of the phonon modes in the parent compounds occurs in such a way as to prevent the development of infinite correlations at the structural phase transition, and this behavior begins well above the transition temperature. The second is that local structural distortions in doped FeSC show evidence of structural distortion up to room temperature, casting doubt on the long range stability of the structure against fluctuations in the paramagnetic state. The third is that the coupling between the lattice and magnetic degrees of freedom can be seen in the phonon spectrum, through the splitting of high frequency phonon modes in the collapsed tetragonal (cT) state, and the direct observation of spin-phonon coupling through inelastic neutron scattering.

Several of these observations are new. The field of high temperature superconductivity is dominated by the study of magnetic phenomena and purely electronic effects, so

lattice effects have been relegated to something of an unimportant detail. However, this work shows that the subtle effects of the structure are central to the nature of several questions in high temperature superconductors. In these systems, the local distortions result in local environments that are distinct in the solid, resulting in distorted and in extreme cases ambiguous descriptors for the long range behavior. These effects, arising from a strong coupling between the lattice, spin, and possibly orbital degrees of freedom are pronounced, and are likely to contribute to the source of the superconducting pairing in these materials.

An important distinction to draw here is the impact of the long range and local behavior on a system. The long range, average behavior determines the high energy phenomena in materials, giving us our understanding of the band structure and the fermiology. Local structure determines the low energy physics, which sets the scale for effects that are observable to humans, such as electron-phonon coupling and superconductivity. Superconductivity is a low energy phenomena, and its solution will be determined by exploration of low energy physics, and local structure and phonon anomalies are crucial to understanding these points.

The results presented require the consideration of static atomic displacements in structures and systems, and the explicit inclusion of spin-lattice effects into further work in this area. In the immediate term, the future for this work is to continue to investigate the extent of structural disorder on FeSC, and relate these discoveries to findings that are made possible by other experimental techniques, i.e. ultrafast laser spectroscopy and tunneling microscopies, which already have shown substantial evidence of local inhomogeneities and complex lattice effects. Another promising avenue is to relate these effects to other types of HTSC, namely cuprate materials. The frontier for this work is to create tractable computational models to capture these effects, to harness these results to aid the development effort to build predictive models of high temperature superconductivity.

Bibliography

[1] G. Shirane, S. A. Shapiro, and J. M. Tranquada, *Neutron Scattering with a Triple Axis Spectrometer* (Cambridge, 2003). xi, 47, 53, 73, 74, 75, 76, 79, 80

[2] W. Sturhahn, J. Phys.: Condens Mat **16**, S497 (2004). xi, 94

[3] M. Rotter, M. Tegel, D. Johrendt, I. Schellenberg, W. Hermes, and R. Pöttgen, Physical Review B **78**, 020503(R) (2008). xii, 18, 20, 29, 112, 135

[4] J. Schweizer, *Neutron Scattering from Magnetic Materials* (Elsevier, 2006), chap. Polarized Neutrons and Polarization Analysis. xii, 146

[5] C. Buzea and K. Robbie, Superconducting Science and Technology **18**, R1 (2005). xiii, 4, 5

[6] E. Dagotto, Reviews of Modern Physics **66**, 763 (1994). xiii, 15

[7] J. Paglione and R. L. Greene, Nat Physics **6**, 645 (2010). xiii, 5, 17, 23, 25

[8] I. I. Mazin, Nature **464**, 183 (2010). xiii, 12, 18

[9] T. Egami, B. V. Fine, D. J. Singh, D. Parshall, C. de la Cruz, and P. Dai, Physica C **470**, S294 (2010). xiv, 21, 25, 27, 30, 99, 127

[10] C. de la Cruz, W. Z. Hu, S. Li, Q. Huang, J. W. Lynn, M. A. Green, G. F. Chen, N. L. Wang, H. A. Mook, Q. Si, and P. Dai, Physical Review Letters **104**, 017204 (2010). xiv, 21, 27, 117

[11] Y. Mizuguchi, Y. Hara, K. Deguchi, S. Tsuda, T. Yamaguchi, K. Takeda, H. Kotegawa, H. Tou, and Y. Takano, Supercond Sci Tech **23**, 054013 (2010). xiv, 21, 27

[12] L. Harriger, H. Luo, M. Liu, C. Frost, J. Hu, M. Norman, and P. Dai, Physical Review B **84**, 054544 (2011). xiv, 23, 24, 30, 44, 107, 117, 150

[13] M. Da Luz, J. Neumeier, R. Bollinger, A. S. Sefat, M. A. McGuire, R. Jin, B. C. Sales, and D. Mandrus, Physical Review B **79**, 214505 (2009). xiv, 25, 26

[14] D. Pratt, W. Tian, A. Kreyssig, J. Zarestky, S. Nandi, N. Ni, S. Bud'ko, P. Canfield, A. Goldman, and R. McQueeney, Physical Review Letters **103**, 87001 (2009). xiv, 20, 29

[15] D. Pratt, M. Kim, A. Kreyssig, Y. Lee, G. Tucker, A. Thaler, W. Tian, J. Zarestky, S. Bud'ko, P. Canfield, B. Harmon, A. Goldman, and R. J. McQueeney, Physical Review Letters **106**, 257001 (2011). xiv, 29

[16] Council for the central laboratory of the research councils - future access to neutron sources: A strategy for the UK, 2005. xv, 51

[17] M. Lumsden, Private communication, 2009. xvi, 73

[18] E. Burkel, *Inelastic Scattering of X-rays with Very High Energy Resolution* (Springer-Verlag, 1991), chap. X-ray Sources. xvi, 90

[19] K. W. Kim, A. Pashkin, H. Schäfer, M. Beyer, M. Porer, T. Wolf, C. Bernhard, J. Demsar, R. Huber, and A. Leitenstorfer, Nature Materials **11**, 1 (2012). xxi, 43, 142, 143

[20] D. van Delft and P. Kes, Physics Today **63**, 38 (2010). 1

[21] J. L. Niedziela, D. Parshall, K. A. Lokshin, A. S. Sefat, A. Alatas, and T. Egami, Physical Review B **84**, 224305 (2011). 3, 107, 150

[22] H. K. Onnes, Leiden Comm. **120b** (1911). 4

[23] H. K. Onnes, Investigations into the properties of substances at low temperatures, which have led, amongst other things, to the preparation of liquid helium, in *Nobel Lectures*, Elsevier Publishing Company, Amsterdam, 1967. 4

[24] J. Bardeen, L. Cooper, and J. Schrieffer, Physical Review **106**, 162 (1957). 4, 11

[25] L. Cooper, Physical Review **104**, 1189 (1956). 4, 10

[26] A. J. Leggett, *Quantum Liquids: Bose Condensation and Cooper Pairing in Condensed-Matter Systems* (Oxford University Press, 2007). 4, 10, 13

[27] A. B. Migdal, Soviet Physics JETP **7**, 996 (1958). 5, 10

[28] G. M. Eliashberg, Soviet Physics JETP **11**, 696 (1960). 5, 11, 12

[29] D. J. Scalapino, J. R. Schrieffer, and J. W. Wilkins, Physical Review **148**, 147 (1966). 5, 11

[30] W. L. McMillan, Physical Review **167**, 331 (1968). 5, 11

[31] J. Bednorz and K. Müller, Zeitschrift für Physik B Condensed Matter **64**, 189 (1986). 5, 12

[32] K. A. Müller and J. G. Bednorz, Science **237**, 1133 (1987). 5

[33] J. G. Bednorz and K. A. Müller, Reviews of Modern Physics **60**, 585 (1988). 5

[34] J. Nagamatsu, N. Nakagawa, T. Muranaka, Y. Zenitani, and J. Akimitsu, Nature **410**, 63 (2001). 5

[35] Y. Kamihara, T. Watanabe, M. Hirano, and H. Hosono, J. Am. Chem. Soc **130**, 3296 (2008). 5, 17

[36] F. Steglich, J. Aarts, C. Bredl, W. Lieke, D. Meschede, W. Franz, and H. Schäfer, Physical Review Letters **43**, 1892 (1979). 5

[37] D. Jerome, A. Mazaud, M. Ribault, and K. Bechgaard, J. Physique Lett. **41**, 95 (1980). 5

[38] A. F. Hebard, M. J. Rosseinsky, R. C. Haddon, D. W. Murphy, S. H. Glarum, T. T. M. Palstra, A. P. Ramirez, and A. R. Kortan, Nature **350**, 600 (1991). 5

[39] Y. Maeno, H. Hashimoto, K. Yoshida, S. Nishizaki, T. Fujita, J. Bednorz, and F. Lichtenberg, Nature **372**, 532 (1994). 5

[40] M. J. Tinkham, *Introduction to Superconductivity* (Dover Press, 1964). 7, 10

[41] J. C. Phillips, Physical Review Letters **10**, 96 (1963). 7

[42] L. P. Gor'kov, Soviet Physics JETP **9**, 1364 (1959). 9

[43] H. Fröhlich, Physical Review **79**, 845 (1950). 9

[44] H. Frölich, Proceedings of the Royal Society (London) **A215**, 291 (1952). 9

[45] E. Maxwell, Physical Review **78**, 477 (1950). 9

[46] C. Reynolds, B. Serin, W. Wright, and L. Nesbitt, Physical Review **78**, 487 (1950). 9

[47] J. E. Hirsch, **cond-mat.supr-con** (2011), 1108.3835. 9

[48] J. E. Hirsch, Physica Scripta **84**, 045705 (2011). 9

[49] J. R. Schrieffer, *Theory of Superconductivity* (Westview Press, 1999). 10

[50] P. B. Allen and R. C. Dynes, Physical Review B **12**, 905 (1975). 11

[51] A. Q. R. Baron, H. Uchiyama, Y. Tanaka, S. Tsutsui, D. Ishikawa, S. Lee, R. Heid, K. P. Bohnen, S. Tajima, and T. Ishikawa, Physical Review Letters **92**, 197004 (2004). 11

[52] J. Rossat-Mignod, L. Regnault, C. Vettier, P. Bourges, P. Burlet, J. Bossy, J. Y. Henry, and G. Lapertot, Physica C **185-189**, 86 (1991). 11

[53] S. D. Wilson, P. Dai, S. Li, S. Chi, H. J. Kang, and J. W. Lynn, Nature **442**, 59 (2006). 11

[54] A. Christianson, E. Goremychkin, R. Osborn, S. Rosenkranz, M. Lumsden, C. Malliakas, I. Todorov, H. Claus, D. Chung, and M. Kanatzidis, Nature **456**, 930 (2008). 11

[55] M. D. Lumsden, A. Christianson, D. Parshall, M. B. Stone, S. E. Nagler, G. J. MacDougall, H. A. Mook, K. A. Lokshin, T. Egami, D. L. Abernathy, E. A. Goremychkin, R. Osborn, M. A. McGuire, A. S. Sefat, R. Jin, B. C. Sales, and D. Mandrus, Physical Review Letters **102**, 107005 (2009). 11, 139

[56] G. Yu, Y. Li, E. M. Motoyama, and M. Greven, Nature Physics **5**, 873 (2009). 11, 19

[57] A. Alexandrov and V. Kabanov, Physical Review Letters **106**, 136403 (2011). 12

[58] W. Kohn and J. M. Luttinger, Physical Review Letters **15**, 524 (1965). 12

[59] W. E. Pickett, Reviews of Modern Physics **61**, 433 (1989). 12

[60] H. Alloul, J. Bobroff, and M. Gabay, Reviews of Modern Physics **81**, 45 (2009). 13, 20

[61] N. Mott, Reviews of Modern Physics **40**, 677 (1968). 13

[62] A. Schilling, M. Cantoni, J. D. Guo, and H. R. Ott, Nature **363**, 56 (1993). 13

[63] C. W. Chu, L. Gao, F. Chen, Z. J. Huang, R. L. Meng, and Y. Y. Xue, Nature **365**, 323 (1993). 13

[64] A. J. Leggett, Nature Physics **2**, 134 (2006). 13

[65] N. Mannella, W. L. Yang, X. J. Zhou, H. Zheng, J. F. Mitchell, J. Zaanen, T. P. Devereaux, N. Nagaosa, Z. Hussain, and Z. X. Shen, Nature **438**, 474 (2005). 13

[66] M. Uchida, K. Ishizaka, P. Hansmann, Y. Kaneko, Y. Ishida, X. Yang, R. Kumai, A. Toschi, Y. Onose, R. Arita, K. Held, O. Andersen, S. Shin, and Y. Tokura, Physical Review Letters **106** (2011). 13

[67] P. W. Anderson, *The Theory of High Temperature Superconductivity* (Princeton Series in Physics, 1997). 13, 19

[68] M. Aranda, Advanced Materials **6**, 905 (1994). 14

[69] M. Laguës, X. M. Xie, H. Tebbji, X. Z. Xu, V. Mairet, C. Hatterer, C. F. Beuran, and C. Deville-Cavellin, Science **262**, 1850 (1993). 14

[70] P. W. Anderson, *The Theory of High Temperature Superconductivity in the High-Tc Cuprates* (Princeton University Press, 1997). 14

[71] B. Toby, T. Egami, J. Jorgensen, and M. Subramanian, Physical Review Letters **64**, 2414 (1990). 14

[72] T. Egami, B. Toby, S. Billinge, H. Rosenfeld, J. Jorgensen, D. Hinks, B. Dabrowski, M. Subramanian, M. Crawford, and W. Farneth, Physica C: Superconductivity and its applications **185**, 867 (1991). 16

[73] T. Sendyka, W. Dmowski, T. Egami, N. Seiji, H. Yamauchi, and S. Tanaka, Physical Review B **51**, 6747 (1995). 16

[74] T. Egami, T. Sendyka, W. Dmowski, D. Louca, H. Yamauchi, S. Tanaka, and M. Arai, Physica C: Superconductivity and its applications **235**, 1229 (1994). 16

[75] S. J. L. Billinge and T. Egami, Physical Review B **47**, 14386 (1993). 16

[76] M. Gutmann, S. Billinge, E. Brosha, and G. Kwei, Physica C: Superconductivity and its applications **341**, 2143 (2000). 16

[77] S. Billinge, T. Egami, D. Richards, D. Hinks, B. Dabrowski, J. Jorgensen, and K. Volin, Physica C: Superconductivity and its applications **179**, 279 (1991). 16

[78] B. Toby, W. Dmowski, T. Egami, J. Jorgensen, M. Subramanian, J. Gopalakrishnan, A. Sleight, and J. Parise, Physica C: Superconductivity and its applications **162**, 101 (1989). 16

[79] C. Kittel, *Introduction to Solid State Physics - Eighth Edition* (John Wiley and Sons, 2005). 17

[80] Y. Kamihara, H. Hiramatsu, M. Hirano, R. Kawamura, H. Yanagi, T. Kamiya, and H. Hosono, Journal of the American Chemical Society **128** (2006). 17

[81] T. Watanabe, H. Yanagi, T. Kamiya, Y. Kamihara, H. Hiramatsu, M. Hirano, and H. Hosono, Inorganic Chemistry **46**, 7719 (2007). 17

[82] Z.-A. Ren, J. Yang, W. Lu, W. Yi, X.-L. Shen, Z.-C. Li, G.-C. Che, X.-L. Dong, L.-L. Sun, F. Zhou, and Z.-X. Zhao, Europhysics Letters **82**, 57002 (2008). 17

[83] X. Zhu, F. Han, G. Mu, P. Cheng, B. Shen, and H. H. Wen, Physical Review B **79**, 220512 (2009). 18

[84] C. de la Cruz, Q. Huang, J. W. Lynn, J. Li, W. R. Ii, J. L. Zarestky, H. A. Mook, G. F. Chen, J. L. Luo, N. L. Wang, and P. Dai, Nature **453**, 899 (2008). 18, 20, 23

[85] M. Wang, C. Fang, D.-X. Yao, G. Tan, L. W. Harriger, Y. Song, T. Neterton, C. Zhang, M. Wang, M. B. Stone, W. Tian, J. Hu, and P. Dai, Nature Communications **2**, 580 (2011). 18

[86] H. Takahashi, K. Igawa, K. Arii, Y. Kamihara, M. Hirano, and H. Hosono, Nature **453**, 376 (2008). 18, 29

[87] X. H. Chen, T. Wu, G. Wu, R. H. Liu, H. Chen, and D. F. Fang, Nature **453**, 761 (2008). 18, 29

[88] M. Rotter, M. Tegel, and D. Johrendt, Physical Review Letters **101**, 107006 (2008). 18, 29

[89] A. S. Sefat, R. Jin, M. A. McGuire, B. C. Sales, D. J. Singh, and D. Mandrus, Physical Review Letters **101**, 117004 (2008). 18, 29, 124

[90] A. S. Sefat, A. Huq, M. A. McGuire, R. Jin, B. C. Sales, D. Mandrus, L. M. D. Cranswick, P. W. Stephens, and K. H. Stone, Physical Review B **78**, 104505 (2008). 18, 29

[91] P. Alireza, Y. Ko, J. Gillett, C. Petrone, J. Cole, G. Lonzarich, and S. E. Sebastian, Journal of Physics, Condensed Matter **21**, 012208 (2009). 18, 27

[92] Z. Ren, Q. Tao, S. Jiang, C. Feng, C. Wang, J. Dai, G. Cao, and Z. Xu, Physical Review Letters **102**, 137002 (2009). 18, 20, 29

[93] S. Jiang, H. Xing, G. Xuan, C. Wang, Z. Ren, C. Feng, J. Dai, Z. Xu, and G. Gao, Journal of Physics: Condensed Matter **21**, 382203 (2009). 18, 29

[94] M. Kim, R. Fernandes, A. Kreyssig, J. Kim, A. Thaler, S. Bud'ko, P. Canfield, R. McQueeney, J. Schmalian, and A. Goldman, Physical Review B **83** (2011). 20

[95] Y. Laplace, J. Bobroff, F. Rullier-Albenque, D. Colson, and A. Forget, Physical Review B **80**, 140501 (2009). 20, 43

[96] A. S. Sefat, D. J. Singh, L. VanBebber, Y. Mozharivskyj, M. A. McGuire, R. Jin, B. C. Sales, V. Keppens, and D. Mandrus, Physical Review B **79**, 224524 (2009). 20

[97] C. C. Tsuei and J. R. Kirtley, Reviews of Modern Physics **72**, 969 (2000). 20

[98] C. C. Tsuei and J. R. Kirtley, Physical Review Letters **85**, 182 (2000). 20

[99] C. C. Tsuei, J. R. Kirtley, G. Hammerl, J. Mannhart, H. Raffy, and Z. Z. Li, Physical Review Letters **93**, 187004 (2004). 20

[100] I. I. Mazin, D. J. Singh, M. D. Johannes, and M. H. Du, Physical Review Letters **101**, 057003 (2008). 20

[101] H. Kontani and S. Onari, Physical Review Letters **104**, 157001 (2010). 20

[102] C.-H. Lee, A. Iyo, H. Eisaki, H. Kito, M. T. Fernandez-Diaz, T. Ito, K. Kihou, H. Matsuhata, M. Braden, and K. Yamada, Journal of the Physical Society of Japan **77**, 083704 (2008). 21, 27

[103] L. Boeri, O. V. Dolgov, and A. A. Golubov, Physical Review Letters **101**, 026403 (2008). 21, 24, 123, 127, 142

[104] L. Boeri, O. V. Dolgov, and A. A. Golubov, Physica C **469**, 628 (2009). 21, 123, 142

[105] L. Boeri, M. Calandra, I. I. Mazin, O. V. Dolgov, and F. Mauri, Physical Review B **82**, 020506(R) (2010). 21, 22, 24, 123, 127, 142

[106] D. Reznik, K. Lokshin, D. C. Mitchell, D. Parshall, W. Dmowski, D. Lamago, R. Heid, K.-P. Bohnen, A. S. Sefat, M. A. McGuire, B. C. Sales, D. G. Mandrus, A. Subedi, D. J. Singh, A. Alatas, M. H. Upton, A. H. Said, A. Cunsolo, Y. Shvyd'ko, and T. Egami, Physical Review B **80**, 214534 (2009). 21, 22, 30, 99, 135, 142

[107] S. Y. Savrasov, Physical Review B **54**, 016470 (1996). 22

[108] O. Roesch and O. Gunnarsson, Physical Review B **70**, 224518 (2004). 22

[109] K. P. Bohnen, R. Heid, and M. Krauss, Europhysics Letters **64**, 104 (2003). 22

[110] M. Zbiri, H. Schober, M. Johnson, S. Rols, R. Mittal, Y. Su, M. Rotter, and D. Johrendt, Physical Review B **79**, 064511 (2009). 22, 24, 27, 30, 142

[111] Y. Wang, S. L. Shang, X. D. Hui, L. Q. Chen, and Z. K. Liu, Applied Physics Letters **97**, 022504 (2010). 22, 126

[112] F. Rullier-Albenque, D. Colson, A. Forget, and H. Alloul, Physical Review Letters **103**, 057001 (2009). 22

[113] L. Yang, Y. Zhang, H. Ou, J. Zhao, D. Shen, B. Zhou, J. Wei, F. Chen, M. Xu, C. He, Y. Chen, Z. D. Wang, X. F. Wang, T. Wu, G. Wu, X. H. Chen, M. Arita, K. Shimada, M. Taniguchi, Z. Y. Lu, T. Xiang, and D. L. Feng, Physical Review Letters **102**, 107002 (2009). 22

[114] Z. P. Yin, S. Lebègue, M. J. Han, B. P. Neal, S. Y. Savrasov, and W. E. Pickett, Physical Review Letters **101**, 047001 (2008). 22, 151

[115] D. J. Singh, Physical Review B **78**, 094511 (2008). 22, 23, 29, 126, 127

[116] F. Bondino, E. Magnano, M. Malvestuto, F. Parmigiani, M. A. McGuire, A. S. Sefat, B. C. Sales, R. Jin, D. Mandrus, E. W. Plummer, D. J. Singh, and N. Mannella, Physical Review Letters **101**, 267001 (2008). 22, 23

[117] I. I. Mazin and M. D. Johannes, Nature Physics **5**, 141 (2008). 22

[118] S. A. J. Kimber, A. Kreyssig, Y.-Z. Zhang, H. O. Jeschke, R. Valent Iacute, F. Yokaichiya, E. Colombier, J. Yan, T. C. Hansen, T. Chatterji, R. J. McQueeney, P. C. Canfield, A. I. Goldman, and D. N. Argyriou, Nature Materials **8**, 471 (2009). 22, 27

[119] C. Liu, G. D. Samolyuk, Y. Lee, N. Ni, T. Kondo, A. Santander-Syro, S. Bud'ko, J. McChesney, E. Rotenberg, and T. Valla, Physical Review Letters **101**, 177005 (2008). 23

[120] B. C. Sales, M. A. McGuire, A. S. Sefat, and D. G. Mandrus, Physica C **470**, 304 (2010). 23, 126

[121] D. Mandrus, A. S. Sefat, M. A. McGuire, and B. C. Sales, Chemistry of Materials **22**, 715 (2010). 23, 28, 29

[122] D. J. Singh, Physica C **469**, 418 (2009). 23, 127

[123] M. Daghofer, Q. Luo, R. Yu, D. Yao, A. Moreo, and E. Dagotto, Physical Review B **81**, 180514(R) (2010). 23

[124] T. Yildirim, Physica C **469**, 425 (2009). 23, 25

[125] K. Kubo and P. Thalmeier, Journal of the Physical Society of Japan **78**, 3704 (2009). 23

[126] J. Zhao, D. T. Adroja, D.-X. Yao, R. Bewley, S. Li, X. F. Wang, G. Wu, X. H. Chen, J. Hu, and P. Dai, Nat Physics **5**, 555 (2009). 24, 44

[127] P. Piekarz and T. Egami, Physical Review B **72**, 054530 (2005). 25

[128] T. Egami, P. Piekarz, and J. Chung, Physica C: Superconductivity **408**, 292 (2004). 25

[129] T. Egami, J. Chung, R. J. McQueeney, M. Yethiraj, H. A. Mook, C. Frost, Y. Petrov, F. Dogan, Y. Inamura, M. Arai, S. Tajima, and Y. Endoh, Physica B **316-317**, 62 (2002). 25

[130] F. Yndurain and J. Soler, Physical Review B **79**, 134506 (2009). 25

[131] H. Eschrig, arXiv **cond-mat.supr-con**, 0804.0186 (2008). 25

[132] T. Yildirim, Physical Review Letters **102**, 037003 (2009). 25, 30, 99, 135

[133] R. M. Fernandes, L. H. VanBebber, S. Bhattacharya, P. Chandra, V. Keppens, D. G. Mandrus, M. A. McGuire, B. C. Sales, A. S. Sefat, and J. Schmalian, Physical Review Letters **105**, 157003 (2010). 25, 126

[134] F. Hardy, P. Adelmann, T. Wolf, H. v. Löhneysen, and C. Meingast, Physical Review Letters **102**, 187004 (2009). 26, 98

[135] E. D. Bauer, J. D. Thompson, J. L. Sarrao, L. A. Morales, F. Wastin, J. Rebizant, J. C. Griveau, P. Javorsky, P. Boulet, E. Colineau, G. H. Lander, and G. R. Stewart, Physical Review Letters **93**, 147005 (2004). 26

[136] J. Müller, M. Lang, F. Steglich, J. Schlueter, A. Kini, and T. Sasaki, Physical Review B **65**, 144521 (2002). 26

[137] J. Nyhus, U. Thisted, N. Kikugawa, T. Suzuki, and K. Fossheim, Physica C **369**, 273 (2002). 26

[138] O. Delaire, M. S. Lucas, A. M. d. Santos, A. Subedi, A. S. Sefat, M. A. McGuire, L. Mauger, J. A. Muñoz, C. A. Tulk, Y. Xiao, M. Somayazulu, J. Y. Zhao, W. Sturhahn, E. E. Alp, D. J. Singh, B. C. Sales, D. Mandrus, and T. Egami, Physical Review B **81**, 094504 (2010). 26, 27, 93, 134

[139] R. Mittal, L. Pintschovius, D. Lamago, R. Heid, K. P. Bohnen, D. Reznik, S. Chaplot, Y. Su, N. Kumar, S. Dhar, A. Thamizhavel, and T. Brueckel, Physical Review Letters **102**, 217001 (2009). 27, 126, 142

[140] R. Mittal, S. Rols, M. Zbiri, Y. Su, H. Schober, S. Chaplot, M. Johnson, M. Tegel, T. Chatterji, S. Matsuishi, H. Hosono, D. Johrendt, and T. Brueckel, Physical Review B **79**, 144516 (2009). 27

[141] V. Cvetkovic and Z. Tesanovic, Physical Review B **80**, 24512 (2009). 27

[142] T. Yamazaki, N. Takeshita, R. Kobayashi, H. Fukazawa, Y. Kohori, K. Kihou, C. Lee, H. Kito, A. Iyo, and H. Eisaki, Physical Review B **81**, 224511 (2010). 27

[143] M. Lumsden and A. Christianson, Journal of Physics: Condensed Matter **22**, 23203 (2010). 27, 150

[144] E. Wiesenmayer, H. Luetkens, G. Pascua, R. Khasanov, A. Amato, H. Potts, B. Banusch, H.-H. Klauss, and D. Johrendt, Physical Review Letters **107**, 237001 (2011). 27, 110

[145] B. Joseph, V. Zinth, M. Brunelli, B. Maroni, D. Johrendt, and L. Malavasi, Journal of Physics: Condensed Matter **23**, 112202 (2011). 27, 117

[146] D. Louca, K. Horigane, A. Llobet, R. Arita, S. Ji, N. Katayama, S. Konbu, K. Nakamura, T.-Y. Koo, P. Tong, and K. Yamada, Physical Review B **81**, 134524 (2010). 28, 110

[147] J. M. Caron, J. R. Neilson, D. C. Miller, A. Llobet, and T. M. McQueen, Physical Review B **85**, 180405(R) (2012). 28, 110

[148] T. M. McQueen, A. Williams, P. Stephens, J. Tao, Y. Zhu, V. Ksenofontov, F. Casper, C. Felser, and R. Cava, Physical Review Letters **103**, 057002 (2009). 28, 110, 117

[149] S. Saha, N. Butch, K. Kirshenbaum, J. Paglione, and P. Zavalij, Physical Review Letters **103**, 037005 (2009). 28

[150] L. Malavasi, G. Artioli, H. Kim, B. Maroni, B. Joseph, Y. Ren, T. Proffen, and S. Billinge, Journal of Physics: Condensed Matter **23**, 272201 (2011). 28, 110, 117, 118

[151] S. Margadonna, Y. Takabayashi, M. Mcdonald, M. Brunelli, G. Wu, R. Liu, X. Chen, and K. Prassides, Physical Review B **79**, 014503 (2009). 28, 110

[152] Q. Huang, Y. Qiu, W. Bao, M. A. Green, J. W. Lynn, Y. C. Gasparovic, T. Wu, G. Wu, and X. H. Chen, Physical Review Letters **101**, 257003 (2008). 29, 151

[153] C. Dhital, Z. Yamani, W. Tian, J. Zeretsky, A. Sefat, Z. Wang, R. Birgeneau, and S. D. Wilson, Physical Review Letters **108**, 087001 (2012). 29, 108, 150

[154] A. Christianson, M. D. Lumsden, S. Nagler, G. J. MacDougall, M. A. McGuire, A. S. Sefat, R. Jin, B. C. Sales, and D. Mandrus, Physical Review Letters **103**, 087002 (2009). 29

[155] C.-H. Lee, K. Kihou, K. Horigane, S. Tsutsui, T. Fukuda, H. Eisaki, A. Iyo, H. Yamaguchi, A. Q. R. Baron, M. Braden, and K. Yamada, Journal of the Physical Society of Japan **79**, 014714 (2010). 30

[156] T. Fukuda, A. Q. R. Baron, S. Shamoto, M. Ishikado, H. Nakamura, M. Machida, H. Uchiyama, S. Tsutsui, and A. Iyo, Journal of the Physical Society of Japan **77**, 103715 (2008). 30

[157] M. Zbiri, R. Mittal, S. Rols, Y. Su, Y. Xiao, H. Schober, S. Chaplot, M. Johnson, T. Chatterji, Y. Inoue, S. Matsuishi, H. Hosono, and T. Brueckel, Journal of Physics: Condensed Matter **22**, 315701 (2010). 30, 142

[158] A. Cano, M. Civelli, I. Eremin, and I. Paul, Physical Review B **82**, 020408 (2010). 30

[159] I. Paul, Physical Review Letters , 047004 (2011). 30

[160] K. Deguchi, Y. Mizuguchi, Y. Kawasaki, T. Ozaki, S. Tsuda, T. Yamaguchi, and Y. Takano, Superconducting Science and Technology **24**, 055008 (2011). 31, 119, 120

[161] N. W. Ashcrohft and N. D. Mermin, *Solid State Physics* (Saunders College Publishing, 1976). 34, 36

[162] D. C. Wallace, *Thermodynamics of Crystals* (Dover Publications, 1998). 34

[163] P. Brüesch, *Phonons: Theory and Experiment I - Lattice Dynamics and Models of Interatomic Forces* (Springer Series in Solid-State Sciences, Springer-Verlag, 1982). 34, 35

[164] W. Kohn, Physical Review Letters **2**, 393 (1959). 35, 126

[165] P. Mohn, Itinerant Electron Systems: Magnetism (Ferromagnetism), in *Encyclopedia of Physics*, edited by R. G. Lerner and G. L. Trigg, p. 4316, Wiley-VCH, 2007. 36

[166] P. Mohn, *Magnetism in the Solid State* (Springer Series in the Solid State Sciences, 2006). 36

[167] Mattis, *Theory of Magnetism Made Simple* (World Scientific, 2006). 38

[168] P. Mohn, *Magnetism in the Solid State* (Springer Series in the Solid State Sciences, 2002), chap. Itinerant Electrons at 0K. 38

[169] P. Mohn, *Magnetism in the Solid State* (Springer Series in the Solid State Sciences, 2002), chap. Itinerant Electrons at T > 0: A Historical Survey. 38

[170] T. Moriya, Physical Review Letters **24**, 1433 (1970). 39

[171] P. Mohn, *Magnetism in the Solid State* (Springer Series in the Solid State Sciences, 2002), chap. Spin Fluctuations. 40

[172] R. L. Melcher, Encyclopedia of Physics , 554 (1981). 41, 42, 43

[173] B. S. Chandrasekhar, Magnetostriction, in *Encyclopedia of Physics*, edited by R. G. Lerner and G. L. Trigg, pp. 565–566, Addison-Wesley, 1981. 41, 42

[174] W. Miller, C. W. Smith, D. S. Mackenzie, and K. E. Evans, J Mater Sci **44**, 5441 (2009). 42

[175] P. Brown, I. Jassim, K. Neumann, and K. R. A. Ziebeck, Physica B **161**, 9 (1989). 42

[176] D. E. Parshall, *Spin-Lattice Coupling in the Iron-Pnictide High-Temperature Superconductors*, PhD thesis, University of Tennessee Knoxville, 2010. 43

[177] S. W. Lovesey, *Theory of Neutron Scattering from Condensed Matter: Volume 2* (Clarendon Press, 1984). 43, 47, 74

[178] P. R. C. Kent, *Techniques and Applications of Quantum Monte Carlo*, PhD thesis, Robinsons College, University of Cambridge, 1999. 45

[179] G. Alvarez, M. Mayr, A. Moreo, and E. Dagotto, Physical Review B **71**, 014514 (2005). 46

[180] E. Dagotto, T. Hotta, and A. Moreo, Physics Reports **344**, 1 (2001). 46

[181] G. L. Squires, *Introduction to the Theory of Thermal Neutron Scattering* (Dover, 1996). 47, 51, 74

[182] R. Pynn, Neutron Scattering - A Primer, 2002. 47

[183] E. Burkel, *Inelastic Scattering of X-rays with very high energy resolution*, Springer Tracts in Modern Physics Vol. 125 (Springer-Verlag, Berlin/Heidelberg, 1991). 47

[184] E. Burkel, Reports on Progress in Physics **63**, 171 (2000). 47, 92

[185] B. E. Warren, *X-ray Diffraction* (Dover Press, 1990). 48

[186] A. Guinier, *X-ray Diffraction In Crystals, Imperfect Crystals, and Amorphous Bodies* (Dover Press, 1994). 48

[187] V. K. Pecharsky and P. Y. Zavalij, *Fundamentals of Powder Diffraction and Structural Characterization of Materials* (Springer, 2009). 48

[188] E. Wollan and C. Shull, Physical Review **73**, 830 (1948). 49

[189] B. Brockhouse and A. Stewart, Physical Review **100**, 756 (1955). 50

[190] D. J. Griffths, *Introduction to Quantum Mechanics* (Benjamin Cummings, 1994). 51

[191] E. Merzbacher, *Quantum Mechanics* (Wiley, 1997). 52

[192] Neutron scattering lengths and cross sections, http://www.ncnr.nist.gov/resources/n-lengths/, 2012. 53

[193] National nuclear data center, http://www.nndc.bnl.gov/, 2012. 53

[194] P. J. Brown, Magnetic form factors, in *International Tables for Crystallography, Volume C*, pp. 454–461, International Union of Crystallography, 2006. 54

[195] H. M. Rietveld, Journal of Applied Crystallography **2**, 65 (1969). 61, 64, 65, 95, 111

[196] A. C. Larson and R. B. von Dreele, LANL Reports **LAUR 86-748** (2000). 63, 96, 102, 111

[197] National Institutes of Science and Technology, Diffraction metrology and standards, http://www.nist.gov/mml/ceramics/structure_determination/diffraction-metrology.cfm, 2012. 63

[198] T. Egami and S. J. L. Billinge, *Underneath the Bragg Peaks* (Pergammon Press, 2003). 63, 64, 65, 110, 111

[199] W. Dmowksi, B. Toby, T. Egami, M. Subramanian, J. Gopalakrishnan, and A. Sleight, Physical Review Letters **61**, 2608 (1988). 64, 65

[200] T. Proffen and K. Page, Zeitschrift für Kristallographie **219**, 130 (2004). 64

[201] T. Proffen, S. J. L. Billinge, T. Egami, and D. Louca, Zeitschrift für Kristallographie **218**, 132 (2003). 65

[202] B. Warren and N. Gingrich, Physical Review **46**, 368 (1934). 65

[203] S. J. L. Billinge, Zeitschrift für Kristallographie **219**, 117 (2004). 65

[204] B. H. Toby and S. J. L. Billinge, Acta Crystallographica A: Foundations of Crystallography **60**, 315 (2004). 67

[205] B. H. Toby and T. Egami, Acta Crystallographica **48**, 336 (1992). 67

[206] D. L. Abernathy, Notiziario Neutroni E Luce Di Sincrotrone **13**, 1 (2008). 69

[207] G. Ehlers, A. A. Podlesnyak, J. L. Niedziela, E. B. Iverson, and P. E. Sokol, Review of Scientific Instruments **82**, 085108 (2011). 69

[208] R. M. Moon, T. Riste, and W. Koehler, Physical Review **181**, 920 (1969). 72, 76, 78

[209] M. J. Cooper and R. Nathans, Acta Crystallographica **23**, 357 (1967). 73, 91

[210] S. T. Bramwell, Neutron Scattering and Highly Frustrated Magnetism, in *Introduction to Frustrated Magnetism Springer Series in Solid-State Sciences*, Springer, 2011. 74

[211] W. Marshall and R. Lowde, Reports on Progress in Physics **31**, 705 (1968). 74

[212] J. Schweizer, Polarized neutron scattering, in *Neutron Scattering from Magnetic Materials*, edited by T. Chatterji, Elsevier, 2006. 74, 79, 80

[213] P. J. Brown, Magnetic Form Factors, http://www.ill.eu/sites/ccsl/ffacts/ffacts.html, 2012. 76

[214] W. C. Chen, T. R. Gentile, T. G. Walker, and E. Babcock, Physical Review A **75**, 013416 (2007). 79

[215] W. C. Chen, R. Erwin, J. W. M. Iii, S. Watson, C. B. Fu, T. R. Gentile, J. A. Borchers, J. W. Lynn, and G. L. Jones, Physica B **404**, 2663 (2009). 79

[216] G. J. Russell, E. J. Pitcher, G. Muhrer, F. Mezei, and P. D. Ferguson, Overview of Spallation Neutron Source Physics, in *Fundamental Physics with Pulsed Neutron Beams*, pp. 19–47, World Scientific, 2000. 81, 82, 83, 84

[217] E. Fermi, J. Marshall, and L. Marshall, Physical Review **72**, 193 (1947). 83

[218] G. F. Knoll, *Radiation Detection and Measurement* (John Wiley and Sons, 2000). 86

[219] M. L. Crow, J. P. Hodges, and R. G. Cooper, Nuclear Instruments and Methods A **529**, 287 (2004). 86

[220] C. Wang, L. Clonts, R. Cooper, M. Crow, Y. Diawara, E. Ellis, L. Funk, B. Hannan, J. Hodges, and J. Richards, Nuclear Science Symposium and Medical Imaging Conference (NSS/MIC), 2011 IEEE , 4877 (2011). 86, 87

[221] K. Kuroda and I. Manuilov, Nuclear Instruments and Methods **A430**, 311 (1999). 87

[222] D. Green, *The Physics of Particle Detectors*Cambridge Monographs on Particle Physics, Nuclear Physics, and Cosmology (Cambridge, 2000). 87

[223] H. Nojiri, S. Yoshii, M. Yasui, K. Okada, M. Matsuda, J. Jung, T. Kimura, L. Santodonato, G. Granroth, K. Ross, J. Carlo, and B. Gaulin, Physical Review Letters **106**, 237202 (2011). 88

[224] K. An, H. D. Skorpenske, A. D. Stoica, D. Ma, X.-L. Wang, and E. Cakmak, Metall and Mat Trans A **42**, 95 (2010). 88

[225] E. Burkel, *Inelastic Scattering of X-rays with Very High Energy Resolution* (Springer-Verlag, 1991). 90

[226] B. Dormer, E. Burkel, T. Illini, and J. Peisl, Z. Phys. B. Condensed Matter **69**, 179 (1987). 90

[227] C. Masciovecchio, U. Bergmann, M. Krisch, G. Ruocco, F. Sette, and R. Verbeni, Nuclear Instruments and Methods in Physics Research Section B: Beam Interactions with Materials and Atoms **111**, 181 (1996). 90

[228] C. Masciovecchio, U. Bergmann, M. Krisch, G. Ruocco, F. Sette, and R. Verbeni, Nuclear Instruments and Methods in Physics Research Section B: Beam Interactions with Materials and Atoms **117**, 339 (1996). 90

[229] A. Q. R. Baron, Y. Tanaka, S. Goto, K. Takeshita, T. Matsushita, and T. Ishikawa, Journal of Physics and Chemistry of Solids **61**, 461 (2000). 90

[230] A. Q. R. Baron, Y. Tanaka, D. Miwa, D. Ishikawa, T. Mochizuki, K. Takeshita, S. Goto, T. Matsushita, H. Kimura, F. Yamamoto, and T. Ishikawa, Nuclear Instruments and Methods A **467**, 627 (2001). 90

[231] A. Q. R. Baron, The Journal of the Spectroscopic Society of Japan **58**, 205 (2009). 91

[232] A. Chumakov, A. Q. R. Baron, R. Rüffer, H. Grünsteudel, H. Grünsteudel, and A. Meyer, Physical Review Letters **76**, 4258 (1996). 92

[233] T. Proffen, T. Egami, S. J. L. Billinge, A. Cheetham, D. Louca, and J. Parise, Applied Physics A: Materials Science & Processing **74**, s163 (2002). 96, 102, 111

[234] A. Huq, J. P. Hodges, O. Gourdon, and L. Heroux, Zeitschrift für Kristallographie Proceedings **2011**, 127 (2011). 96, 111

[235] A. Catalano, R. J. Arnott, and A. Wold, Journal of Solid State Chemistry **7**, 262 (1973). 96, 111

[236] H. Fuji, S. Komura, T. Takeda, T. Okamoto, Y. Ito, and J. Akimitsu, Journal of the Physical Society of Japan **46**, 1616 (1979). 96, 111

[237] A. Koumina, M. Bacmann, D. Fruchart, J. L. Soubeyroux, P. Wolfers, J. Tobola, S. Kaprzyk, S. Niziol, M. Mesnaoui, and R. Zach, Ann. Chim. Sci. Mat. **23**, 177 (1998). 96, 111

[238] M. Rotter, C. Hieke, and D. Johrendt, Physical Review B **82**, 014513 (2010). 96

[239] V. Zinth and D. Johrendt, European Physics Letters **98**, 57010 (2012). 98

[240] S. Bud'ko, N. Ni, S. Nandi, G. Schmiedeshoff, and P. Canfield, Physical Review B **79**, 054525 (2009). 98

[241] A. E. Böhmer, P. Burger, F. Hardy, T. Wolf, P. Schweiss, R. Fromknecht, C. Meingast, H. K. Mak, R. Lortz, S. Kasahara, T. Terashima, T. Shibauchi, and Y. Matsuda, arXiv **cond-mat.supr-con**, 1203.2119 (2012). 98

[242] A. I. Goldman, A. Kreyssig, K. Prokes, D. K. Pratt, D. N. Argyriou, J. W. Lynn, S. Nandi, S. A. J. Kimber, Y. Chen, Y. B. Lee, G. D. Samolyuk, J. B. Leao, S. J. Poulton, S. L. Bud'ko, N. Ni, P. C. Canfield, B. N. Harmon, and R. J. McQueeney, Physical Review B **79**, 024513 (2009). 99, 135

[243] T. Egami, B. V. Fine, D. Parshall, A. Subedi, and D. J. Singh, Advances in Condensed Matter Physics **2010**, 164916 (2010). 99

[244] P. Peterson, M. Gutmann, T. Proffen, and S. J. L. Billinge, Journal of Applied Crystallography **33**, 1192 (2000). 102, 112

[245] C. Farrow, P. Juhas, J. Liu, D. Bryndin, E. S. Bozin, J. Bloch, T. Proffen, and S. J. L. Billinge, Journal of Physics: Condensed Matter **19**, 335219 (2007). 102, 112

[246] M. Han, Q. Yin, W. Pickett, and S. Savrasov, Physical Review Letters **102**, 107003 (2009). 107

[247] N. Qureshi, P. Steffens, S. Wurmehl, S. Aswartham, and M. Braden, arXiv **cond-mat.supr-con**, 1201.2332 (2012). 108

[248] C. A. Young and A. L. Goodwin, Journal of Materials Chemistry **21**, 6464 (2011). 110

[249] D. Dimitrov, H. Röder, and A. Bishop, Physical Review B **64**, 014303 (2001). 115

[250] M. F. Thorpe, V. A. Levashov, M. Lei, and S. J. L. Billinge, From Semiconducutors to Proteins: Beyond the Average Strucure , 105 (2002). 115

[251] K. Deguchi, T. Okuda, Y. Kawasaki, H. Hara, S. Demura, T. Watanabe, H. Okazaki, T. Ozaki, T. Yamaguchi, H. Takeya, F. Saito, M. Hisamoto, and Y. Takano, arXiv **cond-mat.supr-con**, 1204.0190 (2012). 119, 120

[252] A. D. Christianson, M. D. Lumsden, O. Delaire, M. B. Stone, D. L. Abernathy, M. A. McGuire, A. S. Sefat, R. Jin, B. C. Sales, D. Mandrus, E. D. Mun, P. C. Canfield, J. Y. Y. Lin, M. Lucas, M. Kresch, J. B. Keith, B. Fultz, E. A. Goremychkin, and R. J. McQueeney, Physical Review Letters **101**, 157004 (2008). 123, 142

[253] T. Toellner, A. Alatas, and A. Said, J Synchrotron Radiat **18**, 605 (2011). 124

[254] H. Sinn, E. E. Alp, A. Alatas, J. Barraza, G. Bortel, E. Burkel, D. Shu, W. Sturhahn, J. P. Sutter, T. S. Toellner, and J. Zhao, Nuclear Instruments and Methods **467-468**, 1545 (2001). 124

[255] E. Whiting, Journal of Quantitative Spectroscopy and Radiative Transfer **8**, 1379 (1968). 124

[256] J. Olivero and R. Longbothum, Journal of Quantitative Spectroscopy and Radiative Transfer **17**, 233 (1977). 124

[257] T. Goto, R. Kurihara, K. Araki, K. Mitsumoto, M. Akatsu, Y. Nemoto, S. Tatematsu, and M. Sato, Journal of the Physical Society of Japan **80**, 073702 (2011). 126

[258] M. Yoshizawa, D. Kimura, T. Chiba, S. Simayi, Y. Nakanishi, K. Kihou, C.-H. Lee, A. Iyo, H. Eisaki, M. Nakajima, and S.-I. Uchida, Journal of the Physical Society of Japan **81**, 024604 (2012). 126

[259] R. A. Cowley, Physical Review B **13**, 4877 (1976). 126

[260] V. Brouet, M. Marsi, B. Mansart, A. Nicolaou, A. Taleb-Ibrahimi, P. Le Fèvre, F. Bertran, F. Rullier-Albenque, A. Forget, and D. Colson, Physical Review B **80**, 165115 (2009). 126

[261] P. Aynajian, T. Keller, L. Boeri, S. M. Shapiro, K. Habicht, and B. Keimer, Science **319**, 1509 (2008). 127, 128

[262] C.-C. Lee, W.-G. Yin, and W. Ku, Physical Review Letters **103**, 267001 (2009). 127

[263] M. Korshunov and I. Eremin, Physical Review B **78**, 140509(R) (2008). 139

[264] D. Parshall, K. A. Lokshin, J. L. Niedziela, A. D. Christianson, M. D. Lumsden, H. A. Mook, S. E. Nagler, M. A. McGuire, M. B. Stone, D. L. Abernathy, A. S. Sefat, B. C. Sales, D. Mandrus, and T. Egami, Physical Review B **80**, 012502 (2009). 139, 140, 141

[265] M. Yethiraj, G. Aeppli, T. Mason, and T. Armstrong, Physical Review Letters **70** (1993). 139

[266] O. Lipscombe, L. Harriger, P. Freeman, M. Enderle, C. Zhang, M. Wang, T. Egami, J. Hu, T. Xiang, M. Norman, and P. Dai, Physical Review B **82**, 064515 (2010). 139, 140

[267] M. Liu, L. W. Harriger, H. Luo, M. Wang, R. A. Ewings, T. Guidi, H. Park, K. Haule, G. Kotliar, S. M. Hayden, and P. Dai, Nature Physics **8**, 376 (2012). 139, 151

[268] K. Matan, R. Morinaga, K. Iida, and T. J. Sato, Physical Review B **79**, 054526 (2009). 150

[269] M. Kofu, Y. Qiu, W. Bao, S.-H. Lee, S. Chang, T. Wu, and X. Chen, New Journal of Physics **11**, 055001 (2009). 150, 151

[270] C. R. Rotundu and R. J. Birgeneau, Physical Review B **84**, 092501 (2011). 150

[271] S. D. Wilson, Z. Yamani, C. R. Rotundu, B. Freelon, E. Bourret-Courchesne, and R. Birgeneau, Physical Review B **79**, 144502 (2009). 151

Vita

Jennifer Niedziela was born in Massachusetts in 1981, the oldest of three children born to a nurse and insurance salesman turned professional photographer. Being from a nomadic family, she moved around a lot and was never good at being the new kid, a trend that continues to this day.

Jennifer did her Bachelor's in Physics through a combination program between the University of Massachusetts at Amherst (B. S., 2003) and Holyoke Community College (A. S., 2001). As an undergraduate, she spent summers at the Stanford Linear Accelerator Center and Jefferson Laboratory. After graduation, she became a member of the accelerator operations staff at Brookhaven National Laboratory, later serving as an Operations Coordinator. While at Brookhaven, she contributed to accelerator physics experiments to study and correct the accelerator optics; and focused on improving operational reliability. In 2007, Jennifer relocated to Oak Ridge to take a position at Oak Ridge National Laboratory, and was part of the neutron instrument team at the Spallation Neutron Source; at the same time began graduate coursework in August 2007. Jennifer also holds a Masters degree in Business Administration from the University of Phoenix (2008).

Jennifer is a member of the American Physical Society, the American Nuclear Society, the Neutron Scattering Society of America, the American Association for the Advancement of Science, and her local NPR station. Additional non sequiturs include

that she is an ardent supporter of nuclear energy, a big efficiency nerd, and aims to visit every national laboratory in the country before she turns 40. Jennifer currently lives with her nuclear engineer husband in Oak Ridge, Tennessee, where they share a small house with a large book collection and talk a lot about neutrons.